

I. Attenuation Tomography
II. Modeling Regional Love Waves:
Imperial Valley to Pasadena

Thesis by
Phyllis Hang-Yin Ho-Liu

In Partial Fulfillment of the Requirements
for the Degree of
Doctor of Philosophy

California Institute of Technology
Pasadena, California

1988
(submitted May 20, 1988)

Acknowledgements

The research presented in this study was supported by USGS grants #14-08-0001-G1171 and #14-08-0001-G1183, by a grant from the Keck Foundation, and by the Geophysical Sciences Division of the Air Force Geophysics Laboratory under contract F19628-8-K0028.

I am very grateful to the faculty, students and the staff at the Seismo Lab. It was a very enjoyable experience, working with both my thesis advisors, Hiroo who directed me towards the idea of applying back-projection tomography and no-block inversion to the attenuation problem, and Don, who showed me how to make sense out of a bunch of 'wiggles.' Rob Clayton has always been so enlightening in his suggestions (when I can find him), and offered me much support when I first started working in seismology by guiding me into various applications of the finite-difference technique and back-projection tomography.

The transition from a geodynamicist to a seismologist during my first year at the Lab was made easier with the help of many students, especially Luciana, Mark, and my office mates, Bob, John and Harold. Most of the years of my stay at the Lab are pleasant memories, thanks to my Seismo Lab 'buddies': Luciana, Chris, Richard, Bob, John V., Harold, Cathy, Steve G., John L., Gene, Vicky, Ann, Jiajun, Holly, Heidi, Gladys, Cindy, Leslie, Huw the best volleyball umpire, Rob the volleyball dunker, Hua-Wei, Oli, Scott the elastic man, Tom the high bumper, Hitoshi, Linda, Nancy, Dee, Sue, Janet, and many others. My thanks to all the 'aftershocks' (the official Seismo Lab volleyball team) who have been so supportive. I will never forget the cold shower that you gave me in the Men's locker room! Special thanks to Richard, who was willing to set up the volleyball net every time for the team. I am also grateful to Ann who helped me in cleaning up my apartment after my departure and providing me hospitality during my two visits back here to finish up my thesis.

I really enjoyed my experience working with different students and faculty: Chris Sanders was very helpful in showing me how to measure amplitudes on messy seismograms (and get poorer eyesight); experience working with Brad was both exciting and frustrating (in hindsight, I still treasure the experience); Arthur Raefsky was a wonderful person to work with; Jean-Paul was a very patient co-worker in guiding me through the idea of applying inversion to the continuous form of an attenuation problem, and contributed much to the derivation in Chapter 2 of this thesis; Luciana was a delightful co-worker; Christof was generous in letting me use the 3-D raytracer for determining the raypaths in Chapter 1; Marianne Walck also shared her Coso travel-time results with us; John Vidale has given many many brilliant suggestions and useful discussions; and of course Richard Stead has always offered many hours of help in straightening me out during my conversion from a Fortran programmer to a C programmer. And many others. Informal discussions with both faculty and students were tremendously useful in my earlier years at the Lab, and I sincerely hope that an environment of free and friendly discussion will somehow make its way back to the Lab. Carl Johnson and Bob Koyanagi were very helpful in various discussions on the interpretations of Chapter 3, and in providing information about the HVO stations. I also want to thank Holly, John V., Huw, Richard, Dave Scott, and Chris Sanders for reviewing this thesis, and especially Luciana who has probably reviewed each chapter at least twice.

Finally, I would like to especially thank my loving parents (Ping-Kee and Grace) for encouraging and allowing me to study what interested me, my sister Helen for supporting the family all these years so that I could work on my degree, and my very patient and caring husband, Matt, for his tolerance and encouragement and guidance all through my graduate years, and especially his support and advice during my transition from a geodynamicist to a seismologist. I dedicate this thesis to Ping-Kee, Grace, Helen and Matt.

Table of Contents

| | |
|---|-----|
| Acknowledgements | ii |
| Part I: Attenuation Tomography | |
| Abstract | 1 |
| Chapter 1: Applications of Attenuation Tomography to the Imperial Valley and Coso-Indian Wells Region, Southern California | |
| 1.1 Introduction | 3 |
| 1.2 Analogy to Travel-Time Tomography | 4 |
| 1.3 Inverse Problem in Attenuation Tomography | 4 |
| 1.4 Applications to the Imperial Valley and Coso-Indian Wells region | 8 |
| 1.5 Results for the Coso region | 21 |
| 1.6 Results for the Imperial Valley | 30 |
| 1.7 Resolution Estimates and Noise Effects | 33 |
| 1.8 Discussion | 40 |
| 1.9 Conclusion | 46 |
| Chapter 2: Comparison of Iterative Back-Projection and Generalized No-Block Attenuation Tomography | |
| 2.1 Introduction | 50 |
| 2.2 Inverse Problem in Attenuation Tomography | 51 |
| 2.3 Iterative Back-Projection Tomography | 53 |
| 2.4 Generalized Inversion without Blocks | 56 |
| 2.5 Approximate Form of Back-Projection Algorithm | 59 |
| 2.6 Comparison of Results in Case Studies | 62 |
| 2.7 Discussion and Conclusion | 70 |
| Chapter 3: Three-dimensional Attenuation Structure of Kilauea-East Rift Zone, Hawaii | |
| 3.1 Introduction | 72 |
| 3.2 Data Analysis | 76 |
| 3.3 Description of the Model | 86 |
| 3.4 Results..... | 88 |
| 3.5 Resolution of Inversion and Error Estimates | 96 |
| 3.6 Discussion | 110 |
| 3.7 Conclusions | 114 |
| References | 116 |

Appendix 120

**Part II: Modeling Regional Love Waves:
Imperial Valley to Pasadena**

Abstract 124

1. Introduction 125
2. Crustal Cross Section and Green's Functions 133
3. Long-Period Modeling 138
4. Strong Motions from Imperial Valley Events 146
5. Discussion and Conclusion 152

References 159

Abstract to Part I

The inverse problem of seismic wave attenuation is solved by an iterative back-projection method. The seismic wave quality factor, Q , can be estimated approximately by inverting the S-to-P amplitude ratios. Effects of various uncertainties in the method are tested and the attenuation tomography is shown to be useful in solving for the spatial variations in attenuation structure and in estimating the effective seismic quality factor of attenuating anomalies.

Back-projection attenuation tomography is applied to two cases in southern California: Imperial Valley and the Coso-Indian Wells region. In the Coso-Indian Wells region, a highly attenuating body (S-wave quality factor $Q_\beta \approx 30$) coincides with a slow P-wave anomaly mapped by Walck and Clayton (1987). This coincidence suggests the presence of a magmatic or hydrothermal body 3 to 5 km deep in the Indian Wells region. In the Imperial Valley, slow P-wave travel-time anomalies and highly attenuating S-wave anomalies were found in the Brawley seismic zone at a depth of 8 to 12 km. The effective S-wave quality factor is very low ($Q_\beta \approx 20$) and the P-wave velocity is 10% slower than the surrounding areas. These results suggest either magmatic or hydrothermal intrusions, or fractures at depth, possibly related to active shear in the Brawley seismic zone.

No-block inversion is a generalized tomographic method utilizing the continuous form of an inverse problem. The inverse problem of attenuation can be posed in a continuous form, and the no-block inversion technique is applied to the same data set used in the back-projection tomography. A relatively small data set with little redundancy enables us to apply both techniques to a similar degree of resolution. The

results obtained by the two methods are very similar. By applying the two methods to the same data set, formal errors and resolution can be directly computed for the final model, and the objectivity of the final result can be enhanced.

Both methods of attenuation tomography are applied to a data set of local earthquakes in Kilauea, Hawaii, to solve for the attenuation structure under Kilauea and the East Rift Zone. The shallow Kilauea magma chamber, East Rift Zone and the Mauna Loa magma chamber are delineated as attenuating anomalies. Detailed inversion reveals shallow secondary magma reservoirs at Mauna Ulu and Puu Oo, the present sites of volcanic eruptions. The Hilina Fault zone is highly attenuating, dominating the attenuating anomalies at shallow depths. The magma conduit system along the summit and the East Rift Zone of Kilauea shows up as a continuous supply channel extending down to a depth of approximately 6 km. The Southwest Rift Zone, on the other hand, is not delineated by attenuating anomalies, except at a depth of 8-12 km, where an attenuating anomaly is imaged west of Puu Kou. The Mauna Loa chamber is seated at a deeper level (about 6-10 km) than the Kilauea magma chamber. Resolution in the Mauna Loa area is not as good as in the Kilauea area, and there is a trade-off between the depth extent of the magma chamber imaged under Mauna Loa and the error that is due to poor ray coverage. Kilauea magma chamber, on the other hand, is well resolved, according to a resolution test done at the location of the magma chamber.

Chapter 1

Applications of Attenuation Tomography to the Imperial Valley and Coso-Indian Wells Region, Southern California

1.1 Introduction

Back-projection tomography is a technique that utilizes an iterative approach to the solution of an inverse problem. It has been recently applied to travel-time data of seismic waves to invert them for velocity perturbations (Humphreys *et al.*, 1984; Hearn and Clayton, 1986ab; Walck and Clayton, 1987; Clayton and Comer, 1987; Comer and Clayton, 1987). In this study, a similar method is applied to amplitude data, to locate attenuating bodies in the crust. An attenuating body decreases the amplitude of seismic waves passing through it, just as a low-velocity body lengthens the travel time. Previous work on estimating the quality factor of a medium includes the reduced spectral ratio technique (Ward and Young, 1980), which inverts the spectral data directly for the P-wave attenuation, spectral ratio analysis, which calculates the quality factor for S-waves (Kobayashi *et al.*, 1986; Sudo, 1987), and crosshole seismic imaging at two sites, which reconstructs the perturbations of P-velocities between the holes (Wong *et al.*, 1983). This chapter describes the technique of the tomographic inversion of amplitude data and presents two applications. The results from travel-time tomography and attenuation tomography are also compared.

1.2 Analogy to Travel-Time Tomography

Standard travel-time tomography uses the relation between slowness and travel time and is applied to travel-time perturbations (Comer and Clayton, 1987). The seismic travel time is given by the relation

$$\int s \, dl = t , \quad (1)$$

where t is the travel time from source to receiver, dl is the incremental ray length, and s is the slowness along the raypath. However, since the ray path depends on s , this equation is nonlinear with respect to s . A linear system can be obtained by the use of perturbations in t and s (Fawcett and Clayton, 1984). Equation (1) then becomes to first order

$$\int \Delta s \, dl = \Delta t , \quad (2)$$

where Δs and Δt are the perturbations in slowness and travel time, respectively. If the medium is divided into blocks, Equation (2) can be written as

$$\sum_j \Delta s_j l_{ij} = \Delta t_i , \quad (3)$$

where j is the block number, i is the ray number, and l_{ij} is the length of the i^{th} ray in the j^{th} block.

1.3 Inverse Problem in Attenuation Tomography

The tomographic method described in Comer and Clayton (1987) can also be applied to amplitude data to determine the attenuation structure of the medium. We divide the medium into N blocks and let Q_i be the quality factor in the i^{th} block. Then the amplitude of a ray j , A_j , is given by

$$A_j = A_{oj} \prod_{i=1}^N \exp \left(- \frac{\pi f t_{ij}}{Q_i} \right), \quad (4)$$

where A_{oj} is the initial amplitude of ray j , f is the frequency, t_{ij} is the travel time of ray j through the i^{th} block, and N is the total number of blocks in the medium. We set t_{ij} (and l_{ij} below) to be zero for blocks not crossed by the j^{th} -ray.

Rearranging (4) and substituting $l_{ij} s_i$ for t_{ij} , with s_i denoting the slowness of the i^{th} block, we have

$$\frac{A_j}{A_{oj}} = \prod_{i=1}^N \exp \left(- \frac{\pi f l_{ij} s_i}{Q_i} \right) \quad (5)$$

or

$$\ln \left[\frac{A_j}{A_{oj}} \right] = \sum_{i=1}^N \left[\frac{-\pi f s_i l_{ij}}{Q_i} \right] = - \sum_{i=1}^N m_{ij} \left[\frac{f}{Q_i} \right], \quad (6)$$

where m_{ij} is $(\pi s_i l_{ij})$. Denoting $[-\ln (A_j/A_{oj})]$ and f/Q_i by a_j and q_i , respectively, we have from (6)

$$a_j = \sum_{i=1}^N m_{ij} q_i. \quad (7a)$$

Equation (7a) has the same form as Equation (3) with q_i , a_j and m_{ij} replacing Δs_i , Δt_j and l_{ij} , respectively. We can then use the algorithm developed by Comer and Clayton (1987) to solve for the unknown q_i in the medium:

$$q_i^{k+1} = q_i^k + \frac{\sum_j \left(\frac{a_j^k}{L_j} \right) m_{ji}}{\mu + \sum_j m_{ji}} \quad (7b)$$

$$a_j^k = a_j^o - \sum_i m_{ji} q_i^k, \quad (7c)$$

where k denotes the index of iteration, L_j is the total length of ray j , and μ is a damping factor to reduce the effects of less constrained model parameters and to stabilize the solution (Comer and Clayton, 1987).

The effective quality factor in the medium can be calculated from (7). However, the block slowness s_i is not known *a priori*. We can approximate s_i by the slowness of the i^{th} block in the reference velocity model used to trace rays through the medium. Also, a_j is not known because the initial amplitude of the ray is unknown. We obtain a_j by the following analysis. Here we denote the observed S,P wave amplitude by $A_{s,p}$, the initial S,P wave amplitude by A_s^o , the amplitude radiation pattern of S and P waves by $R_{s,p}$, the instrument response for S and P waves by $I_{s,p}$, the geometrical spreading factor for S and P waves by $G_{s,p}$, the frequency by f , the quality factor for P and S waves by $Q_{\alpha,\beta}$, the distance traversed by seismic wave by l , and the slowness parameter by $s_{\alpha,\beta}$. The observed P and S amplitudes are given by

$$A_p = A_p^o R_p I_p G_p \exp \left[-l s_\alpha f \frac{\pi}{Q_\alpha} \right] \quad (8)$$

$$A_s = A_s^o R_s I_s G_s \exp \left[-l s_\beta f \frac{\pi}{Q_\beta} \right]. \quad (9)$$

Dividing (9) by (8), we have

$$\frac{A_s}{A_p} = \frac{A_s^o}{A_p^o} \frac{R_s}{R_p} \frac{I_s}{I_p} \frac{G_s}{G_p} \exp \left[-\pi f l \left(\frac{s_\beta}{Q_\beta} - \frac{s_\alpha}{Q_\alpha} \right) \right]. \quad (10)$$

If we assume that $I_s \approx k_1 I_p$, where k_1 is a constant, $G_s \approx G_p$, and

$A_s^o \approx k_2 A_p^o$, where k_2 is $(\alpha/\beta)^3$, and if we let the quality factor for P-waves, Q_α be represented by ηQ_β (η is a constant), we then obtain

$$\frac{A_s}{A_p} = k_1 k_2 \frac{R_s}{R_p} \exp \left\{ - \pi f l \left[\frac{s_\beta}{Q_\beta} \left(1 - \frac{s_\alpha}{\eta s_\beta} \right) \right] \right\}. \quad (11)$$

For normal crustal rocks, $\eta \approx 2.25$ and the ratio $s_\alpha/\eta s_\beta$ is approximately 1/4 (Anderson and Archambeau, 1964; Anderson, 1967). If the attenuation is caused by the existence of fluid phase, the ratio is even smaller than 1/4. We therefore neglect this term in the inversion. Some observational work indicates that η in the midcrust can be as low as 1 (Rautian *et al.*, 1978; Frankel, 1982). If $\eta \approx 1$, we see from Equation 11 that we need only to multiply the inverted quality factor by a factor of approximately 0.4.

The constant k_1 is determined by the response of the seismograph (in this case, vertical-component instruments with frequency bands of about 5 Hz are used) to the incident P waves and SV waves. It depends on the incidence angle of the wave at the station. Because the velocity of the medium near the surface is very low, the incidence is nearly vertical so that the vertical-component seismograph is not as sensitive to SV-waves as it is to P-waves. We therefore expect k_1 to be a small number, probably in the range of 0.1 to 0.5. We cannot calculate the exact value of k_1 because we do not know the actual P- and S-velocity profiles in the areas. Errors in k_1 propagate throughout the inversion. We include this ratio as an unknown parameter in the inversion and vary it, thereby obtaining the sensitivity of the inversion results to k_1 .

The constant k_2 is determined by the P- and SV-velocities at the source and is approximately 5 for most rocks using a Poisson's ratio of 0.25. Therefore, we expect the product $k_1 k_2$ to be on the order of 1. Since the value of k_1 is uncertain, we perform the inversion for several trial values of $k_1 k_2$, and compare the results. With these assumptions, we obtain

$$\frac{A_s}{A_p} \approx k_1 k_2 \frac{R_s}{R_p} \exp \left(- \pi f l \frac{s_\beta}{Q_\beta} \right)$$

or

$$- \ln \left(\frac{A_s / A_p}{k_1 k_2 R_s / R_p} \right) = \pi s_\beta l \frac{f}{Q_\beta} . \quad (12)$$

Equation (12) can be cast into discrete form as Equation (7) with a_j replaced by $-\ln \left[(A_s / A_p) / (k_1 k_2 R_s / R_p) \right]$, q_i by f / Q_i , and m_{ij} by $l_{ij} \pi s_{\beta i}$. The tomographic technique can be readily applied to solve (12) for the attenuation parameter f / Q_i for the appropriate frequency range of the data.

1.4 Applications to the Imperial Valley and Coso-Indian Wells Region

We have applied this method to data sets obtained for the Coso-Indian Wells Valley and the Imperial Valley, southern California (Figure 1). These two areas have several features in common. Both are sediment-filled basins in active tectonic areas that are local spreading centers or regions of extensional stresses (Hill, 1977; Weaver and Hill, 1978). Earthquake swarms are common

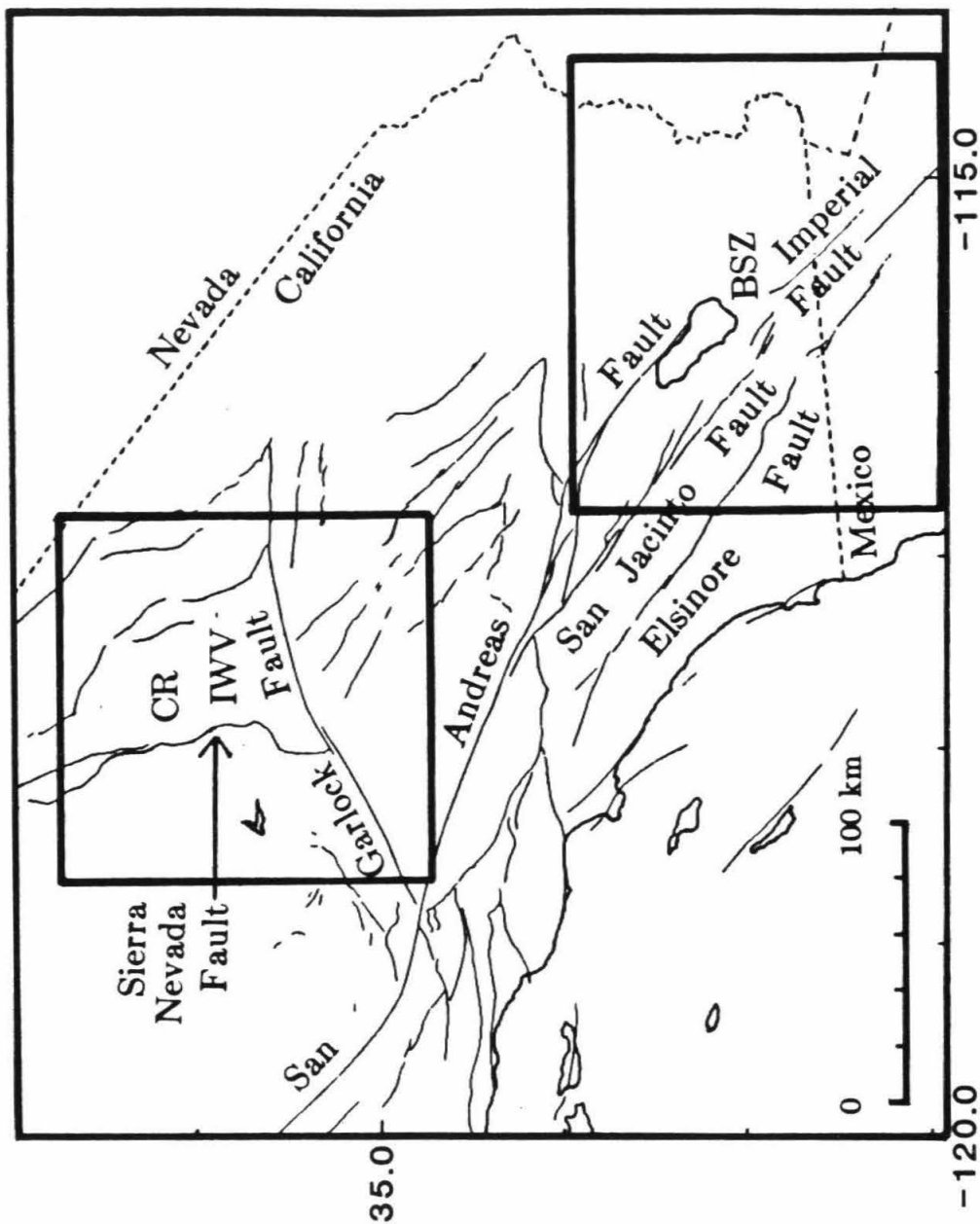


Figure 1: Boxes enclosed the attenuation tomography study areas in Coso-Indian Wells Valley and Imperial Valley, southern California. Major faults are indicated and the abbreviations are: CR-Coso Range, IWW-Indian Wells Valley and BSZ-Brawley Seismic Zone.

in both areas. Magmatic activity has been suspected to cause such swarm activity. However, the three-dimensional structures in these two areas are not known in sufficient detail to determine whether the swarms are due to magmatic, hydrothermal, or other causes. The attenuation tomography described above helps us to detail the three-dimensional Q structure of the underlying medium, thereby adding a constraint on models of the causes of the earthquake swarms.

For the Coso-Indian Wells Valley, we used the 16 earthquakes shown in Figure 2, which were also used by Sanders *et al.* (1988) for S-wave screening studies (Figure 4). Many other earthquakes in the same area could have been used in the study. We limit our choice of events to these 16 earthquakes because they provide an even depth and azimuthal coverage. Also, the amount of computation can be kept to a reasonable level. Depths of these 16 earthquakes are listed in Table 1a. These earthquakes are relocated individually (Sanders *et al.*, 1988). In the attenuation inversion we used the same block size (2 km x 2 km x 0.2 km) as that used in the travel-time inversion of Walck and Clayton (1987). There were 72 blocks in the E-W direction and 72 blocks in the N-S direction, covering an area of 144 km x 144 km. The depth of the model was spanned by 75 blocks, so the model extended down to 15 km. Since the raytracing code that we used requires a non zero velocity gradient in the model, we used a small (0.2 km) block dimension in the depth direction to accommodate the velocity discontinuities in the model shown in Figure 6a. Since we do not expect a spatial resolution of 0.2 km from our data set, we averaged the results over several layers and we present the final results in 1 or

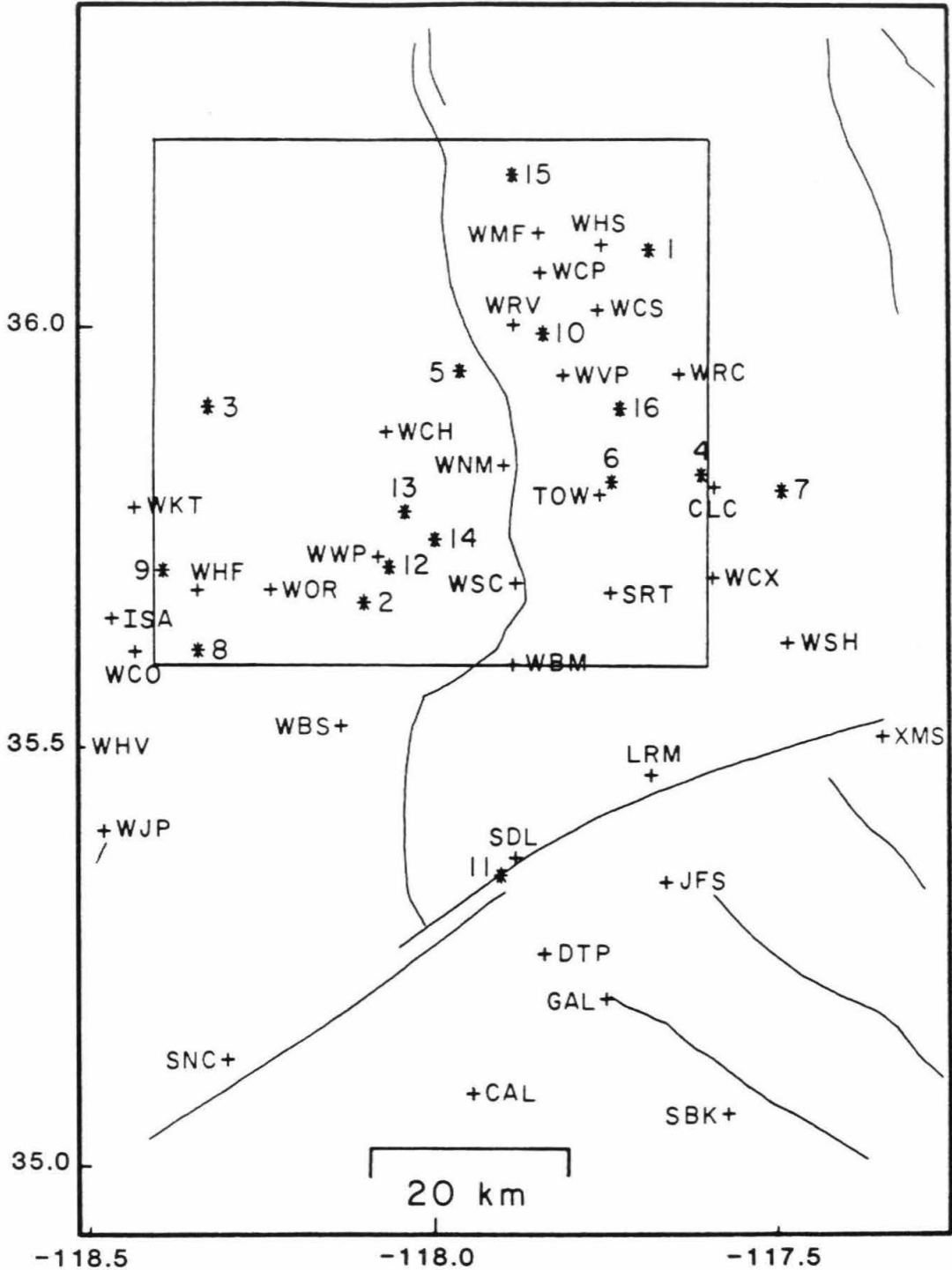


Figure 2: Numbers indicate the locations of the 16 earthquakes used in the attenuation inversion. Station codes show the locations of the Southern California Array stations used in the Coso region study. Inner box is the study area of travel-time inversion by Walck and Clayton (1988).

Table 1a. List of dates and hypocenters of 16 earthquakes used in the Coso-Indian Wells region study

| Event number | Date | Latitude | Longitude | Depth(km) |
|--------------|--------|------------|--------------|-----------|
| 1 | 831030 | 36° 06.89' | -117° 40.35' | 3.2 |
| 2 | 840224 | 35° 41.11' | -118° 06.02' | 10.5 |
| 3 | 840224 | 35° 55.10' | -118° 19.27' | 5.5 |
| 4 | 840109 | 35° 49.87' | -117° 36.29' | 7.5 |
| 5 | 840127 | 35° 57.44' | -117° 57.93' | 9.8 |
| 6 | 840120 | 35° 49.34' | -117° 44.64' | 6.8 |
| 7 | 831006 | 35° 48.72' | -117° 29.72' | 6.5 |
| 8 | 840202 | 35° 37.75' | -118° 20.48' | 13.6 |
| 9 | 830724 | 35° 43.48' | -118° 24.46' | 12.0 |
| 10 | 830731 | 35° 59.04' | -117° 50.91' | 7.4 |
| 11 | 840406 | 35° 21.62' | -117° 54.30' | 10.2 |
| 12 | 830907 | 35° 43.07' | -118° 03.63' | 7.0 |
| 13 | 840411 | 35° 47.31' | -118° 02.21' | 9.4 |
| 14 | 840412 | 35° 45.51' | -117° 59.71' | 7.7 |
| 15 | 808164 | 36° 11.31' | -117° 53.11' | 9.6 |
| 16 | 800822 | 35° 54.18' | -117° 43.56' | 9.5 |

Table 1b. List of dates and hypocenters of 15 earthquakes used in the Imperial Valley study

| Event number | Date | Latitude | Longitude | Depth(km) |
|--------------|--------|------------|--------------|-----------|
| 1 | 831224 | 32° 58.22' | -115° 33.85' | 8.62 |
| 2 | 830902 | 33° 18.44' | -116° 20.55' | 8.95 |
| 3 | 831115 | 33° 02.10' | -115° 33.67' | 8.77 |
| 4 | 831015 | 32° 57.43' | -115° 30.12' | 9.43 |
| 5 | 831212 | 33° 03.74' | -116° 03.22' | 8.28 |
| 6 | 840130 | 33° 02.72' | -116° 12.70' | 2.49 |
| 7 | 840426 | 32° 44.77' | -115° 25.92' | 11.88 |
| 8 | 840422 | 32° 49.14' | -115° 26.73' | 9.87 |
| 9 | 841018 | 32° 49.85' | -115° 36.96' | 10.56 |
| 10 | 841003 | 32° 48.60' | -115° 42.96' | 10.11 |
| 11 | 840417 | 32° 56.96' | -115° 51.99' | 8.13 |
| 12 | 840529 | 32° 52.16' | -115° 31.73' | 8.26 |
| 13 | 840321 | 32° 58.86' | -115° 32.75' | 9.12 |
| 14 | 840429 | 32° 58.04' | -115° 31.62' | 9.26 |
| 15 | 841030 | 32° 56.51' | -115° 32.79' | 10.18 |

2 km thick depth slices.

A data set of 15 earthquakes was chosen from an initial set of more than 200 earthquakes for both the P-wave travel time and S-wave attenuation inversions in the Imperial Valley (Figure 3). The earthquake depths are listed in Table 1b. All earthquakes used in this study are relocated individually, using the layered-velocity model shown in Figure 6b. Similar to the case of the Coso-Indian Wells region, other earthquakes could have been used in the inversion, but we limit our choice to a relatively small number of events with a good coverage of azimuth and depth to keep the amount of computation at a reasonable level. There are events outside the Brawley area that could have been selected. However, most of these events were not recorded on the stations within the area of interest. The station distribution is not as dense in this area as in Coso, forcing us to use more events in the Brawley area to maintain enough resolution in the Brawley seismic zone. The attenuation anomaly is established by events not only in the Brawley area, but also outside the area (for example, event #9 in Figure 5a). The same block size as in the Coso-Indian Wells study was used (2 km x 2 km x 0.2 km). The model was divided into 80 blocks across (E-W) and 72 blocks in the N-S direction, covering an area of 160 km x 144 km. The model had 80 blocks in depth, extending to 16 km. The results were averaged over several layers and were presented in 4 km thick depth slices.

In analyzing the data, amplitudes of P-waves were determined by measuring the maximum peak-to-peak amplitudes on the seismogram nearest the expected P-arrival time (which is the first arrival on the seismogram). The S-

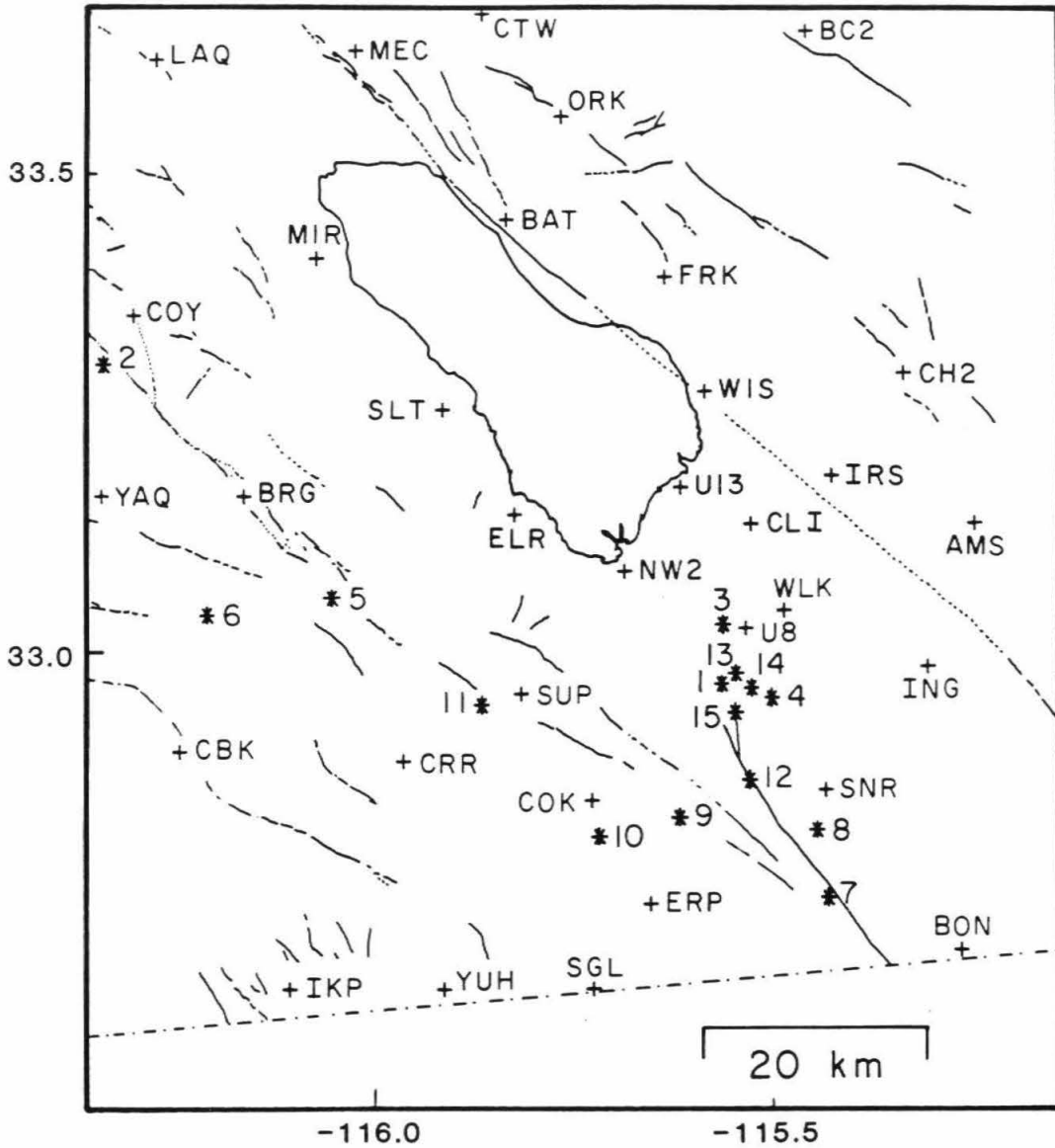


Figure 3: Numbers indicate the locations of the 15 earthquakes used in the attenuation inversion. Station codes show the locations of the Southern California Array stations used in the Imperial Valley study.

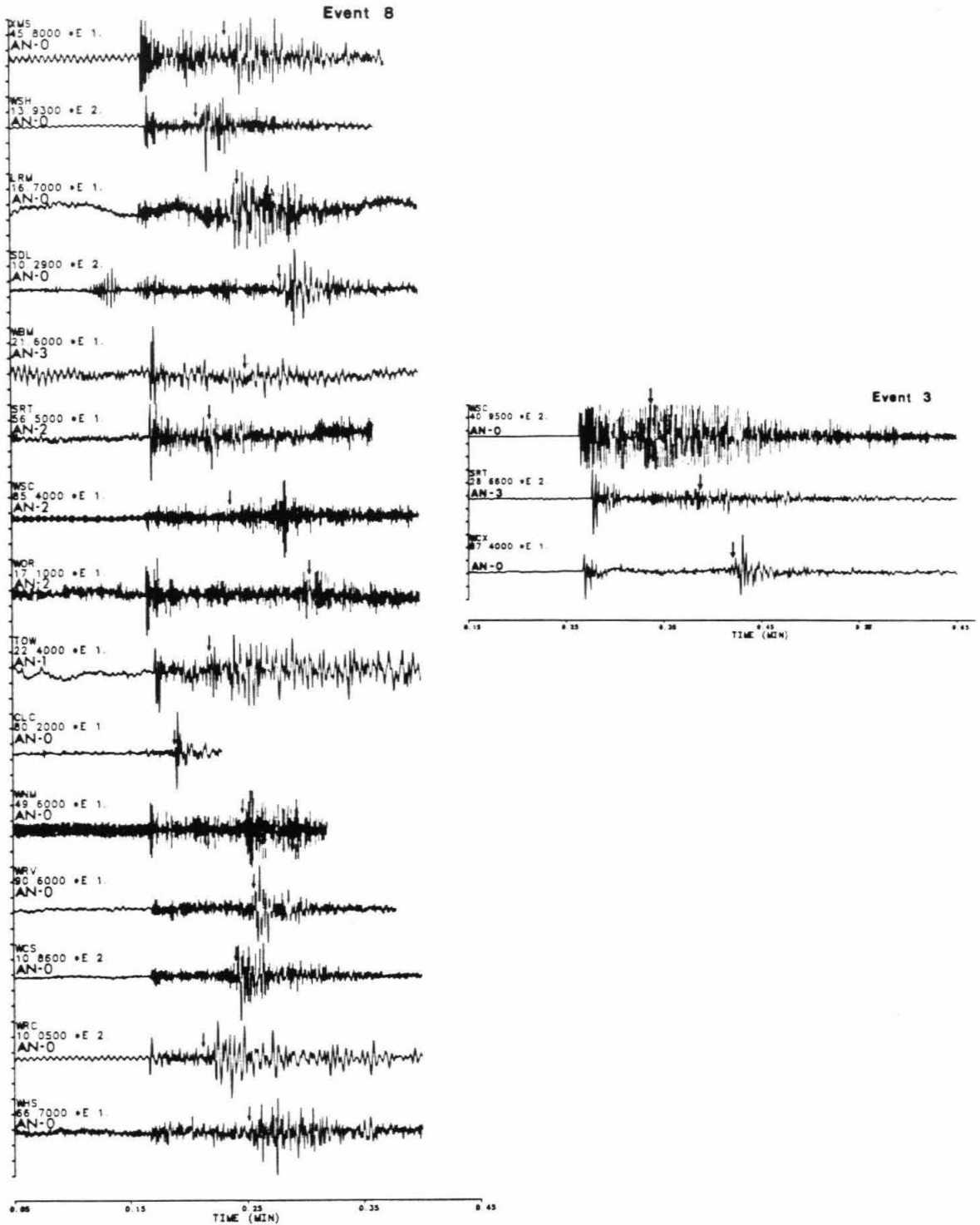


Figure 4a: Examples of seismograms in the Coso-Indian Wells region with attenuated S-arrivals. Arrows indicate the expected S-arrival time (Sanders *et al.*, 1988).

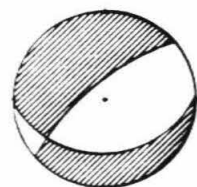
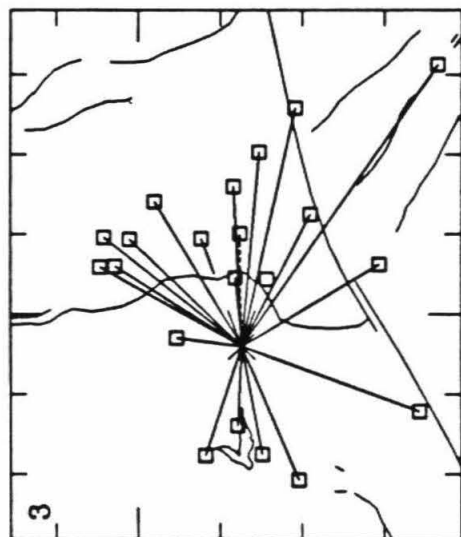
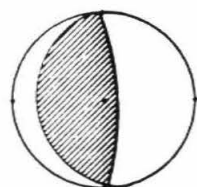
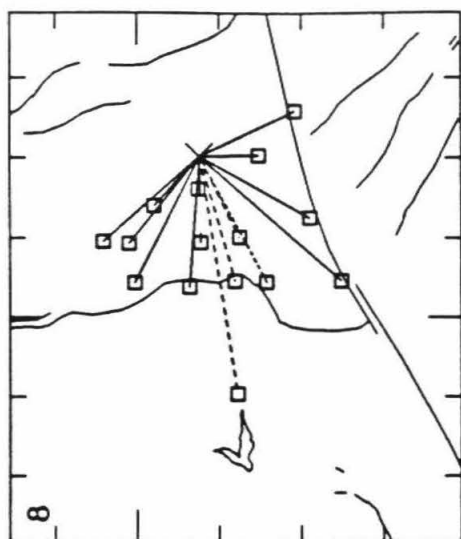


Figure 4b: Plots of ray paths with indication of degree of attenuation for the two events shown on Figure 4a. Short dashes are for highly attenuated rays, long dashes are for partially attenuated rays and solid lines are for normal rays (Sanders *et al.*, 1988). The focal mechanisms are also plotted on the top-left corner of each event.

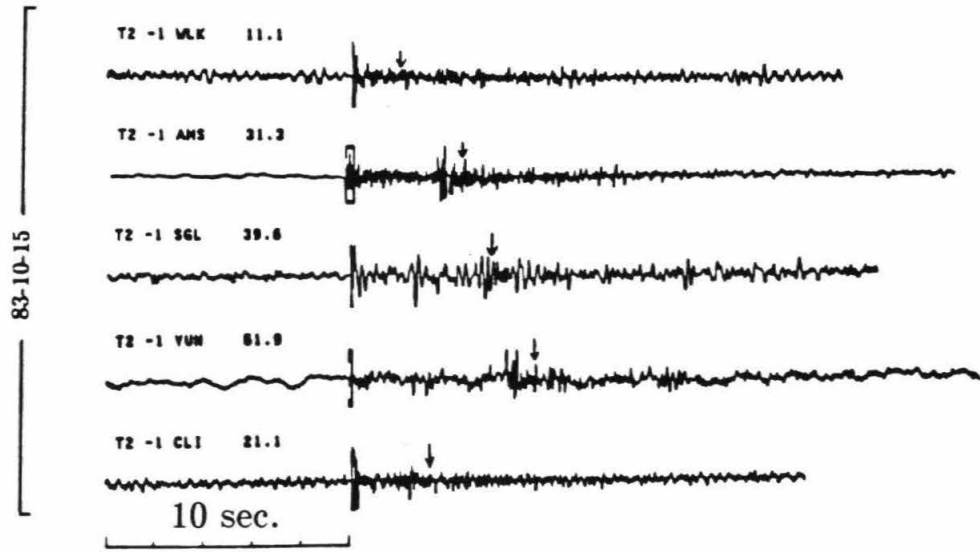
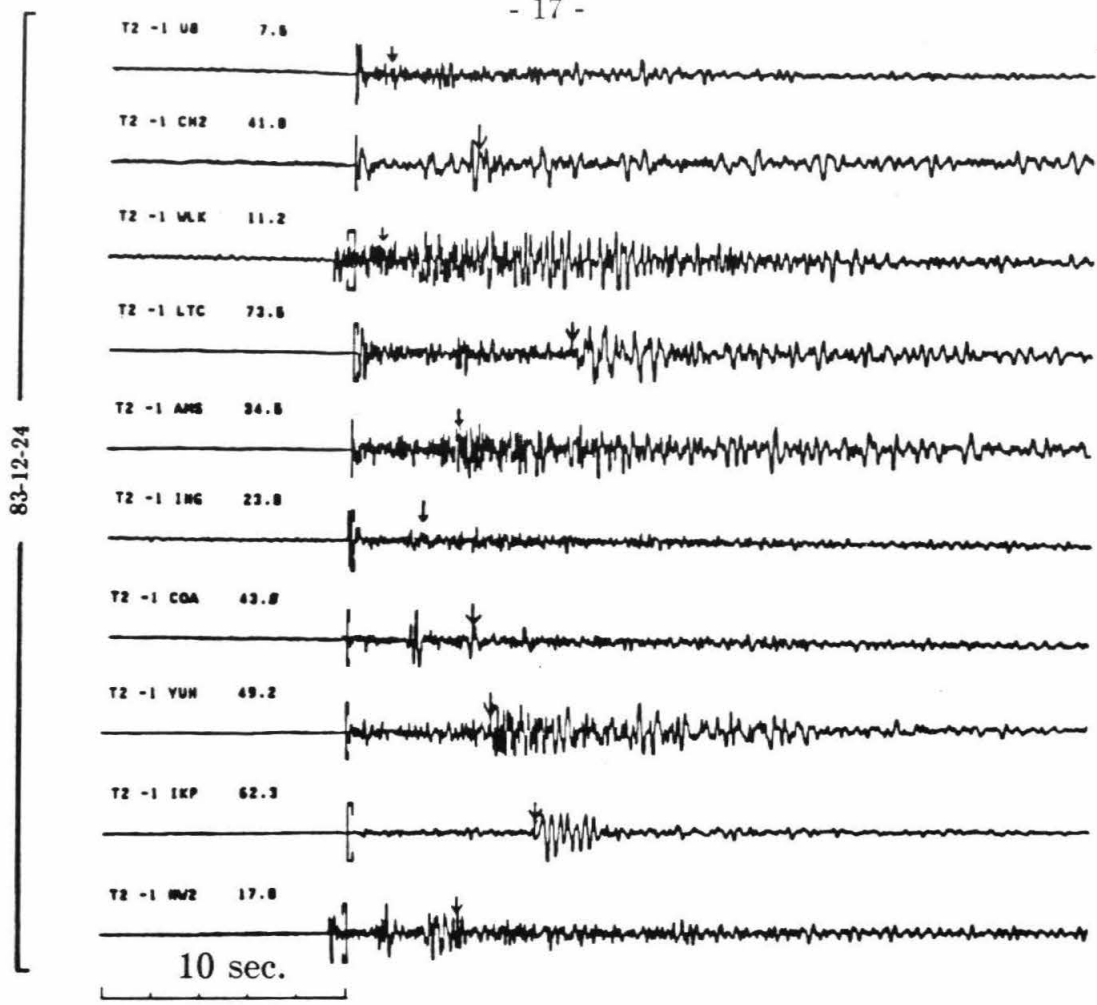


Figure 5a: Examples of seismograms in the Imperial Valley with attenuated S-arrivals. Arrows indicate the expected S-arrival time.

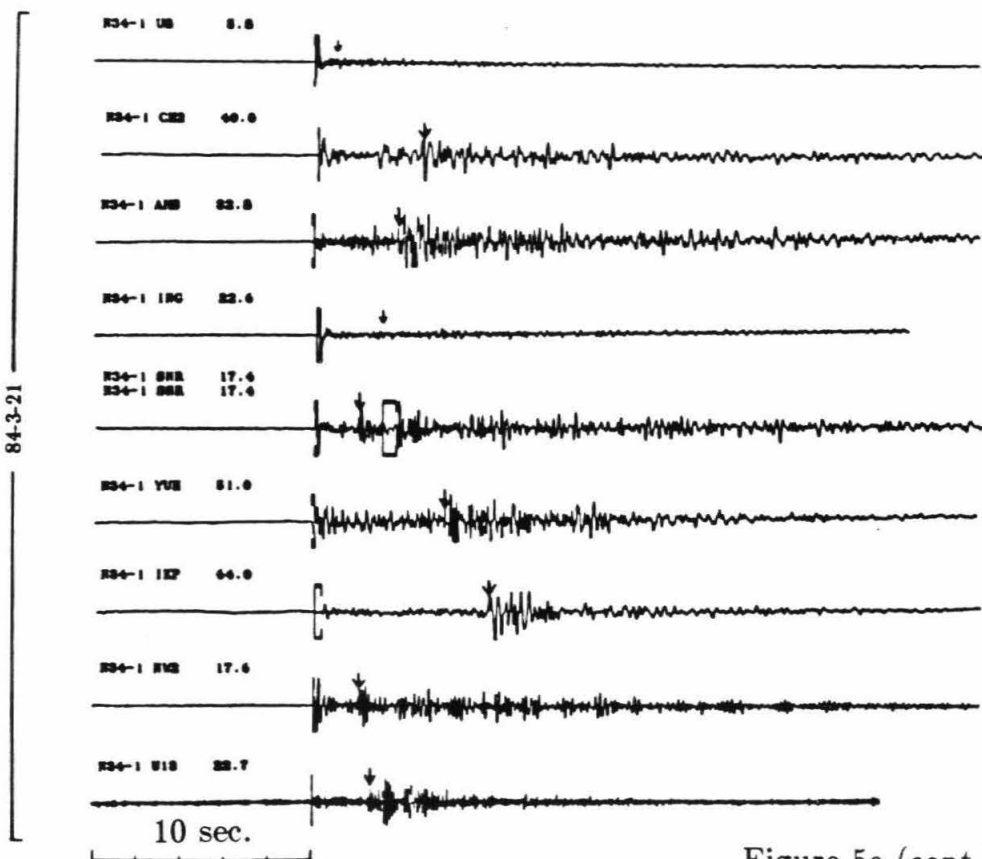
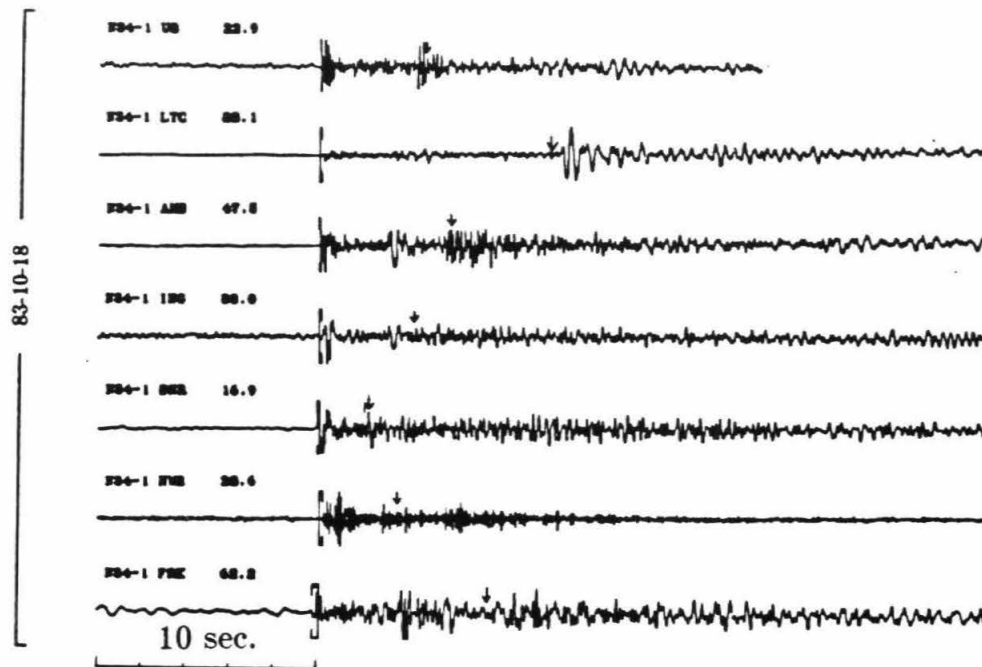


Figure 5a (cont.)

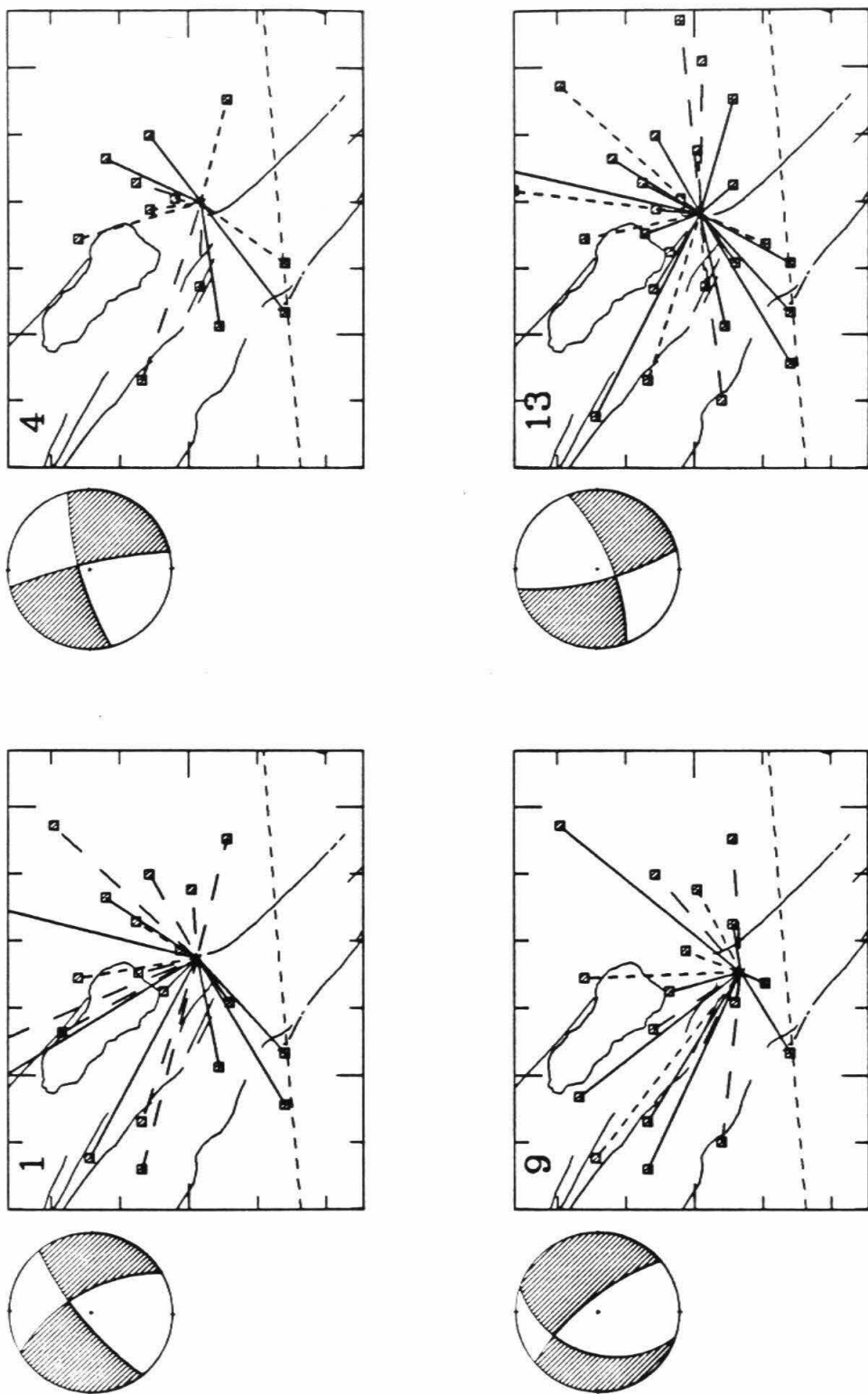


Figure 5b: Plots of ray paths with indication of degree of attenuation for the four events shown in Figure 5a. Degree of attenuation is indicated by the types of lines as indicated as in Figure 4b. The focal mechanisms are also plotted on the top-left corner of each event.

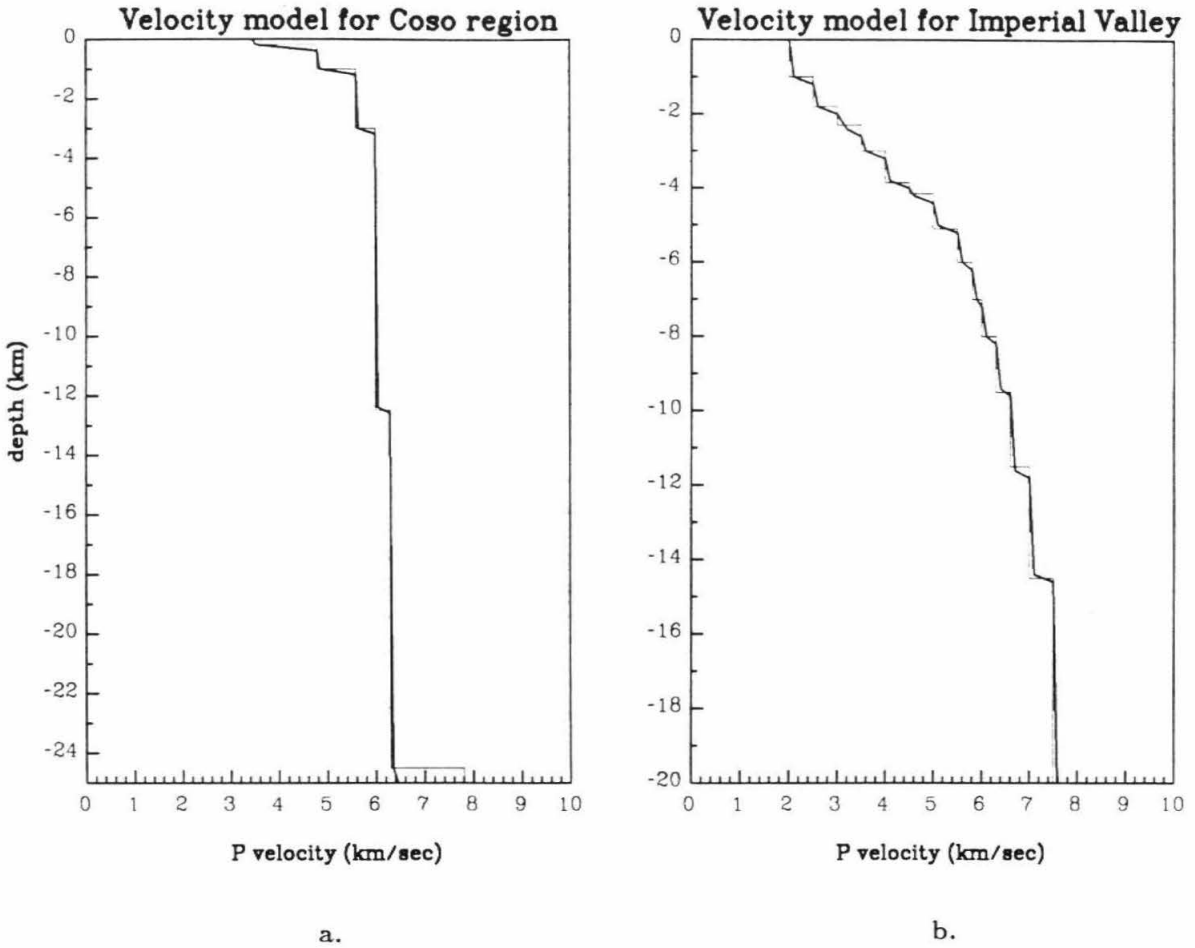


Figure 8: a). Velocity depth function used in the Coso region study. Thin line indicates the velocity model by Walter and Weaver (1980) and bold line is the modified velocity model actually used to trace rays. b). Velocity depth function used in Imperial Valley study. Thin line indicates the velocity model of Fuis *et al.* (1982) and bold line is the modified velocity model used to trace rays.

wave amplitudes were also the maximum peak-to-peak amplitudes within a 0.5 sec time window surrounding the expected arrival time of direct S-waves, or Sg-waves. On some seismograms, the S-wave period is longer than the P-wave period, suggesting greater attenuation of high frequency S-waves, though this could be a source effect. The values R_s/R_p were determined by estimating the focal mechanism for each earthquake from first motion data (Figures 4b and 5b).

1.5 Results for the Coso Region

We first used a homogeneous halfspace to invert the data and compared the results to those obtained by the screening technique described by Sanders (1984). Figure 7 shows the results from the halfspace model inversion for the Coso region at depth ranges of 1-3, 3-5 and 5-7 km. Results are shown in terms of $1/Q$ where filled circles indicate high attenuation (low Q). The larger the size of the circles, the stronger the attenuation. Smallest circles indicate infinite Q . The term k_1k_2 is assumed 1 in the halfspace inversion. The main purpose of the halfspace experiment is to compare the geometry of the anomalous bodies obtained by the halfspace inversion with that inferred from the observations by screening. The exact value of k_1k_2 is not important for this comparison. Locations of anomalous attenuating bodies inferred from screening of S waves (Sanders *et al.*, 1988) are plotted on the same figures for each depth range. The anomalies mapped by the halfspace inversion correspond closely to those obtained by screening.

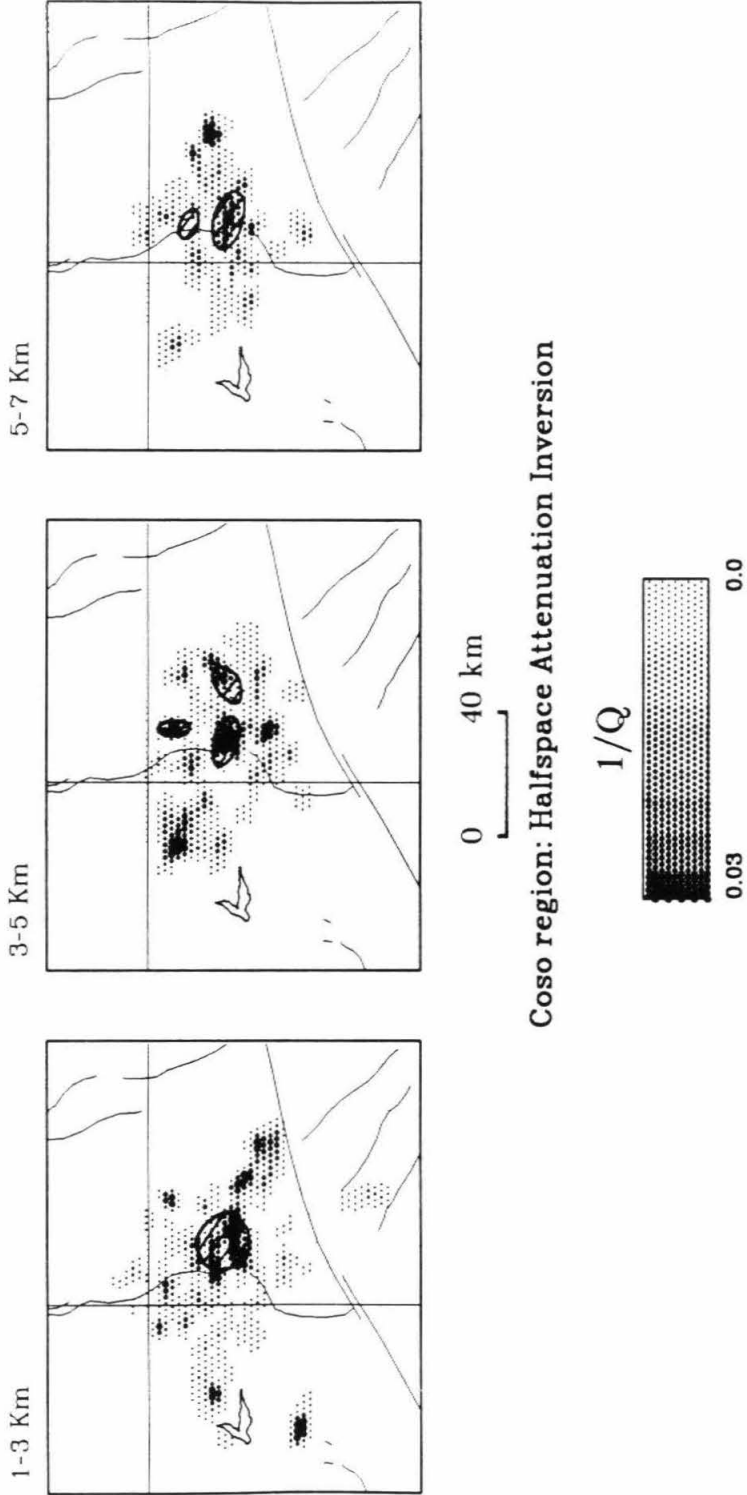


Figure 7: Results of halfspace inversion for Coso region. Depth slices at the depths of 1-3, 3-5 and 5-7 km are shown, together with the anomalies located by the forward modeling of Sanders *et al.* (1988). Large circles indicate areas with high attenuation and small circles indicate areas with low attenuation. Cross-hatched areas are the resolved anomalies from the forward modeling of Sanders *et al.* (1988). Locations of the anomalies in each depth slice obtained by inversion and forward modeling agree well.

We next used the vertically varying structure shown in Figure 6a for the inversion. This structure was obtained by Walter and Weaver (1980) and was used by Walck and Clayton (1987) for velocity inversion. Results with $k_1 k_2 = 1$ are shown in Figure 8a. Depth slices from P-wave travel-time tomography (Walck and Clayton, 1987) are shown in Figure 8b. Since the travel-time inversion was done using a larger data set of more than 400 earthquakes, we did not perform travel-time inversion using the smaller data set used for attenuation tomography. There is a good correlation between low-velocity anomalies and high-attenuation anomalies, despite the fact that a smaller data set was used in the latter. Although the data set used in the amplitude inversion was relatively small, the ray coverage in the central region was dense at depths from 3 to 9 km as indicated by the large number of hitcounts (number of rays that cross a block) shown in Figure 8c. The number of rays used in both cases was on the order of 300. We limited the inversion to blocks with two hitcounts or more. We also inverted the data limited to blocks with four or more hitcounts. Since the blocks with four or more hitcounts were relatively sparse, the results were given only for these sparse blocks. However, when these sparse anomalies were spatially smoothed, the overall pattern was essentially the same as that obtained for blocks with two or more hitcounts. These anomalies include the major anomalies in both Indian Wells Valley and Brawley areas (see next section for the results on Imperial Valley). For layers with sparse ray coverage, for example, layers 1 and 2 in the Coso region and layer 1 in Imperial Valley, any anomalies are considered unresolved. Since this tomographic inversion used the number of hitcounts of a block as the

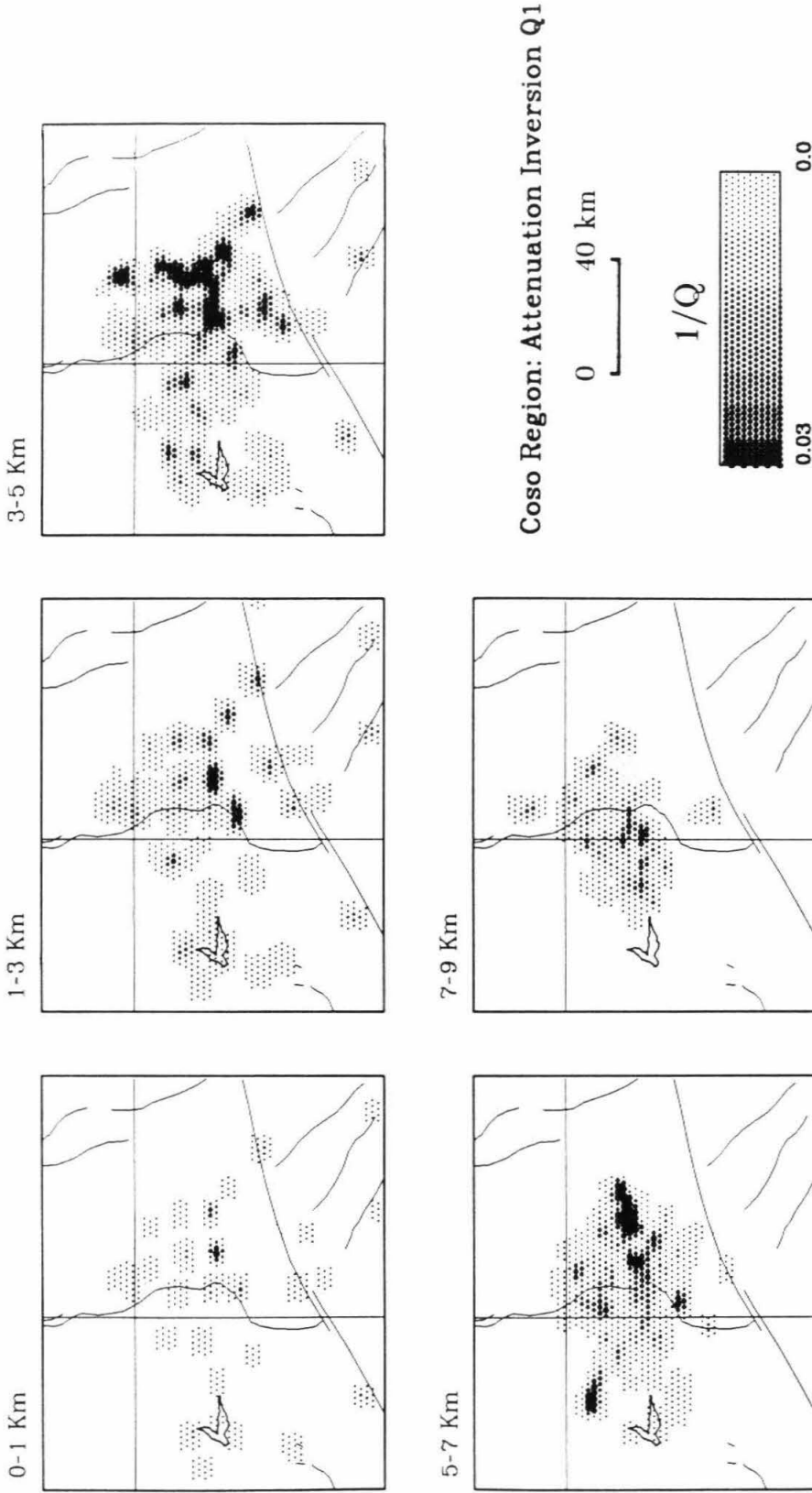


Figure 8a: Results of attenuation inversion using the Coso velocity model shown in Figure 2a. Depth slices at: (i) 1-3 km, (ii) 3-5 km, (iii) 5-7 km and (iv) 7-9 km are shown. A value of 1 was used for $k_1 k_2$. Attenuation anomalies are resolved beneath the Coso Range and the Indian Wells Valley in the depth range of 3-5 km. The locations of these two anomalies agree very well with the low-velocity anomalies obtained by inversion of P-wave travel times (Walck and Clayton, 1988). The anomalies at the edge of ray coverage (see Figure 8c) are probably spurious resulting from low hitcounts or poor azimuthal ray coverage. The Coso range anomaly disappears below 5 km, but the Indian Wells Valley anomaly still exists at 5-7 km depth range.

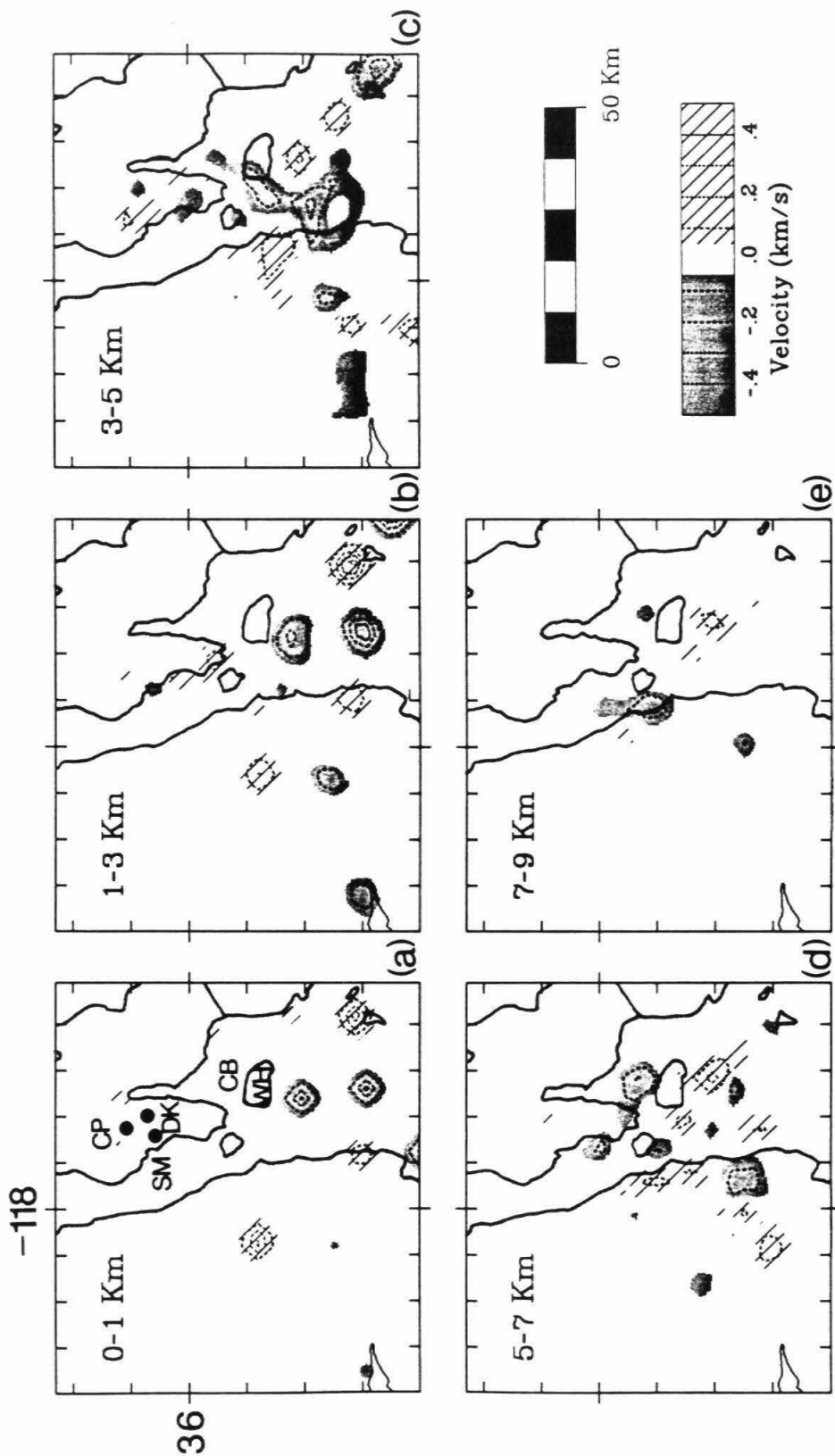


Figure 8b: Results of travel-time tomography (Walck and Clayton, 1988) for the same depth slices as in Figure 8a. The area covered by their study (80 km x 70 km) is smaller than the area covered by this attenuation study (144 km x 144 km). CP stands for Cactus Peak, SM for Sugarloaf Mountain, CB for Coso Basin, DK for Devil's Kitchen, and WH for White Hills. Shaded regions indicate slow anomalies, while hatched areas are fast. Notice the good agreement in locations of these two anomalies (Coso Range and Indian Wells Valley anomalies) in the depth slice of 3-5 km with the anomalies resolved by attenuation inversion shown in Figure 8a-ii.

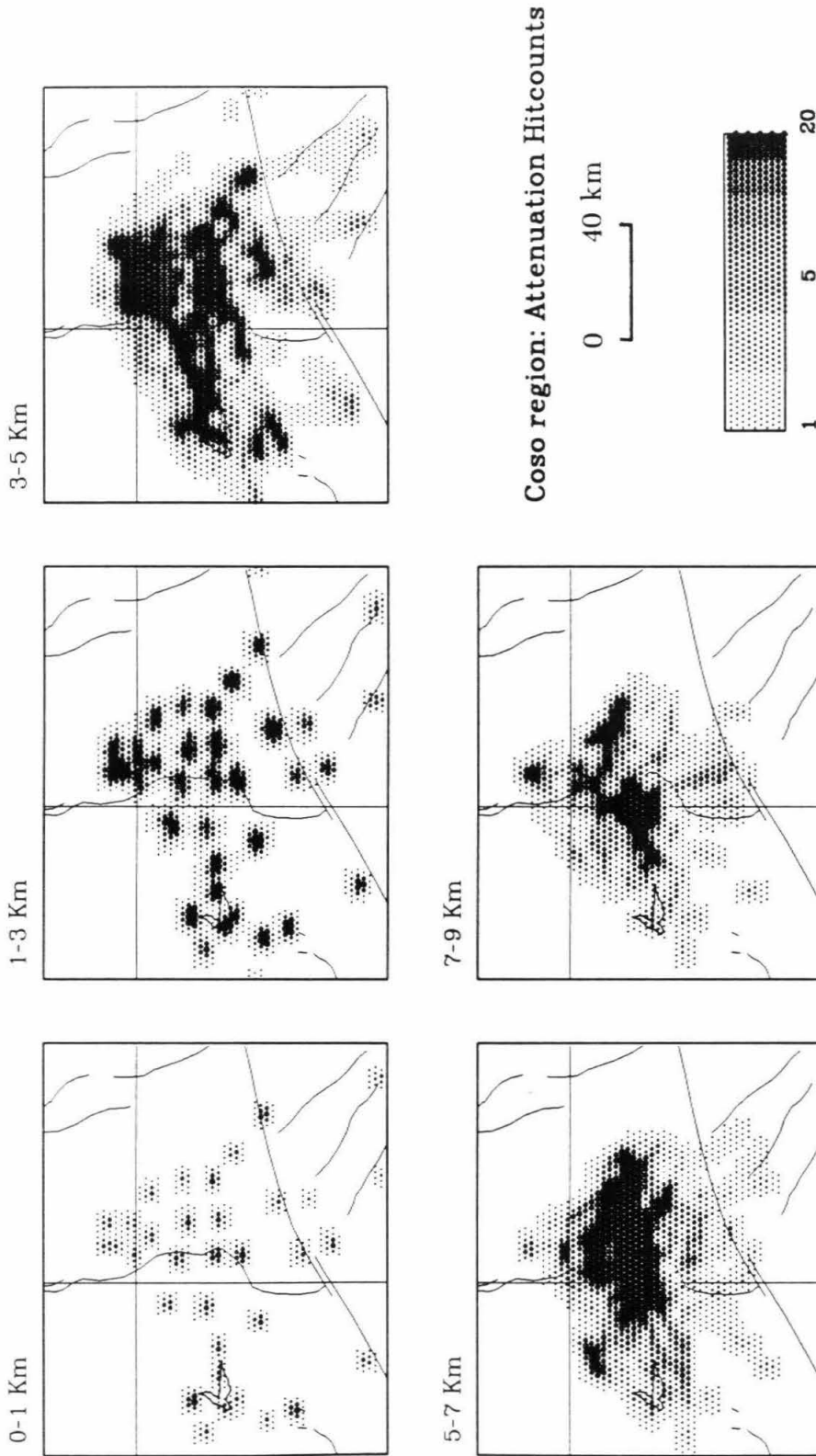


Figure 8c: Hitcount maps of Coso for the depth slices of: (i) 1-3 km, (ii) 3-5 km, (iii) 5-7 km and (iv) 7-9 km. The depth slice of 3-5 km is well covered at the locations of the two resolved anomalies. The hitcount is highest in the center of the model in both 3-5 km and 5-7 km depth slices.

weighting factor for that block, the higher the number of hitcounts, the more reliable the result. There is an apparent correspondence between the locations of resolved anomalies and dense hitcounts (Figures 8a and 8c and Figures 11a and 12), suggesting the possibility that the resolved anomalies are artifacts related to the dense hitcounts that are due to the weighting scheme used in this method. In order to examine this, we used a generalized inversion technique, which uses a different approach to test the resolution (we have a detailed description of this generalized technique in Chapter 2). We found that the locations of the anomalies are well resolved in both cases. Therefore, we conclude that these resolved anomalies are not artifacts of the weighting scheme used in the back-projection method. The quality factor Q_β in the attenuating body is as low as 30, and the average Q_β in the whole region is about 160.

In view of the uncertainty in k_1k_2 , we inverted the same data with $k_1k_2 = 10$ (Figure 8d), and a value of $k_1k_2 = 0.5$ (Figure 8e). Although the spatial extent of the anomalous body in the depth range 3 to 5 km is slightly reduced in both cases, the overall pattern is the same as that shown in Figure 8a (with $k_1k_2=1$). Because of the uncertainty in k_1k_2 , the size and Q_β value of the attenuating body are not definitive, but the overall geometry of the attenuating bodies in the Indian Wells Valley appears to be well resolved.

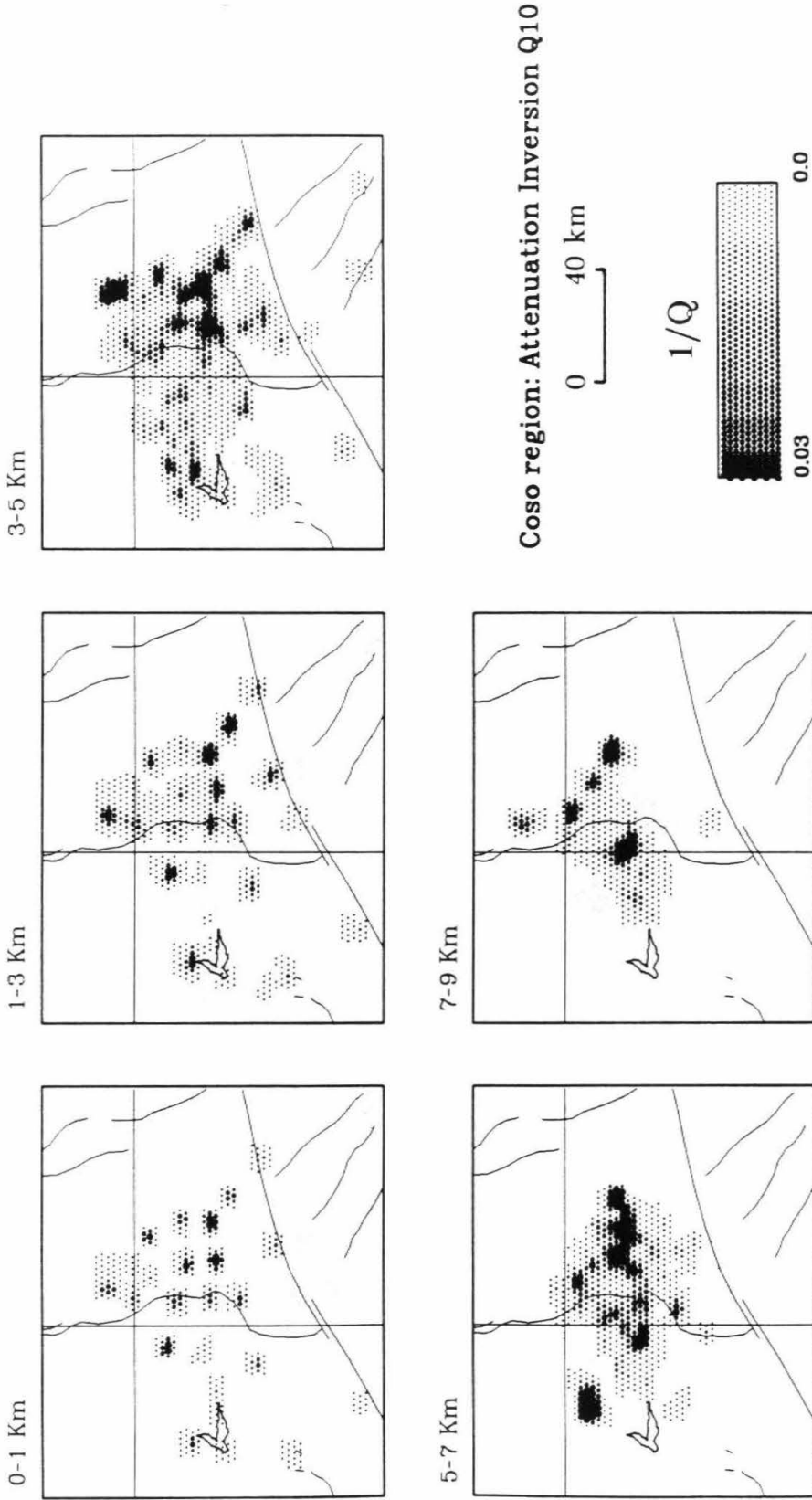


Figure 8d: Results of attenuation inversion with $k_1k_2 = 10$. The two anomalies in the depth range of 3-5 km are still apparent, and the general pattern resembles that shown in Figure 8a. Anomalies at the edge of ray coverage (e.g., the anomaly just northeast of Lake Isabella in the depth range of 5-7 km) are not well resolved. The value of Q_β remains approximately the same as in Figure 8a.

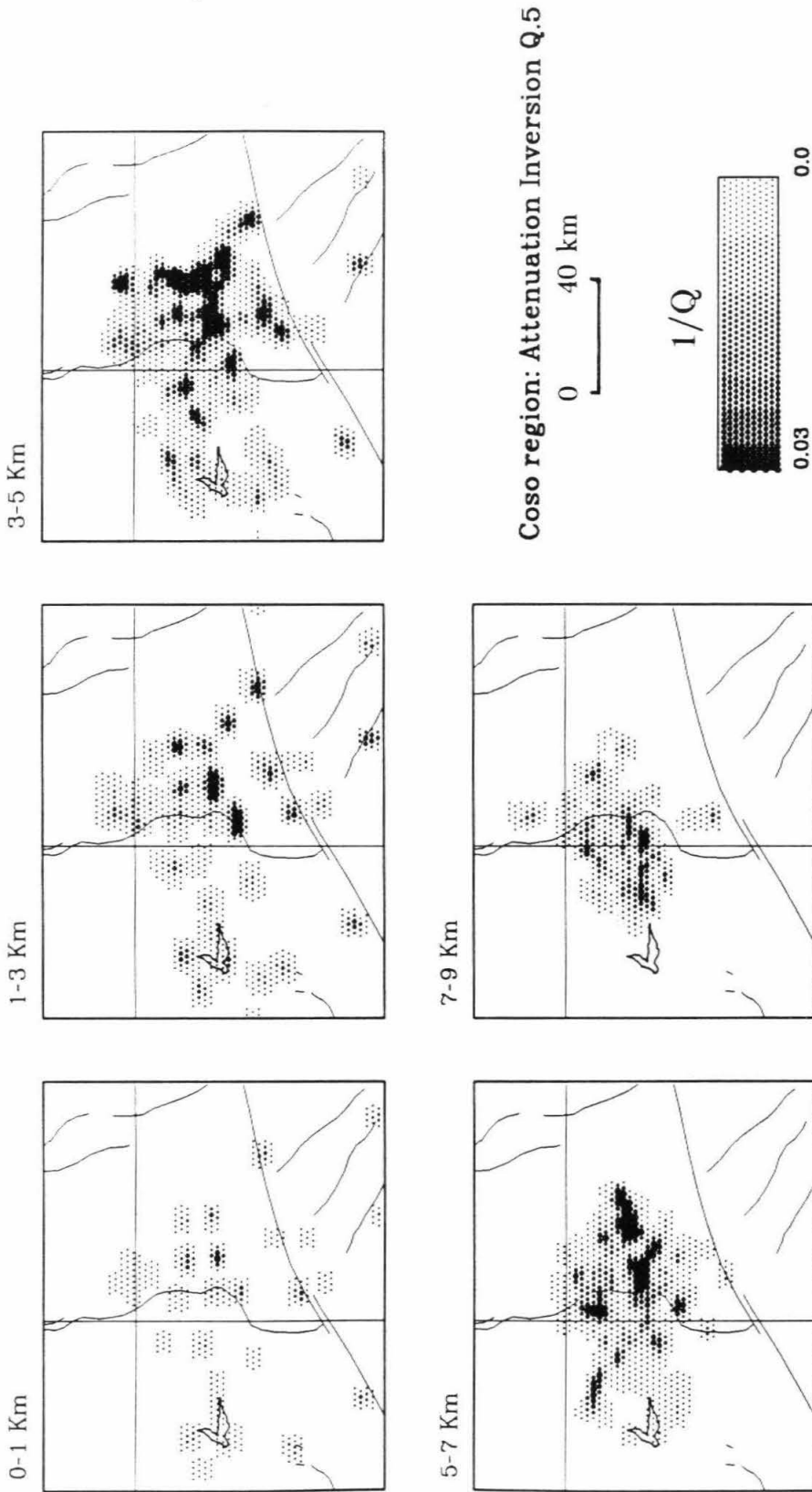


Figure 8e: Results of attenuation inversion with $k_1k_2 = 0.5$. The Indian Wells Valley anomaly are still apparent in the range of 3-5 km. The image of the anomaly remains the same as in Figure 8a. The value of Q_β is slightly lower than the value of the anomaly in Figure 8a, but is on the same order of 30.

1.6 Results for the Imperial Valley

Figure 9 shows the results for the halfspace model for the Imperial Valley together with the anomalies inferred by screening. The value of k_1k_2 is 1 in the halfspace inversion. Attenuation anomalies are found in both the 3-5 km and 5-8 km depth slices in the screening. The largest anomaly is located just north of the Imperial Fault in the southern Brawley seismic zone in the 5-8 km depth slice. By inverting the amplitude data in a halfspace model, we found anomalies in the 3-5 km and 5-8 km depth slices at almost the same locations as from screening.

Next, we relocated all earthquakes used in the analysis (Figure 3) using HYPO78 (Lee and Lahr, 1975) and traced the rays through the velocity model derived by Fuis *et al.* (1982) for the southern Imperial Valley (Figure 6b).

The result of the travel-time tomography is shown in Figure 10. A slow anomaly is found north of the Imperial fault in the Brawley seismic zone. The anomaly is deeper than that found by using the halfspace model because rays are travelling downwards from the earthquakes to the stations in this velocity model. In the halfspace model, the rays travel straight up from the earthquakes, and the image of the anomaly is formed at a shallower depth. The velocity is about 10% slower than normal in the 8-12 km depth range. The number of hitcounts is the highest in the area north of the Imperial fault in the depth range of 8-12 km (see Figure 12 for the hitcount map of attenuation inversion). The hitcount map of travel-time inversion is similar to Figure 12. With a larger number of hitcounts in the Brawley seismic zone, the weighting factor is higher, and therefore the results obtained in the Brawley seismic zone

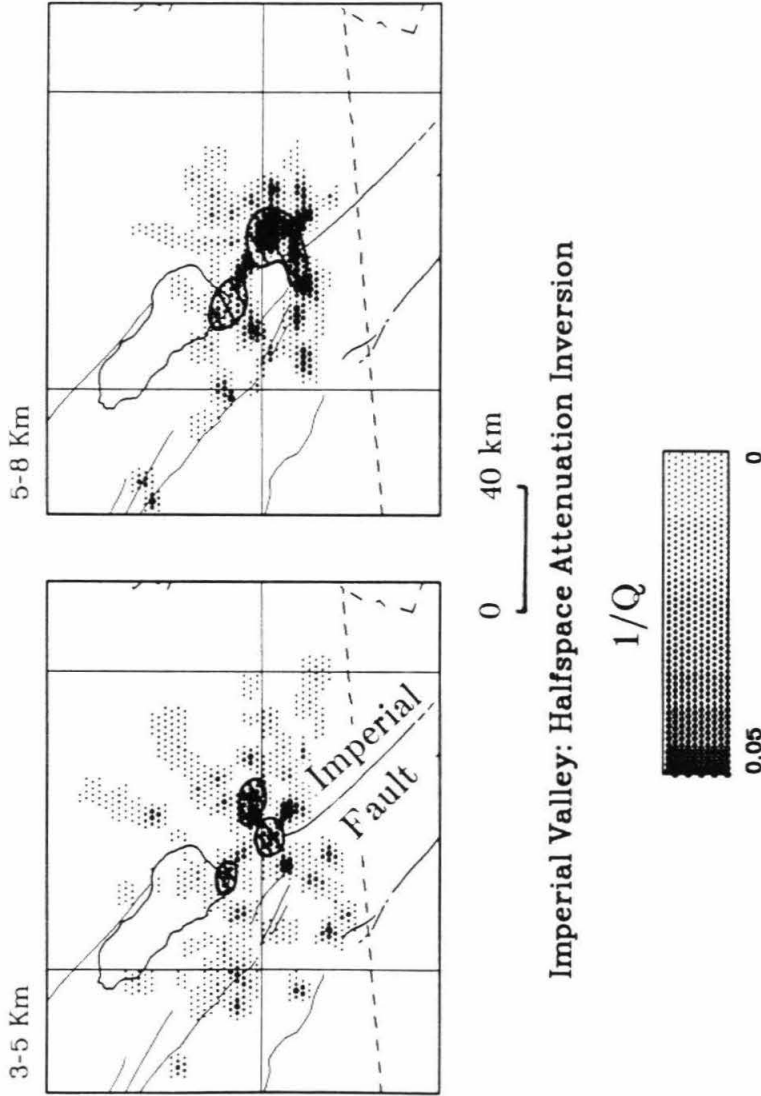


Figure 9: Results of halfspace inversion for Imperial Valley. Depth slices of 3-5 and 5-8 km are shown, together with the anomalies resolved by forward modeling (S-wave screening technique). The major anomaly is that north of the Imperial Fault in the southern portion of the Brawley seismic zone, in the depth range of 5-8 km. The locations of the anomalies obtained by inversion and forward modeling agree well.

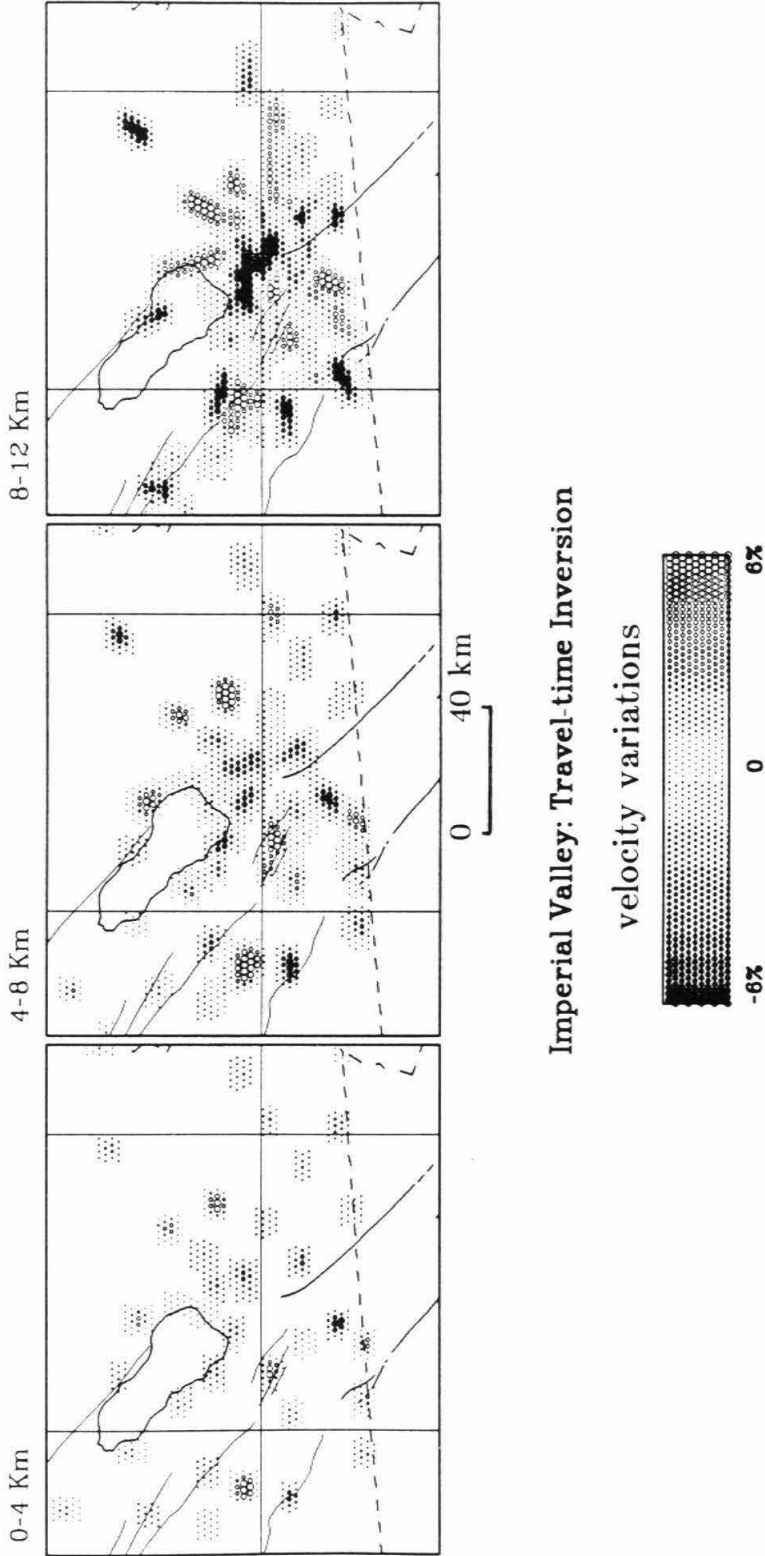


Figure 10: Results of travel-time inversion for the depth slices of: (i) 0-4 km, (ii) 4-8 km and (iii) 8-12 km. The scale indicates percentage variations in P-wave velocities. Filled circles indicate slow velocities, while open circles indicate fast velocities. The 8-12 km depth slice is best resolved. The velocity is 10% slower in the southern Brawley seismic zone in this depth range compared to the surrounding region.

are more reliable than those in other areas of the model.

Figure 11a shows the results of the attenuation tomography, using the same data set with $k_1k_2 = 1$. A highly attenuating anomaly is located north of the Imperial fault in the vicinity of the slow-velocity anomaly at the same depth range of 8-12 km. Figures 11b and 11c show the results of the attenuation tomography with $k_1k_2 = 10$ and $k_1k_2 = 0.5$, respectively. Notice that in both cases where k_1k_2 is not 1, a highly attenuating anomaly is imaged in the southern Brawley seismic zone at 8-12 km depth. The value of Q_β remains on the order of 20 in all three cases. This similarity suggests that the overall geometry of the anomalous structure is resolved well despite the uncertainty in k_1k_2 . This is not surprising because the distribution of the attenuated paths is essentially controlled by the locations of the attenuating bodies. The details of the structure, however, depend on the value of k_1k_2 . Here, we take the result with $k_1k_2 = 1$ as a representative structure. The average Q_β for the area covered by the rays is about 140, which reflects the high attenuation that is due to soft sediments in the valley, a result similar to that obtained in an independent study by Liu (1983) on the 1976 Brawley earthquake.

1.7 Resolution Estimates and Noise Effects

In order to evaluate the resolution of our inversion, we performed a test using synthetic data sets. We first generated a synthetic anomaly either at the location of an anomaly obtained by inversion of the data, or at a location where azimuthal ray coverage is poor but the number of hitcounts is high, as a

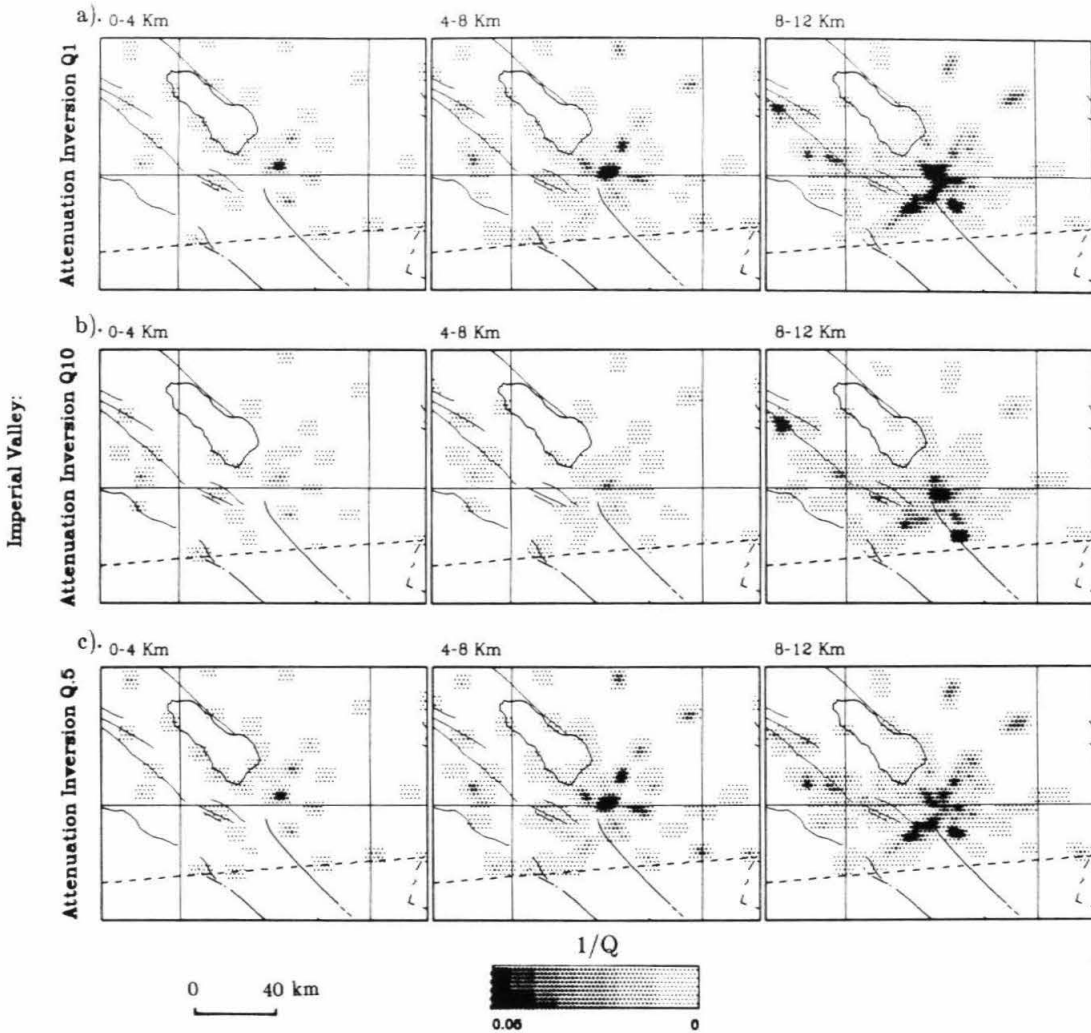


Figure 11: a). Results of attenuation inversion with $k_1k_2 = 1$. The best resolved depth slice of 8-12 km shows a highly attenuating anomaly in the southern Brawley seismic zone, correlated well with the slow anomaly from travel-time inversion (Figure 10). b). Results from attenuation inversion with $k_1k_2 = 10$. The attenuating anomaly is more concentrated in the general Brawley seismic zone. c). Depth slices for results of attenuation inversion with $k_1k_2 = 0.5$. The attenuation anomaly is less intense in the Brawley seismic zone but the general geometry is the same as in (a).

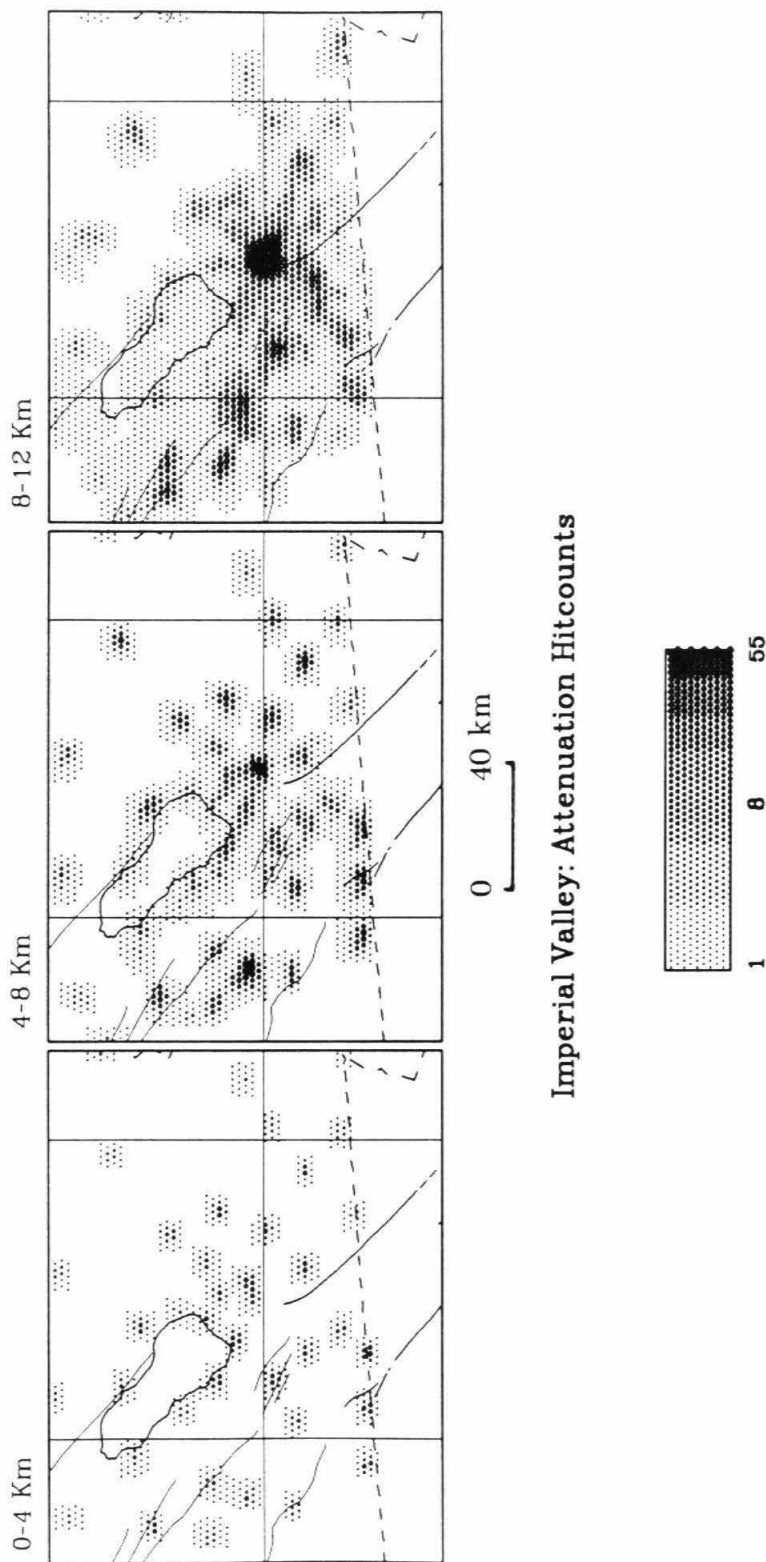


Figure 12: Hitcount maps for attenuation inversion in the same depth slices as in Figure 11. Travel time hitcount distribution was approximately the same. The highest hitcount occurs in the depth range of 8-12 km in the southern Brawley seismic zone. Any anomaly found in this depth range in the Brawley seismic zone is considered well resolved because of the high hitcount.

test of the effect of poor azimuthal ray coverage on the results. We assigned $Q_\beta = 1.0$ to one block at the center of either the anomaly obtained from real data or the area with poor azimuthal ray coverage, setting Q_β to infinity elsewhere. Using this attenuation structure, we computed the amplitude for the rays used in the real data set. We inverted this synthetic data set to test the resolution of our inversion.

For the Coso ray set, a synthetic anomaly with $Q_\beta = 1.0$ is assigned to a block at 7 km depth with a high number of hitcounts but situated at the edge of ray coverage as shown in Figure 13a. This block was of poor azimuthal coverage. As Figure 13b shows, some smearing of the image occurred to the west of the point anomaly. The smearing is more pronounced in the horizontal direction than in the vertical direction. About 90% of the anomaly was recovered by inversion after 30 iterations.

For the Imperial Valley, a synthetic anomaly was generated for both the travel time set ($\Delta s = 1.0$ s/km) and the amplitude set ($Q_\beta = 1.0$) and was given to the block at the center of the anomaly (Figure 14a) resolved by inversion of the actual data. This block was situated at a depth of 8.6 km and it carried the maximum hitcount. Inversion results of travel time (Figure 14b) and amplitude data (Figure 14c) show some smearing of the image in the vertical and horizontal directions. After 30 iterations, about 83% of the travel-time anomaly and about 97% of the attenuation anomaly were recovered.

In order to test the effects of noise on the inversion, the data set was replaced by random noise and was inverted. If the anomaly found by inversion of real data is caused by the presence of high noise level, inversion of

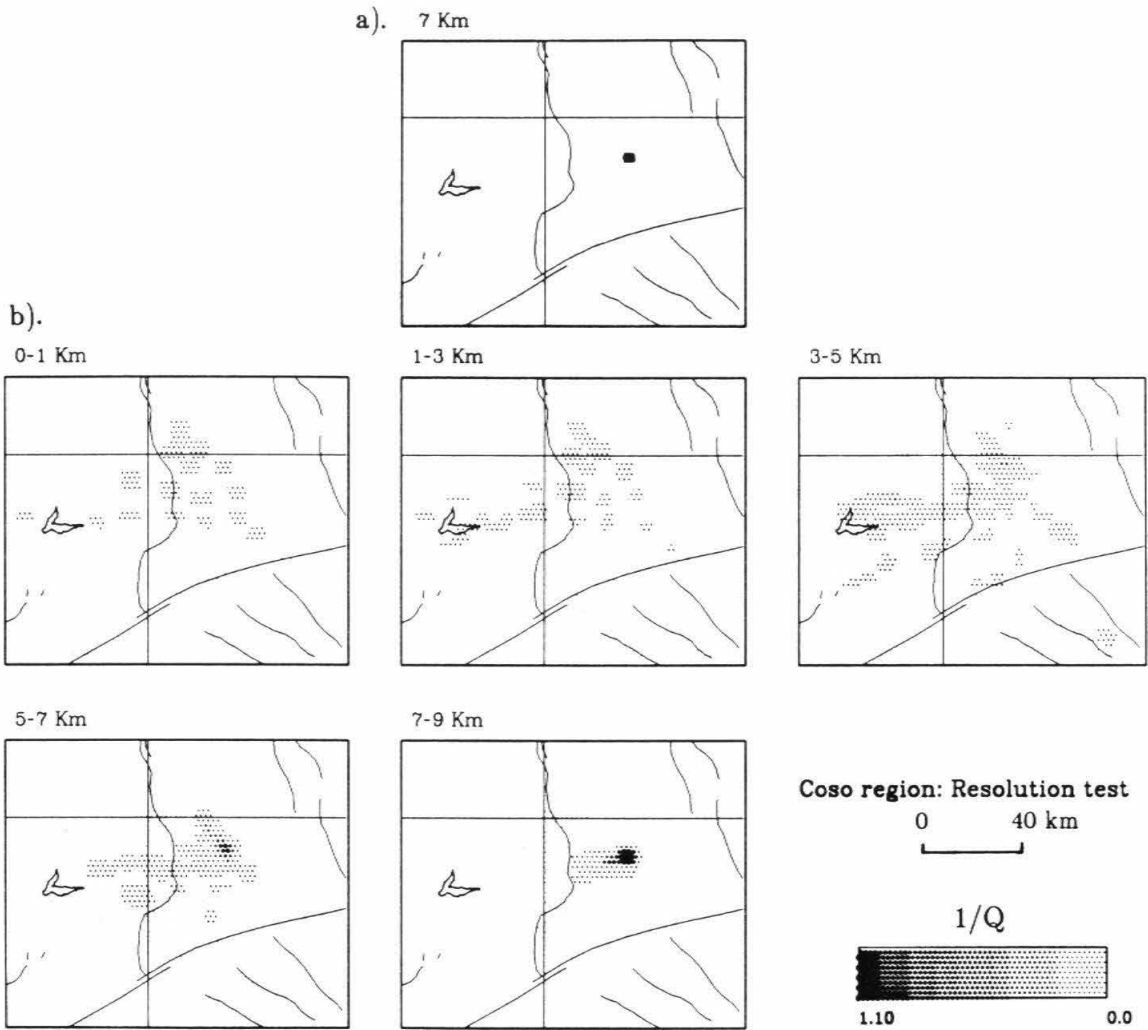


Figure 13: a). Location of a synthetic anomaly in the Coso study. A value of $Q_\beta = 1.0$ was assigned to the shaded block. This block was chosen because of its high hitcount but poor azimuthal ray coverage. The depth of this block is 7 km. b). Results of resolution test for the synthetic anomaly shown in Figure 13a. Northwestward ray streaking can be seen in the depth range 5-7 km.

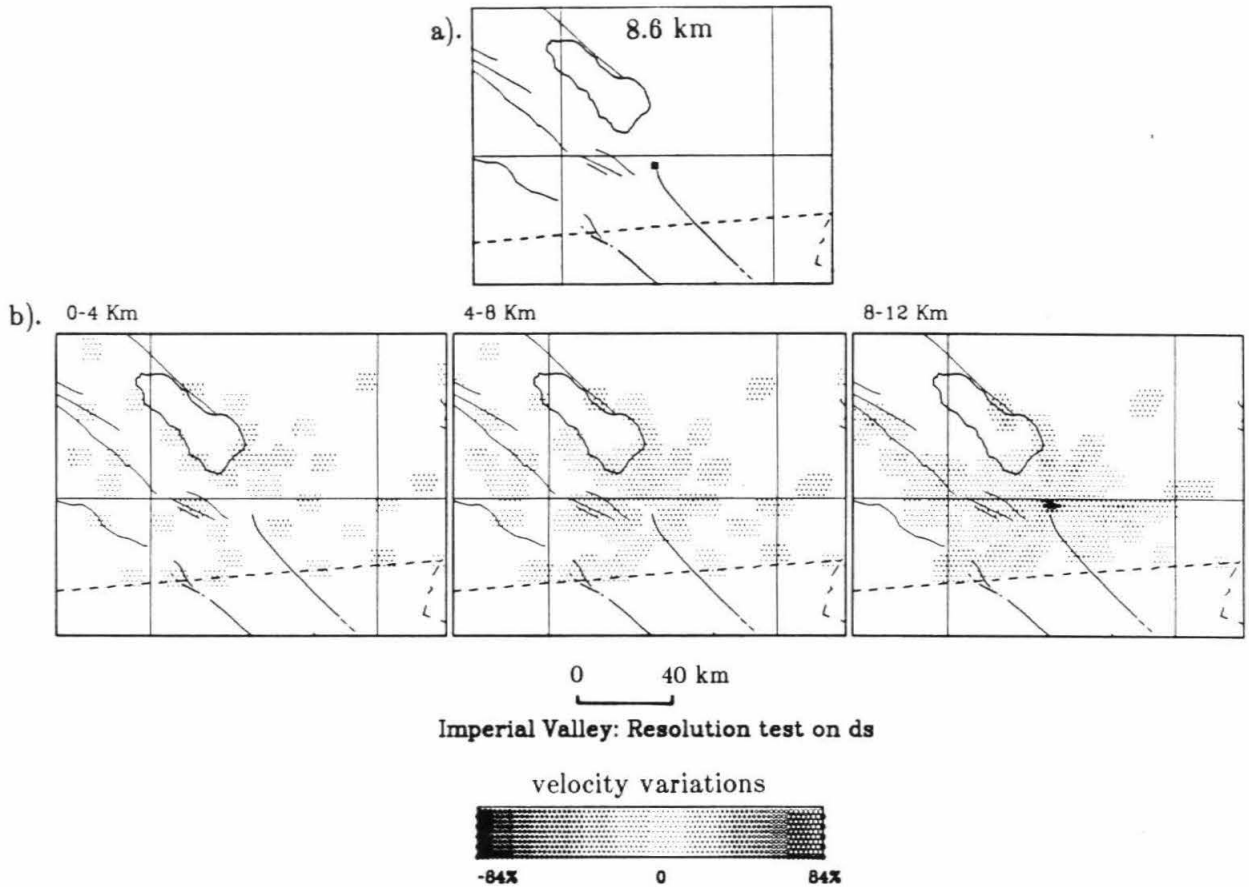


Figure 14: a). Location of a synthetic anomaly in the Imperial Valley study. In the travel-time inversion, a value of $\Delta s = 1.0$ was used, and a value of $Q_\beta = 1.0$ was used in the attenuation inversion. The block was at a depth of 8.6 km. b). Results of resolution test on travel-time inversion for Imperial Valley: Little ray streaking is seen and over 82% of the travel-time anomaly was recovered after 30 iterations. c). Results of resolution test on attenuation inversion for Imperial Valley: The result is very similar to the travel-time test and over 96% of the anomaly was recovered after 30 iterations.

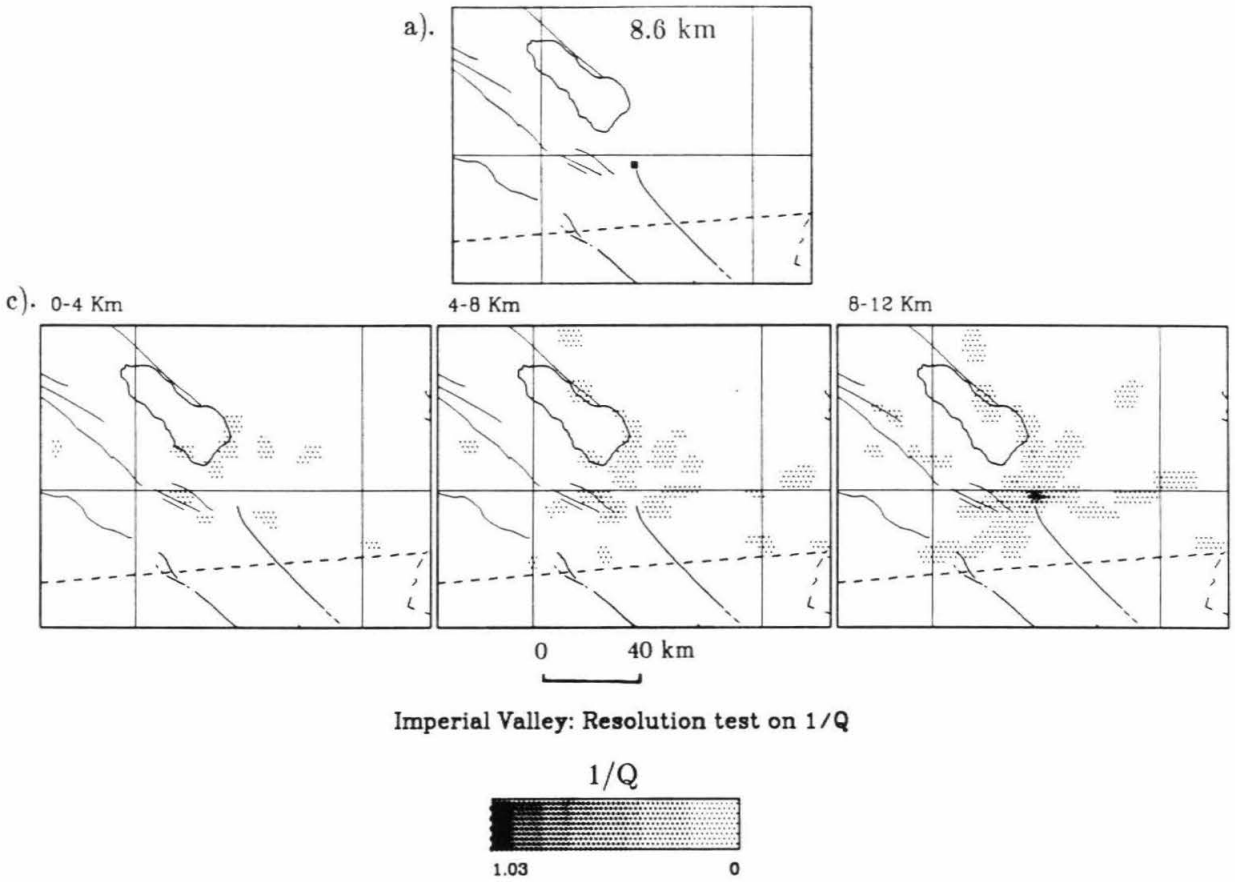


Figure 14a, b & c (cont.)

random noise will image an anomaly at the same location as the anomaly found from inversion of the actual data. As shown in Figure 15, the synthetic data set consisting of random noise yielded a random distribution of anomalies at the depth slice where a single anomaly was found by inversion of real data. Therefore, we believe that random noise was probably not a major cause for the anomalous structure for either Coso or Imperial Valley.

1.8 Discussion

Since most of the stations of southern California network have only a vertical-component seismometer, we had to measure S-wave amplitudes from vertical-component records. The S waves observed on vertical-component seismograms are mostly SV waves, which are more difficult to interpret than SH waves. Furthermore, the incidence angle at the station is usually small, especially on the thick, low-velocity sedimentary layers of the Imperial Valley, so that the vertical component is not very sensitive to S waves. Thus, the experimental setup is not ideal for our purpose. We do not fully understand the nature of these S-waves recorded on the vertical components. One philosophy is not to use them until we can understand them well. Perhaps this has been the prevailing philosophy among seismologists, and, for this very reason, a large amount of data has accumulated unused. We took a somewhat positive philosophy and tried to use these seismograms for mapping attenuating bodies in the crust. This could be a dangerous experiment, unless we carefully examine the data. Our intuitive visual inspection of the data in the manner presented by Sanders *et al.* (1988) indicated that the basic patterns of S-wave

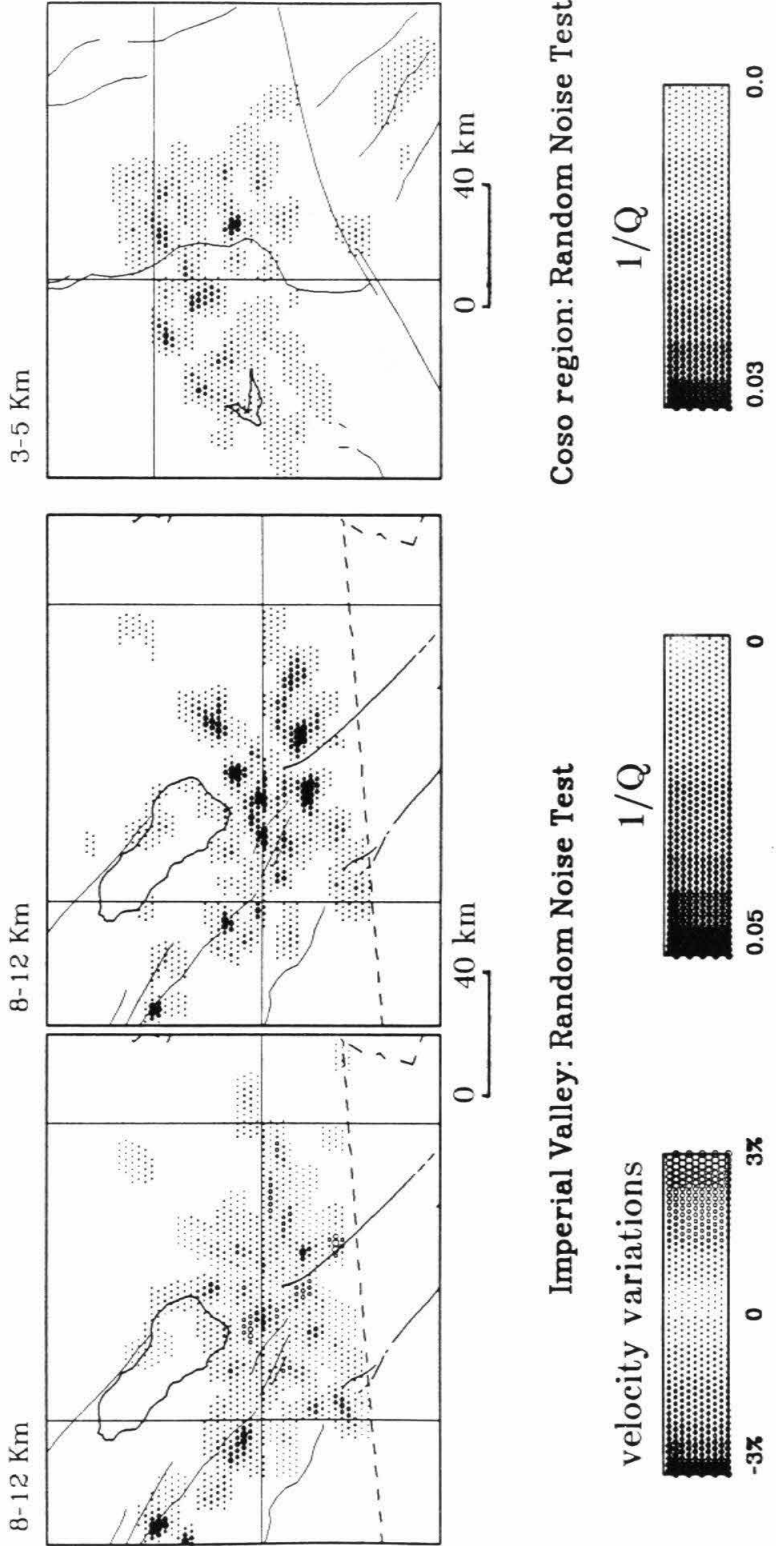


Figure 15a, b and c: Results of tests on inversion with random noise as synthetic data. a). Depth slice 8-12 km of the Imperial Valley travel-time test: near the vicinity of the Brawley seismic zone, no anomaly is resolved by inverting random noise as synthetic travel time data. b). Depth slice 8-12 km of the Imperial Valley attenuation test: by inverting random noise as synthetic amplitude data, no systematic anomaly is resolved in the Brawley seismic zone. c). Depth slice 3-5 km of the Coso test: no systematic anomaly at the location of the Indian-Wells Valley anomaly resolved by inverting data is created by the random noise input.

amplitude variations are large and systematic, suggesting that they are primarily caused by localized low- Q bodies in the crust.

If horizontal instruments are installed in these areas in the future, our method can be used more effectively to determine the crustal Q structures. In the present study, we tested the effect of the sediments on the final result by choosing different values for the parameter k_1k_2 . As we showed earlier, the overall result remained unchanged for a large range of values of k_1k_2 , though the details of the geometry of the anomalous bodies and the Q values changed.

There is one station in the Imperial Valley area that has one horizontal component (SNRE). We examined seismograms of the events recorded at this station. The station SNR is situated on thick sedimentary layers, and any effect of sediments on the measurement of SV-amplitudes should be apparent on the vertical and horizontal records at SNR. Since SNR is located south of the Brawley anomaly, we should have a very good constraint on the southern extent of the Brawley anomaly if S-waves are observed at SNR. We found that the S-to-P amplitude ratios on the vertical components are normal to partially attenuated for the events examined. This suggests that the effect of sediments on the measurement is not as large as we initially estimated, therefore, $k_1k_2 \approx 1$ probably is a good assumption, and the southern extent of the Brawley anomaly is well constrained by the existence of S-arrivals at SNR.

In the formulation of the attenuation tomography given by Equations (4) through (12), we did not include the effect of focusing and defocusing (scattering) of the energy caused by the heterogeneity of the medium. In the actual

medium, however, the wave amplitude can be increased by focusing. As a result of this, negative values of Q often occurred in the inversion. In the results shown in Figures 7, 8, 9 and 11, we have imposed a positivity constraint on the Q values. Whenever negative Q values were obtained, they were replaced by $Q = \infty$. In order to see the effect of this constraint, we inverted the data without the positivity constraint. As shown by Figures 16a (Coso, $k_1 k_2 = 1$) and 16b (Imperial Valley, $k_1 k_2 = 1$), the results are essentially the same as those obtained with the positivity constraint (Figure 8a and Figure 11b).

We computed the variance of the residual of the right-hand side of the Equation 7a at each iteration. Between the initial and the last iterations, we obtained a variance reduction of 53% in the Coso case and 72% in the Imperial Valley, with $k_1 k_2 = 1.0$.

The effect of focusing and defocusing is hard to assess unless we have a fully three-dimensional velocity model for both P- and S-waves. Such a model is also necessary for assessing the validity of our assumption that the P- and S-wave geometrical spreading factors are the same. We can obtain a P-wave velocity model by inverting the P-wave travel-time residuals, but with frequently missing S-waves, it is unlikely that we can invert the S-wave data in the same fashion to obtain S-wave velocity models.

There are some questions about the Brawley anomaly's being in the same location as some of the events used in the study. We have shown previously that the effects of noise in the data do not cause spurious anomalies in the Brawley area. In order to show that the anomaly is not due to clustering of

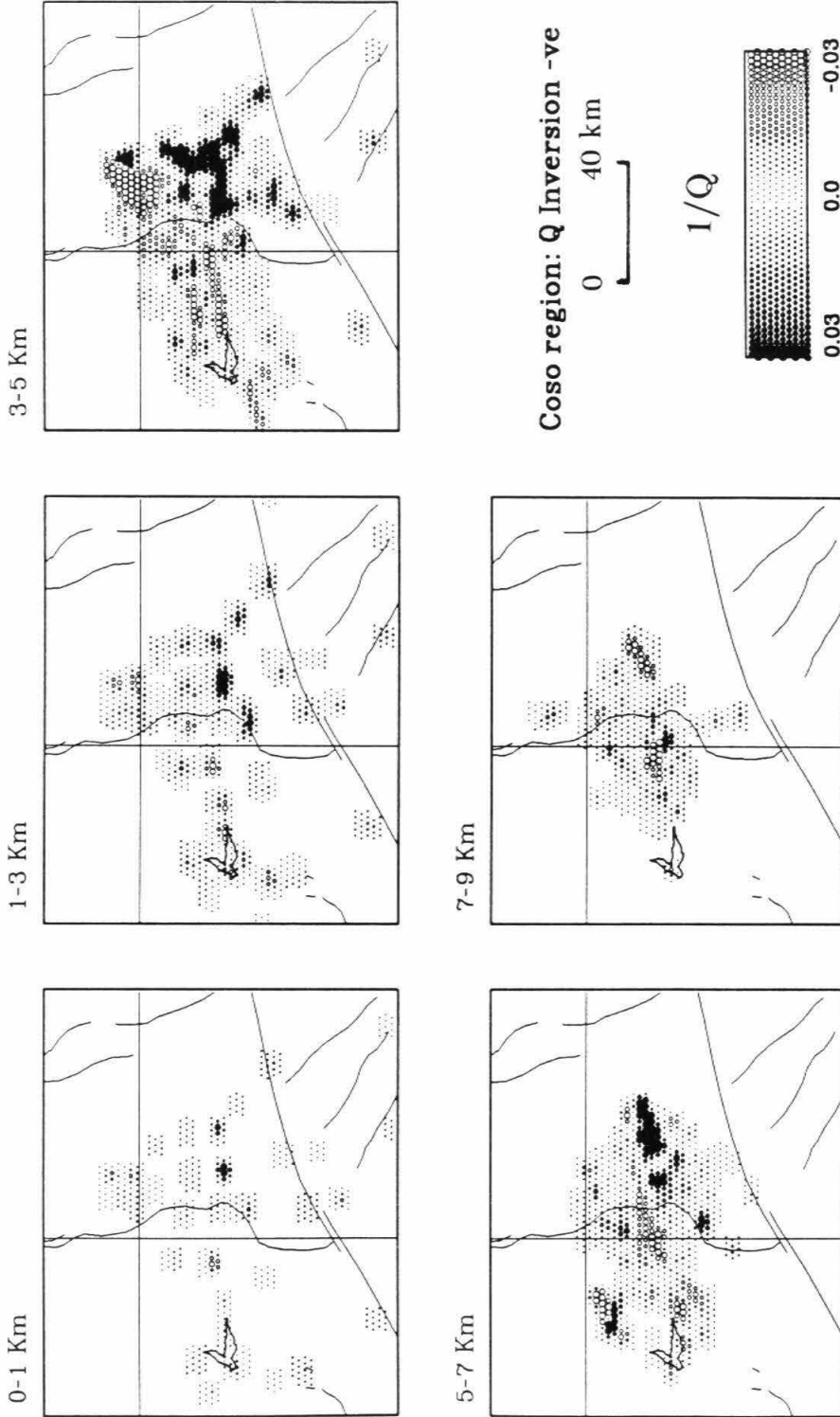


Figure 16a: Results of attenuation inversion using $k_1 k_2 = 1.0$ for the Coso-Indian Wells region. There is no positivity constraint for Q_j in this inversion. Notice that the geometry of anomalies resolved is the same as in the corresponding results in Figure 8a.

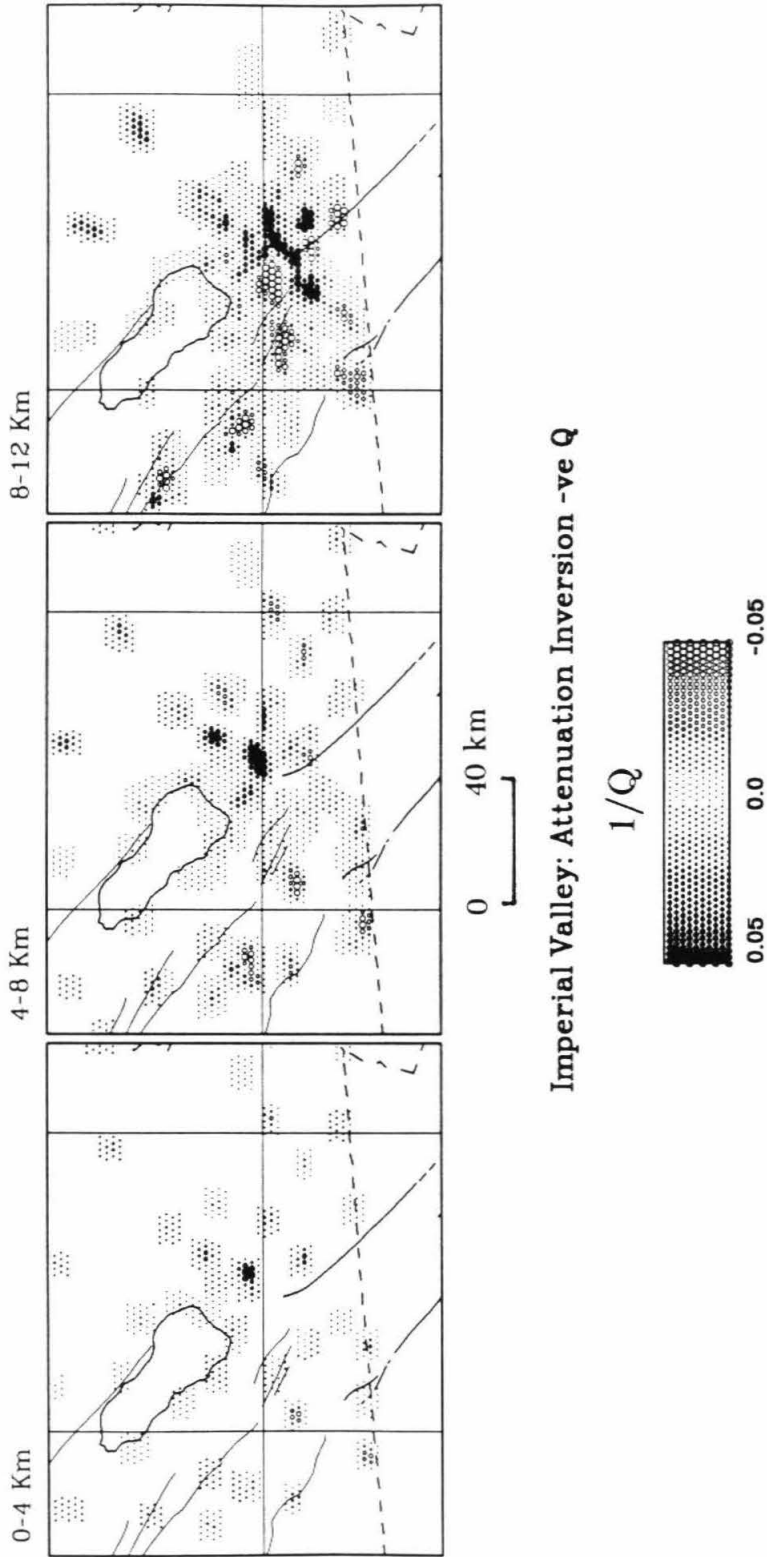
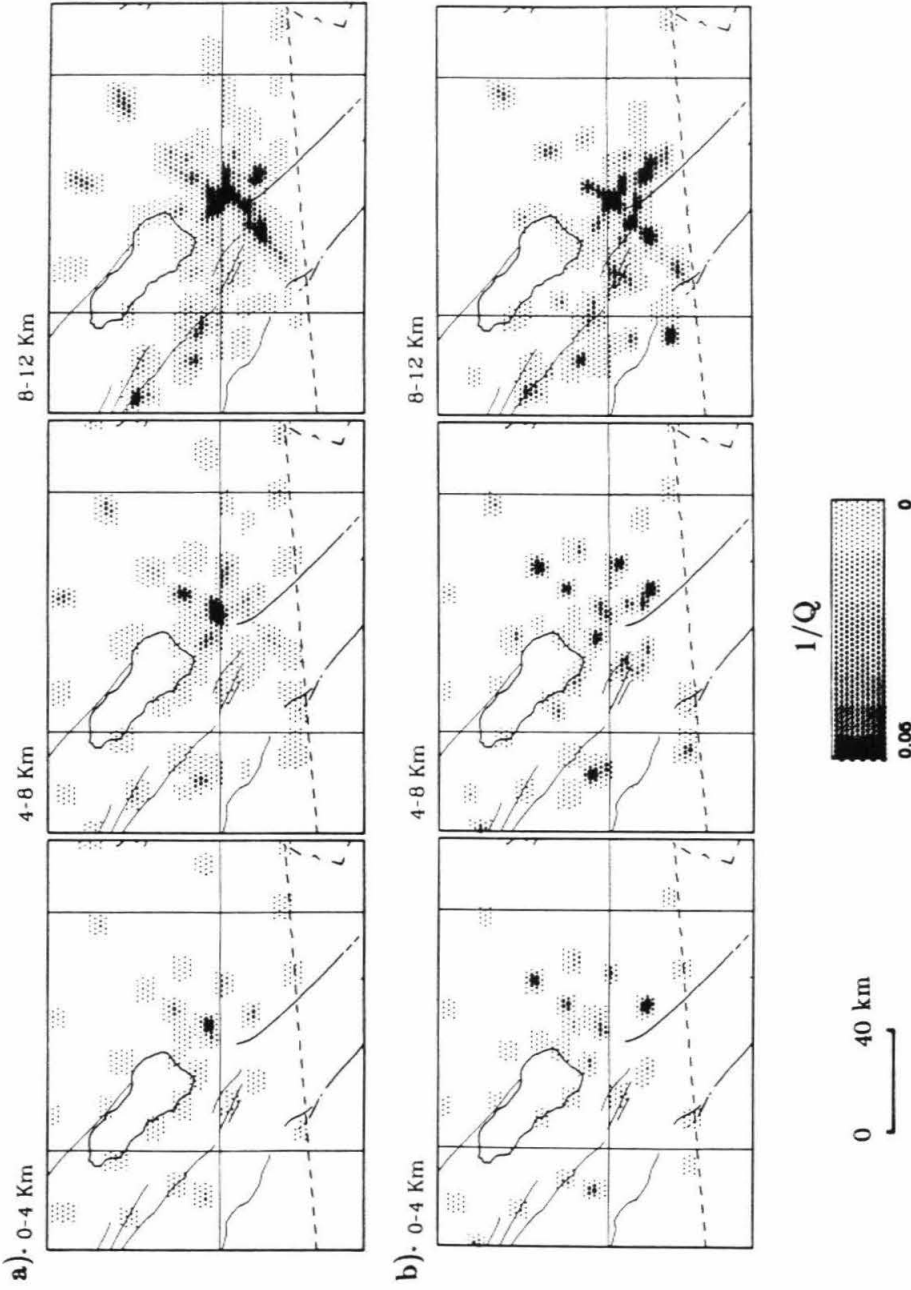


Figure 16b: Results of attenuation inversion using $k_1 k_2 = 1.0$ for Imperial Valley. No positivity constraint was imposed in the inversion. The geometry of the Brawley anomaly is the same as in the results in Figure 11a.

events in the same location, we inverted the data from only 10 out of the original 15 events. Only one event (event #1) is located in the Brawley region. Results of this inversion are shown in Figure 17b. The Brawley anomaly is still clearly imaged at the same location as that imaged by using 15 events (Figure 17a). By using 15 events, we obtained a smooth pattern of anomalous areas, and some anomalies seen in Figure 17b disappeared in Figure 17a. This set of results supports our conclusion that the Brawley anomaly is a real anomaly, not an artifact of inversion of the data set with many events in the area of the anomaly.

1.9 Conclusion

For the Indian-Wells Valley, despite the use of a limited data set of only 16 earthquakes as compared to more than 400 earthquakes in the Walck and Clayton (1987) study of this region, we could resolve an attenuating body with Q_β of approximately 30 in the same location as the slow-velocity anomaly. This shallow attenuating body between 3 and 5 km beneath the Indian-Wells Valley (IWV) extends northward close to the Coso Range. It extends down to the 5-7 km depth range and to the west (Figure 8a-iii) of Indian-Wells Valley, but the anomaly north of the IWV anomaly disappears at this depth range. At the depth range of 7-9 km, the IWV anomaly extends to the west of the Sierra Nevada Fault (Figure 8a-iv). An attenuating body east of the Indian-Wells Valley could be an artifact of ray streaking in a general N-S direction that is due to the poor azimuthal coverage in this vicinity (see Figure 8c-ii and -iii).



Imperial Valley: Attenuation Inversion

Figure 17: Results of attenuation inversion with $k_1k_2=1$ by using a) 15 events and b) 10 events in the Imperial Valley. The 10 events used are events #1, 2, 5, 6, 7, 8, 9, 10, 11 and 12. The general geometry of the Brawley anomaly is very similar to that imaged by using 15 events. Some anomalies shown in b) are probably a result of the poorer ray coverage with less events and are spurious.

For the Imperial Valley, 15 earthquakes were analyzed, and we resolved a slow anomaly and a highly attenuating anomaly in the region of the Brawley seismic zone. Based on the hitcount map (Figure 12), we expect to have good resolution near the Brawley seismic zone, especially in the 8-12 km depth range. Travel-time inversion images a slow velocity anomaly (about 10% slower than the reference velocity model) at a depth range of 8-12 km in the Brawley seismic zone (Figure 10). This slow anomaly extends to the 4-8 km depth range in the same vicinity, but the anomaly decreases in magnitude to about 5% at this depth range. Inversion of the amplitude data shows a highly attenuating body extending from 4 km down to 12 km, which is also in the Brawley seismic zone. The depth range of 8-12 km (Figure 11a-iii) shows a more extensive attenuating anomaly, which is confined to the general area of the Brawley seismic zone. A Q_β value of approximately 20 is obtained for the major attenuating body located at a depth of 8-12 km in the Imperial Valley. The other anomalies shown at the edge of the dense hitcount area are probably artifacts of poor azimuthal coverage. According to the resolution analysis, the anomaly in the depth range of 8-12 km in the vicinity of Brawley is well resolved.

The shallow attenuating anomaly in Coso is probably a magmatic body, as was discussed extensively by Sanders *et al.* (1988) and is supported by the conclusions of Walck and Clayton (1987) and Walck (1988). It is possible that the Imperial Valley attenuating body is of the same nature as the one in Coso because the values for both velocity variations and Q_β are similar. However, the difference in the depth suggests some differences in the cause of such

anomalies. One possibility for the 8 to 12 km depth of the Imperial Valley anomaly is that it is related to the transition from upper to lower crust at a depth of about 10 km (Hearn and Clayton, 1986a). This transition depth is also supported by the maximum depth of seismicity data in the area (Doser and Kanamori, 1986). Another possibility is that it implies an active shear region. By shear region, we mean a region of shattered rocks that is undergoing large-scale shearing. Because of the presence of highly fractured rocks, seismic waves traversing the region are both attenuated and slowed down. Either magmatic or hydrothermal activity also may be responsible for the anomalous structure, though the depth range of 8 to 12 km is probably less favorable for the presence of hydrothermal activity.

Chapter 2

Comparison of Iterative Back-Projection and Generalized No-Block Attenuation Tomography

2.1 Introduction

Geophysical problems often involve inversions of discrete data sets for unknown parameters of Earth. Many inversion algorithms have been developed solely for this type of problem. Pioneering work includes Backus and Gilbert (1968, 1970), Wiggins (1972), Franklin (1970) and Jackson (1979). More recent work in seismology includes Tarantola and Valette (1982) who applied a generalized inversion algorithm to solve nonlinear and linear problems, and Comer and Clayton (1987), who used an iterative back-projection approach to solve linearized problems.

Many inversion techniques involve dividing a study area into blocks and inverting for unknown parameters such as slowness in each block. Tarantola and Valette's (1982) approach utilizes *a priori* information on the unknown parameters and inverts the data for unknowns without dividing the study area into blocks. In contrast, the back-projection approach iteratively back projects the data onto a model space composed of blocks. It processes the data set sequentially and thus can handle a large number of data points.

Most inversion methods in geophysics have been applied to travel-time data to invert for the velocity variations in a medium (Aki and Lee, 1976;

Chou and Booker, 1979; Nercessian *et al.*, 1984; Clayton and Comer, 1987, Hearn and Clayton, 1986a, b; Walck and Clayton, 1988; Walck, 1988). In chapter one of this thesis, we applied a similar method to the amplitude data to determine S-wave quality factor, Q_β , of a medium. In this chapter, we compare Tarantola and Valette's (1982) generalized inversion method and Comer and Clayton's (1987) iterative back-projection method using the same data set. We will refer to Tarantola and Valette's generalized inversion as the 'no-block inversion' or 'generalized inversion without blocks.'

2.2 Inverse problem in Attenuation Tomography

Defining A_i as the observed amplitude, $A_{o i}$ as the original amplitude of ray i , f as the frequency of seismic waves for the data set, Q as the quality factor of the medium, v as the velocity of the medium, \underline{r}_i as the coordinates of ray i in vector form, we obtain:

$$-\ln \left[\frac{A_i}{A_{o i}} \right] = \pi f \int_{L_i(v)} \frac{dl_i}{Q(\underline{r}_i)v(\underline{r}_i)}, \quad (1)$$

where $\int_{L_i(v)} dl_i$ denotes integration along ray i .

An analogy can be drawn at this point to the travel-time equation:

$$t_i = \int_{L_i(s)} dl_i s(\underline{r}_i), \quad (2)$$

where t_i is the total travel time of ray i , s is the slowness of the medium, $\int_{L_i(s)}$ is the integration along the ray path L_i which depends on the slowness s .

In discrete form, Equation (1) becomes

$$-\ln \left[\frac{A_i}{A_{o\ i}} \right] = \sum_{j=1}^N \pi f \frac{l_{ij}}{Q_j v_j} , \quad (3)$$

where l_{ij} is the length of the i^{th} ray in the j^{th} block, Q_j is the quality factor of the j^{th} block and v_j is the velocity of the j^{th} block and N is the total number of blocks in the model. A linearized form of Equation (2) is:

$$\Delta t_i = \sum_{j=1}^{n_p} \Delta s_j l_{ij} , \quad (4)$$

where Δt_i is the residual in travel time for ray i , Δs_j is the differential slowness of the j^{th} block in the medium, and l_{ij} is the length of the i^{th} ray in the j^{th} block.

In the same way that we can directly invert Δt_i for Δs_j in Equation (4), we can invert $-\ln \left[\frac{A_i}{A_{o\ i}} \right]$ for Q_j in Equation (3), using a reference model for v_j .

Complications in the left-hand side of the above equations come from the initial source amplitudes, radiation pattern effects and emergence angles of P- and S-waves, and were discussed in Chapter 1 of this thesis. In the present chapter, we focus on the application of the no-block inversion technique (Tarantola and Valette, 1982) to the attenuation problem and its comparison with the back-projection inversion technique (Comer and Clayton, 1987). We will use the same assumptions as in Chapter 1 in solving the problem.

2.3 Iterative Back-Projection Tomography

In iterative back-projection tomography, we solve a discretized problem in the form

$$d_i = \sum_j l_{ij} p_j, \quad (5)$$

where d_i is the data obtained for ray i , p_j is the unknown parameter for the j^{th} block, and l_{ij} is the length of ray i in the j^{th} block. Note that l_{ij} is 0 for any block not crossed by ray i . The algorithm used in Chapter 1 is exactly the same as the algorithm described by Comer and Clayton (1987) or Walck and Clayton (1987).

Each iteration in the calculation can be described by the following equations:

$$p_j^{(k+1)} = p_j^{(k)} + \frac{\sum_i \left(\frac{d_i^{(k)}}{L_i} \right) l_{ij}}{\mu + \sum_{i=1}^{n_d} l_{ij}} \quad (6a)$$

$$d_i^{(k)} = d_i^{(0)} - \sum_{j=1}^{n_p} l_{ij} p_j^{(k)}, \quad (6b)$$

where k denotes the index of iteration, L_i is the total length of ray i , and μ is a damping constant.

The above algorithm, with $\mu=0$, simply iteratively back projects the data onto each j^{th} block with an appropriate proportion. The proportion is determined by the ratio of the ray length of ray i in the j^{th} block to the total ray length L_i of ray i . The damping factor μ stabilizes the solution. For $\mu=0$, in

case of small $\sum_i l_{ij}$, the value of $p_j^{(k+1)}$ will be large, and therefore less-constrained. In order to reduce this effect, a damping constant is added to the iteration. Choice of the value of the damping constant depends on the data set and is often empirical. In the two case studies to which we applied the back-projection inversion, we used a damping factor of 30. We will give a more intuitive meaning to this damping constant in the section where the two inversion methods are compared.

As was pointed out by Dines and Lytle (1979) and Comer and Clayton (1987), this algorithm is equivalent to a minimization of:

$$\sum_{i=1}^{n_d} \left(d_i^{(0)} - \sum_{j=1}^{n_r} l_{ij} p_j \right)^2 / L_i \quad (6c)$$

This minimization implies that the shorter the path, the more weight the data carry. In other words, we know more about where the possible locations of the anomalies are for a shorter path.

In back-projection tomography, no matrix inversion is necessary, so we can use very small blocks (for example, 2 km x 2 km x 1 km). The back-projection method was applied to two areas in southern California: the Coso-Indian Wells region and Imperial Valley (Figure 1 in Chapter 1). Amplitudes of P- and S-waves were measured on the vertical-component seismograms because horizontal instruments are not available. Sixteen earthquakes were chosen as the data set in the Coso study and fifteen earthquakes for the Imperial Valley area. These two data sets were selected so that they provide good azimuthal and depth coverage, while the amount of computation was

kept at a reasonable level. Details are described in Chapter 1 and will not be presented in this chapter. Inversion results are presented in 1, 2 or 4 km thick depth slices (Figures 2a and 4a for Coso and Imperial Valley, respectively). All results were smoothed by a 9-point filter before presented, so the apparent maximum resolution is 6 km x 6 km. In Figures 2 and 4, filled circles indicate attenuation anomalies. The size of the circles is proportional to the intensity of the anomalies. The scale is in $1/Q$. The attenuation was not determined for areas crossed by less than two rays. These areas remain blank in the figures.

In the back-projection method, since the inverse of the matrix associated with the Equation $\underline{d} = L \cdot \underline{p}$ is not available, we cannot directly construct the classical resolution kernel or the covariance matrix for the model parameters. In order to assess the resolution of the inversion, one can calculate the resolving power of the technique for a data set generated by a synthetic point anomaly. This experiment gives the impulse response of the inversion through a numerical forward calculation. The effect of noise can be indirectly estimated by using random noise as input data. Results of the inversion should then give random parameter values. One can also infer the reliability of the results from the density of the hitcounts in the model. The denser the number of hits in an area, the more reliable the result. However, these numerical tests are indirect.

2.4 Generalized Inversion without Blocks

Since the data sets used in this study are relatively small compared to many of those used in travel-time studies, we can apply the no-block inversion technique to them.

The particular problem of solving for the quality factor $Q(\underline{r})$ is in a continuous form (Equation 1), where \underline{r} denotes the position vector. We can solve the problem directly by the generalized inversion technique without blocks as described by Tarantola and Valette (1982).

This inversion technique is based on the assumption that we can estimate an *a priori* covariance function of parameters C_p and of the data C_d . Here, following Tarantola and Valette (1982), we assume a Gaussian parameter covariance function

$$C_p(\underline{r}, \underline{r}') = \sigma_p^2 \exp\left(-\frac{1}{2} \frac{|\underline{r} - \underline{r}'|^2}{L^2}\right), \quad (7a)$$

where L is the correlation length of the unknowns, σ_p is the *a priori* error in the unknown parameter. Since the data are discrete, C_d is a matrix. We assume that

$$[C_d]_{ij} = (\sigma_{d_i})^2 \delta_{ij}, \quad (7b)$$

which means that $[C_d]$ is a diagonal matrix with its diagonal terms equal to the variances, $\sigma_{d_i}^2$, of the data (no cross correlations in the data space). We also assume that the uncertainties in the data space are uncorrelated to the *a priori* uncertainties in parameter space ($C_{d^o p^o} = 0$).

Using these covariance functions, we solve Equation (1) by the algorithm given by Tarantola and Nercessian (1984):

$$p^{k+1}(\underline{x}) = p^o(\underline{x}) + \pi f \sum_i W_i^k \int_{L_i(\underline{x}^k)} \frac{1}{v_i} dl_i C_{p^o}(\underline{x}, \underline{x}') \quad (8a)$$

$$W_i^k = \sum_j \left[(S^k)^{-1} \right]_{ij} V_j^k \quad (8b)$$

$$\left[S^k \right]_{ij} = (C_{d^o})_{ij} + \pi^2 f^2 \int_{L_i(\underline{x}^k)} \frac{1}{v_i} dl_i \int_{L_j(\underline{x}^k)} \frac{1}{v_j} dl_j C_{p^o}(\underline{x}_i, \underline{x}_j) \quad (8c)$$

$$V_j^k = d_j^o - \pi f \int_{L_j(\underline{x}^k)} \frac{1}{v_j} dl_j p^o(\underline{x}_j) \quad (8d)$$

where $d_j^o = -\ln \left[\frac{A_j}{A_{o_j}} \right]$ and $p(\underline{x}) = 1/Q(\underline{x})$.

The actual problem can be non-linear in the sense that the path in Equation (1) depends on the velocity. Variations in velocity can yield variations in amplitude, but we assume that this effect is small enough that we can carry out the inversion using the initial reference velocity model or use the tomographic velocity structures inverted from travel-time residuals. Therefore, we have a linear problem.

Since the inversion for $1/Q$ is linear, we do not have to iterate to obtain the final model, so we omit k in the equations. Uncertainties, $C_p(\underline{x}, \underline{x}')$, of the final model can be computed by:

$$C_p(\underline{x}, \underline{x}') = C_{p^o}(\underline{x}, \underline{x}') - \sum_i \sum_j \int_{L_i(p)} \frac{\pi f}{v} dl_i \int_{L_j(p)} \frac{\pi f}{v} dl_j C_{p^o}(\underline{x}, \underline{x}_i) \left[S^{-1} \right]_{ij} C_{p^o}(\underline{x}_j, \underline{x}') \quad (9a)$$

The resolution is given by:

$$R(\underline{r}, \underline{r}') = \sum_i \sum_j \int_{L_i(p)} C_{p^0}(\underline{r}, \underline{r}_i) \frac{\pi f}{v(\underline{r}_i)} dl_i \left[S^{-1} \right]_{ij} \frac{\pi f}{v(\underline{r}')} dl_j(\underline{r}'). \quad (9b)$$

The calculation requires only inversion of an $n_{rays} \times n_{rays}$ matrix, where n_{rays} is the number of rays in the data set and the most time consuming part is evaluation of the double integral in Equation (8c). Since n_{rays} is about 300 in our problem, this method can be used efficiently.

The choice of correlation length, L , depends on the resolution one wants to attain, under the condition that the area of interest is well resolved (that is, the error is smaller than the amplitude of the anomaly resolved). In the limit as $|\underline{r} - \underline{r}'| / L \rightarrow 0$ based on our *a priori* assumption (Equation 7a), or if we assume that $C_{p^0}(\underline{r}, \underline{r}') = \sigma_p^2 \delta(\underline{r}, \underline{r}')$, we obtain the Backus and Gilbert (1970) type of generalized inversion with the 'trade-off' parameter, f , which is related to σ_p^2 in the form $1/\sigma_p^2 = f/(1-f)$. As $\sigma_p^2 \rightarrow \infty$, we invert the data with the maximum resolution, with most data explained by the resulting model and the least stability to noise in the data, while $\sigma_p^2 \rightarrow 0$ gives the lowest resolution but most stable solution, and data are not explained. Since the objective of this chapter is to compare the iterative back-projection tomography to the no-block inversion, we will present only results with correlation lengths L that correspond to the resolution of the back-projection results.

2.5 Approximate Form of Back-projection Algorithm

We now show that the algorithm of Comer and Clayton (1987) given by Equation 6a can be approximated from the general algorithm of Tarantola and Valette (1982). Since Comer and Clayton use discrete blocks, we write the algorithm of Tarantola and Valette in discrete form and choose the form of generalized inversion given by Tarantola and Valette (1982), relating $p^{(k)}$ to $p^{(k-1)}$ where (k) is the index of iteration (Equation 25 of Tarantola and Valette (1982)). In discrete form, we have:

$$p_j^{(k)} = p_j^{(k-1)} + \sum_{n=1}^{n_p} [S^{-1}]_{jn} \sum_{i=1}^{n_d} \left\{ \frac{l_{in}}{\sigma_{d_i}^2} \left(d_i - \sum_{r=1}^{n_p} l_{ir} p_r^{(k-1)} \right) - \sum_{r=1}^{n_p} [C_{p^{(o)}}^{-1}]_{nr} (p_r^{(k-1)} - p_r^{(o)}) \right\}, \quad (10)$$

where $[S^{-1}]_{jn}$ is the jn^{th} element of the inverse of matrix S whose elements are s_{jn} :

$$s_{jn} = \sum_{m=1}^{n_d} l_{mj} l_{mn} \frac{1}{\sigma_{d_m}^2} + [C_{p^{(o)}}^{-1}]_{jn}.$$

Comer and Clayton (1987) minimize the norm given by Equation (6c) and Tarantola and Valette (1982) minimize the norm $(\underline{d} - \underline{d}^o)^T C_d^{-1} (\underline{d} - \underline{d}^o) + (\underline{p} - \underline{p}^o)^T C_p^{-1} (\underline{p} - \underline{p}^o)$. Since only a small number of boxes are traversed by a single ray, the matrix L has sparsely distributed non-zero elements. The product $L^T L$ is consequently diagonally dominant. Then if we choose $[C_{p^{(o)}}^{-1}]_{jn} = \frac{1}{\sigma_p^2} \delta_{jn}$, we can approximate Equation (10) by:

$$p_j^{(k)} \approx p_j^{(k-1)} + \quad (11)$$

$$\frac{1}{s_{jj}} \sum_{i=1}^{n_d} \left\{ \frac{l_{ij}}{\sigma_{d_i}^2} \left(d_i - \sum_{r=1}^{n_p} l_{ir} p_r^{(k-1)} \right) - \sum_{r=1}^{n_p} \left[C_{p^{(o)}}^{-1} \right]_{nr} \left(p_r^{(k-1)} - p_r^{(o)} \right) \right\} .$$

We now drop the correction term $\left[C_{p^{(o)}}^{-1} \right] \left(p_r^{(k-1)} - p_r^{(o)} \right)$ in each iteration by assuming that in a linear problem, this correction around a reference point $p_r^{(o)}$ is negligible to the first order; hence, $p_r^{(k-1)} - p_r^{(o)} \rightarrow 0$. Equation (11) then becomes

$$p_j^{(k)} - p_j^{(k-1)} \approx \frac{\sum_{i=1}^{n_d} \frac{l_{ij}}{\sigma_{d_i}^2} \left(d_i - \sum_{r=1}^{n_p} l_{ir} p_r^{(k-1)} \right)}{\sum_{m=1}^{n_d} \frac{l_{mj} l_{mj}}{\sigma_{d_m}^2} + \frac{1}{\sigma_p^2}} . \quad (12)$$

For ray paths that are short relative to the block size, we can assume that $l_{mj} \approx L_m$, where L_m is the total ray length of ray m . Therefore, we have:

$$\sum_{m=1}^{n_d} \frac{l_{mj} l_{mj}}{\sigma_{d_m}^2} \approx \sum_{m=1}^{n_d} l_{mj} \frac{L_m}{\sigma_{d_m}^2} .$$

Equation (12) then becomes

$$p_j^{(k)} - p_j^{(k-1)} \approx \frac{\sum_{i=1}^{n_d} \frac{l_{ij}}{\sigma_{d_i}^2} \left(d_i - \sum_{r=1}^{n_p} l_{ir} p_r^{(k-1)} \right)}{\sum_{m=1}^{n_d} \frac{l_{mj} L_m}{\sigma_{d_m}^2} + \frac{1}{\sigma_p^2}} . \quad (13)$$

In Equation (6a), we see that Comer and Clayton's algorithm applies a $\frac{1}{L_i}$ weighting to the data. In order to have the equivalent weighting, it is

necessary to choose $\sigma_{d_m}^2 = \sigma_d'^2 \frac{L_m}{\Lambda}$, where σ_d' is the average error in data and Λ is a constant of normalization. Then we can write (13) in the form of Comer and Clayton's algorithm (1987):

$$p_j^{(k)} - p_j^{(k-1)} \approx \frac{\sum_{i=1}^{n_d} \frac{l_{ij}}{L_i} \left(d_i - \sum_{r=1}^{n_p} l_{ir} p_r^{(k-1)} \right)}{\sum_{m=1}^{n_d} l_{mj} + \frac{\sigma_d'^2}{\sigma_p^2 \Lambda}} \quad (14)$$

We can assign Λ to the average length of the raypath in the case of slow-inversion or the average sum of partial derivatives in a general case:

$$\Lambda = \frac{1}{n_d} \sum_{m=1}^{n_d} L_m = \frac{1}{n_d} \sum_{m=1}^{n_d} \sum_{n=1}^{n_p} l_{mn} \quad (15)$$

Using the above correspondence between the back-projection tomography and the generalized inverse, we can relate the damping constant μ to the error in the data and the *a priori* error in the parameter by

$$\mu = \frac{\sigma_d'^2}{\sigma_p^2} \frac{n_d}{\sum_{m=1}^{n_d} \sum_{n=1}^{n_p} l_{mn}} \quad (16)$$

If the data are not weighted by $\frac{1}{L}$, the expression of the damping factor is quite simple and is given by:

$$\mu = \frac{\sigma_d'^2}{\sigma_p^2} \quad (17)$$

2.6 Comparison of Results in Case Studies

Results from the back-projection tomography have apparent spatial resolution of 6 km x 6 km x 2 (or 1) km in the case of the Coso-Indian Wells region and 6 km x 6 km x 4 km in the case of Imperial Valley. Hence, we compare the results from the no-block tomography with an L of 4 or 8 km. The empirical damping factor μ was chosen to be 30, based on the condition described by Comer and Clayton (1987). The value of σ_p was chosen to be 100 because, from equation (16), it corresponds to a damping factor of 30 used in the back-projection study.

Results from back-projection are shown in Figures 1a, 2a, 3a and 4a. Blank areas are those crossed by less than two rays. Results from the no-block inversion are shown in Figures 1b, 2b, 3b and 4b for the Coso region and Imperial Valley, respectively. Figures 1b and 3b are for a correlation length of 8 km while Figures 2b and 4b are for a correlation length of 4 km.

The comparison between Figures 2b and 2a and between Figures 4b and 4a demonstrates that the results obtained by the two different methods are very similar. Locations of major anomalies are the same. The no-block technique tends to yield a rounded anomaly because of the *a priori* Gaussian covariance matrix. In the Coso case, since the anomaly resolved by iterative back-projection has a rounded shape, the shapes of the anomalies using both approaches are almost identical. The Imperial Valley anomaly resolved by the iterative back-projection method has a more linear trend. The no-block technique resolved two rounded anomalies at the two ends of the linear trend. In general, the results are very similar.

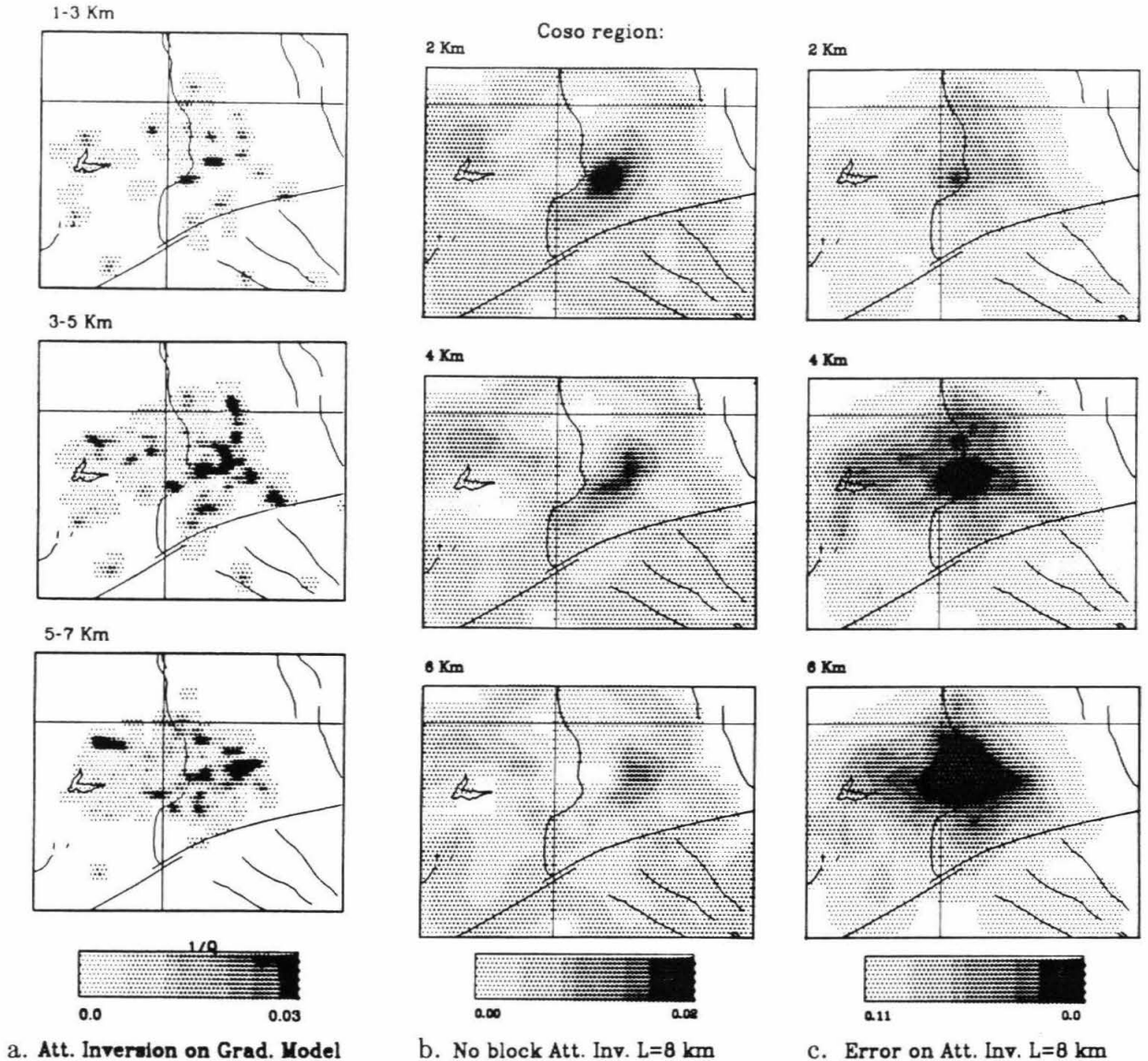


Figure 1: a. Results of attenuation tomography using the iterative back-projection method (Comer and Clayton, 1987) on the Coso-Indian Wells region. Block sizes are 2 km x 2 km x 1.0 km. Actual resolution is 6 km x 6 km x 1 (or 2) km. Depth slices are shown in depths of 1-3 km, 3-5 km and 5-7 km. The major anomaly is the Indian Wells Valley anomaly east of the Sierra Nevada fault. b. Results of attenuation tomography using the no-block inversion technique (Tarantola and Valette, 1982) in the Coso-Indian Wells region. The correlation length is 8 km; *a priori* error on Q is 100. Notice the similarity between the resolved anomaly and the Indian Wells Valley anomaly in Figure 1a. c. Error on the results of attenuation tomography without blocks on the Coso-Indian Wells region with correlation length of 8 km. Amplitude of error is smaller in the area where the major anomaly is located, suggesting that the major anomaly is well resolved.

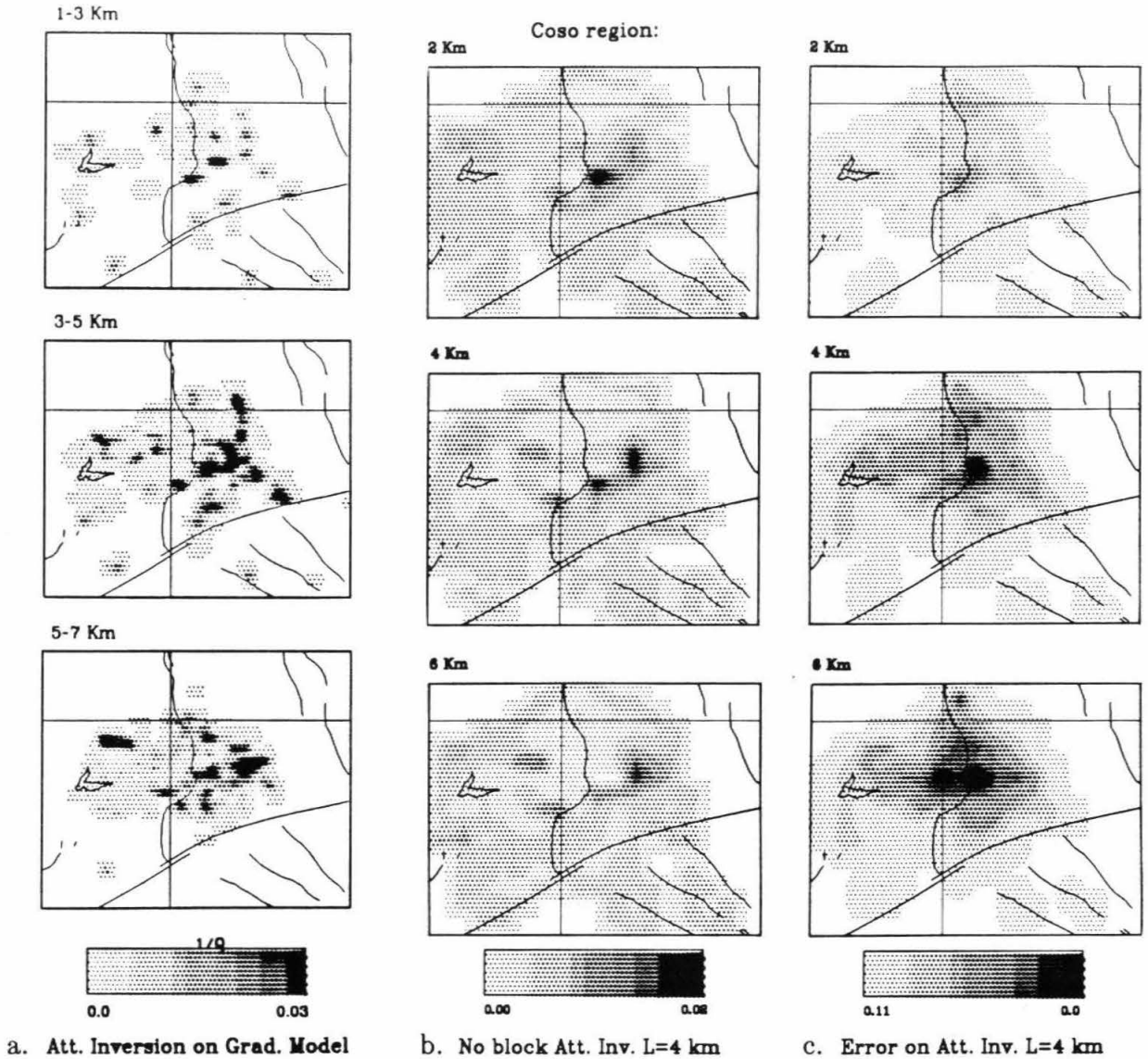


Figure 2: a. Same results of attenuation tomography using iterative back-projection method (Comer and Clayton, 1987) as in Figure 1a. b. Results of attenuation tomography using no-block inversion technique (Tarantola and Valette, 1982) in the same region. The correlation length is 4 km; *a priori* error on Q is 100. c. Error on the results of attenuation tomography without blocks on the Coso-Indian Wells region with correlation length of 4 km. Amplitude of error is also smaller in the area where the major anomaly is located, suggesting that the major anomaly is well resolved.

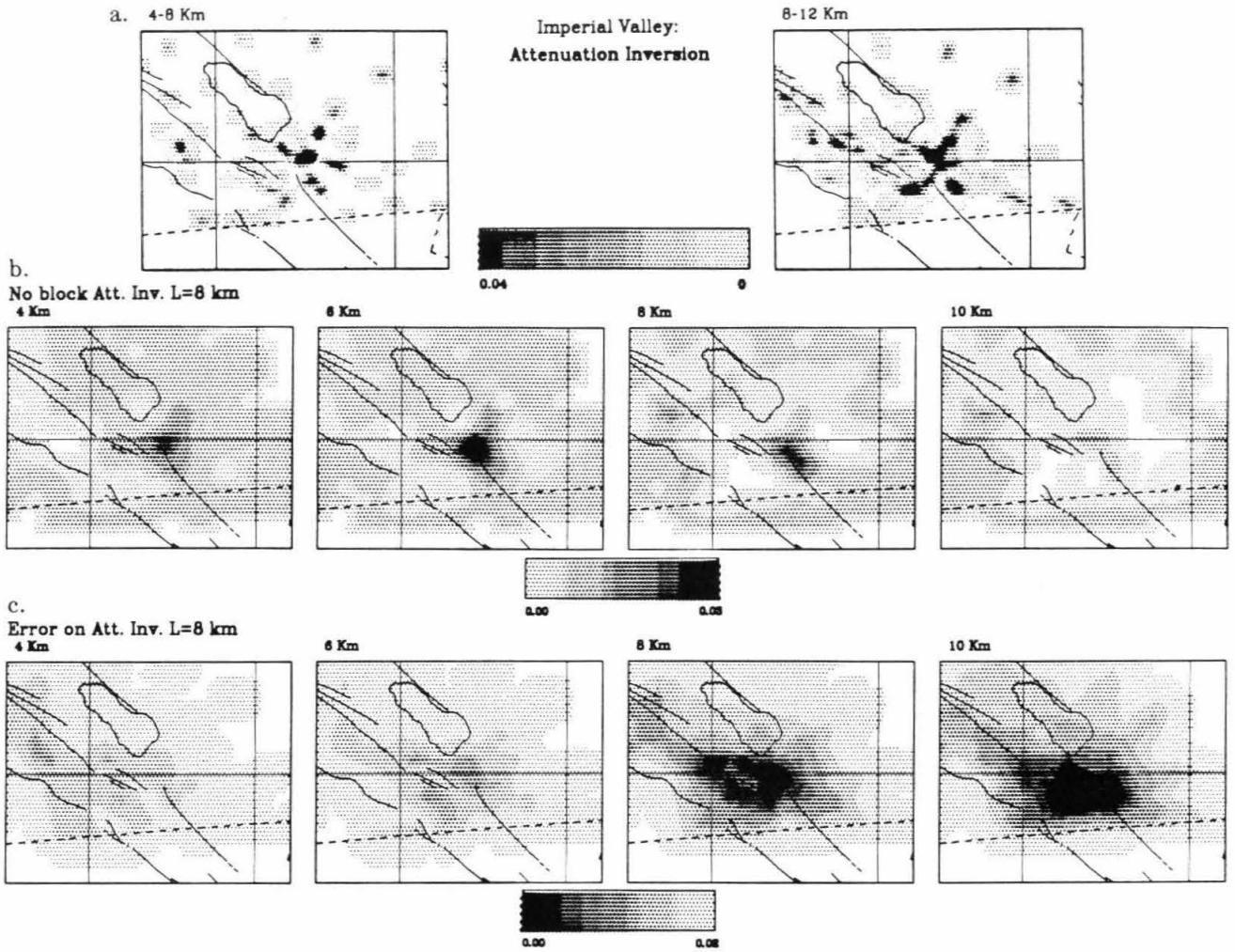


Figure 3: a. Results of attenuation tomography using iterative back-projection method (Comer and Clayton, 1987) on the Imperial Valley. Block sizes are 2 km x 2 km x 1.0 km. Actual resolution is 6 km x 6 km x 4 km. Depth slices are shown in depths of 4-8 km and 8-12 km. The major anomaly is the Brawley anomaly north of of the Imperial fault. b. Results of attenuation tomography using no-block inversion technique (Tarantola and Valette, 1982) in the Coso-Indian Wells region. The correlation length is 8 km; *a priori* error on Q is 100. The major anomaly at Brawley is also resolved. Note the similarities between the location of this anomaly and the location of the one resolved by the iterative back-projection method shown in Figure 3a. c. Error on the results of attenuation tomography without blocks on Imperial Valley with correlation length of 8 km. Amplitude of error is smaller in the area where the major anomaly is located, suggesting that the major anomaly is well resolved.

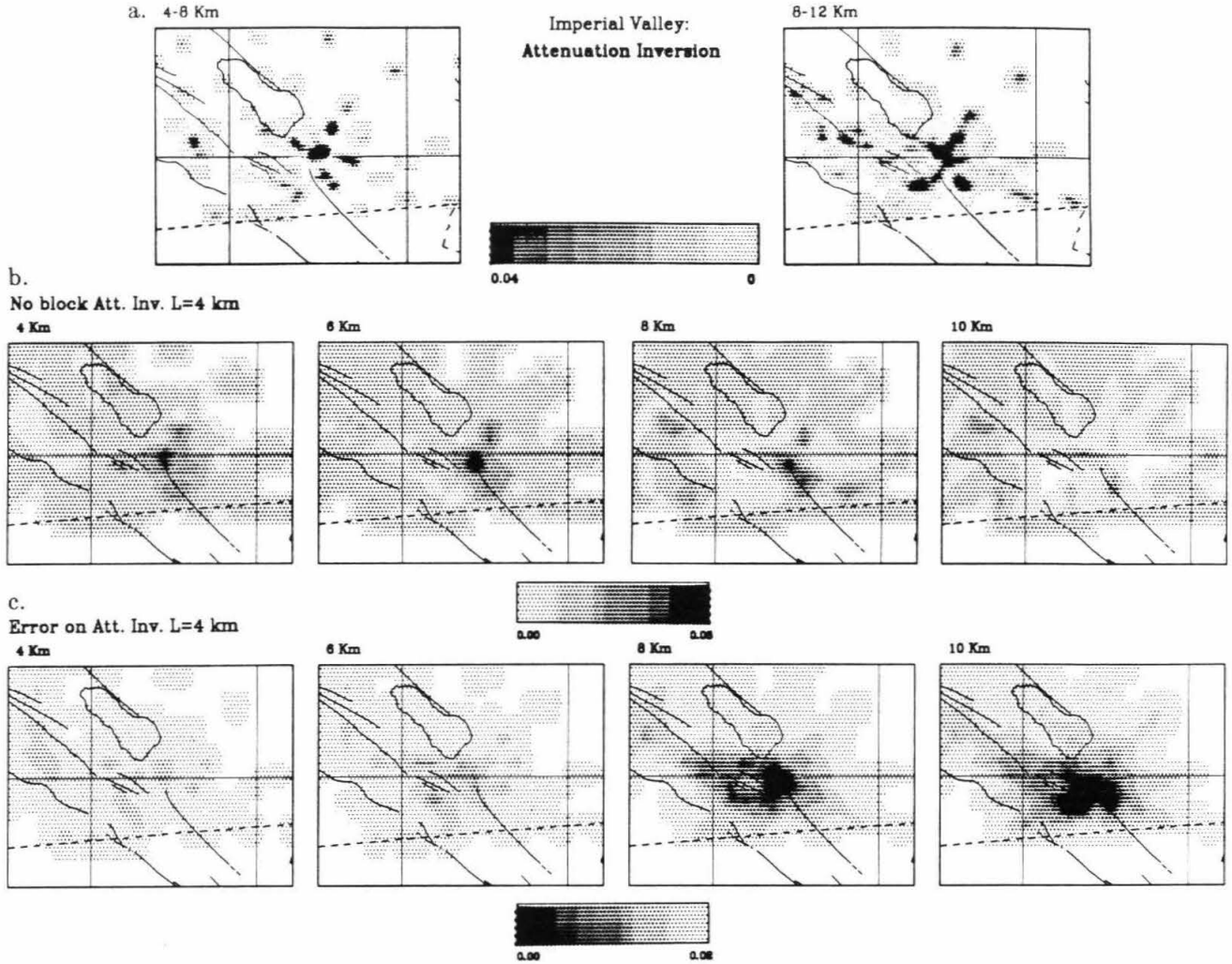


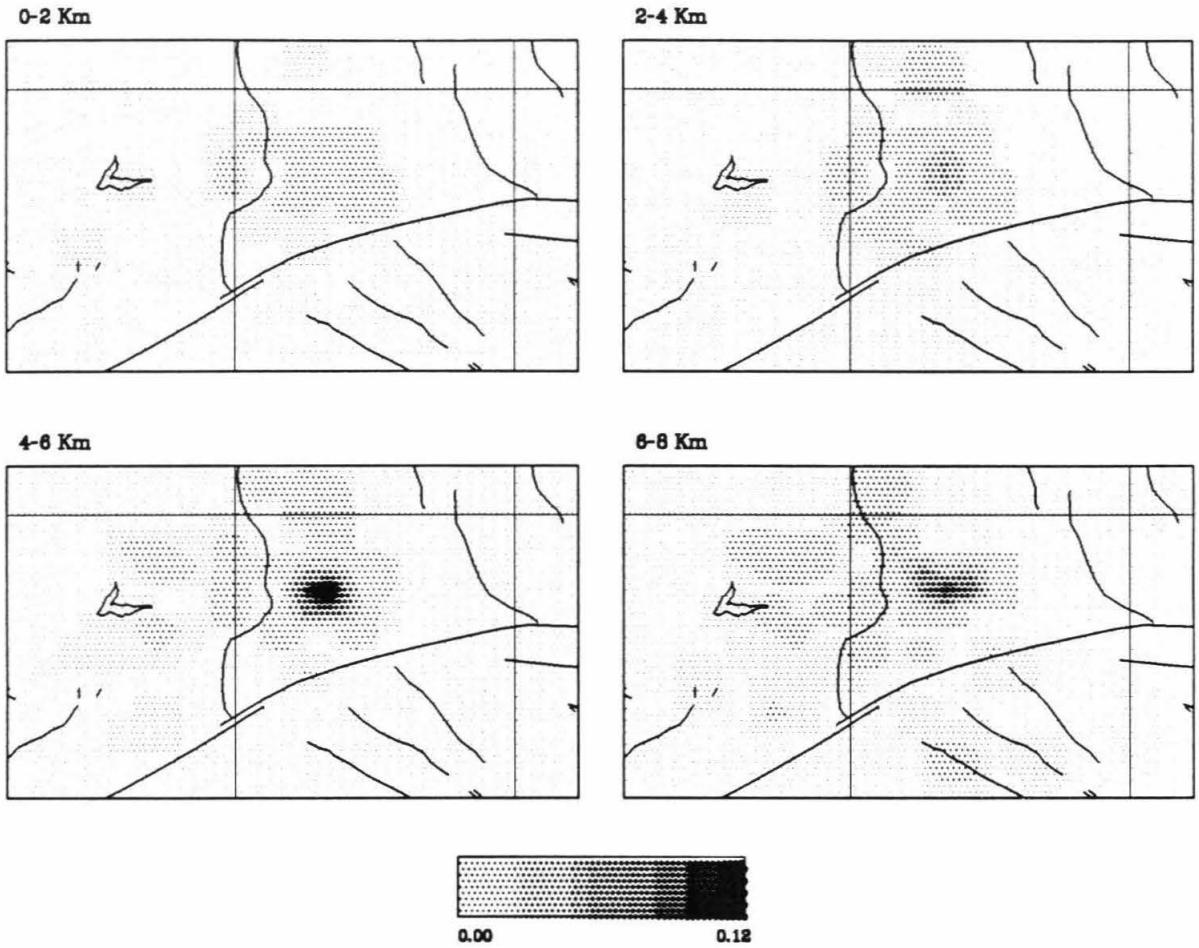
Figure 4: a. Same results of attenuation tomography using the iterative back-projection method (Comer and Clayton, 1987) on the Imperial Valley as in Figure 3a. b. Results of attenuation tomography using no-block inversion technique (Tarantola and Valette, 1982) in the same region. The correlation length is 4 km; *a priori* error on Q is 100. The major anomaly at Brawley is also resolved. Because of the *a priori* assumption that the geometry of the anomaly is Gaussian in shape (see text for details), the shape of the anomaly is not as linear as in Figure 4a but has two rounded anomalies at the two ends of the linear trend. c. Error on the results of attenuation tomography without blocks on Imperial Valley with correlation length of 4 km. Amplitude of error is smaller in the area where the major anomaly is located, suggesting that the major anomaly is well resolved.

The model errors due to random data errors in the inversion can be calculated using Equation 9a and are shown in Figures 1c and 2c for Coso and 3c and 4c for Imperial Valley, respectively. The errors in the area where the anomalies are located are smaller than the anomaly, which means that at the locations of the anomalies, the anomalies are not due to random noise.

More details in the geometry of the anomalies are resolved with a smaller correlation length of 4 km, but the errors for the results with the anomalies are larger than those associated with a correlation length of 8 km (Figures 1c and 2c and Figures 3c and 4c). By comparing results from these two approaches, we are confident that the locations and geometry of major anomalies in both cases are adequately resolved.

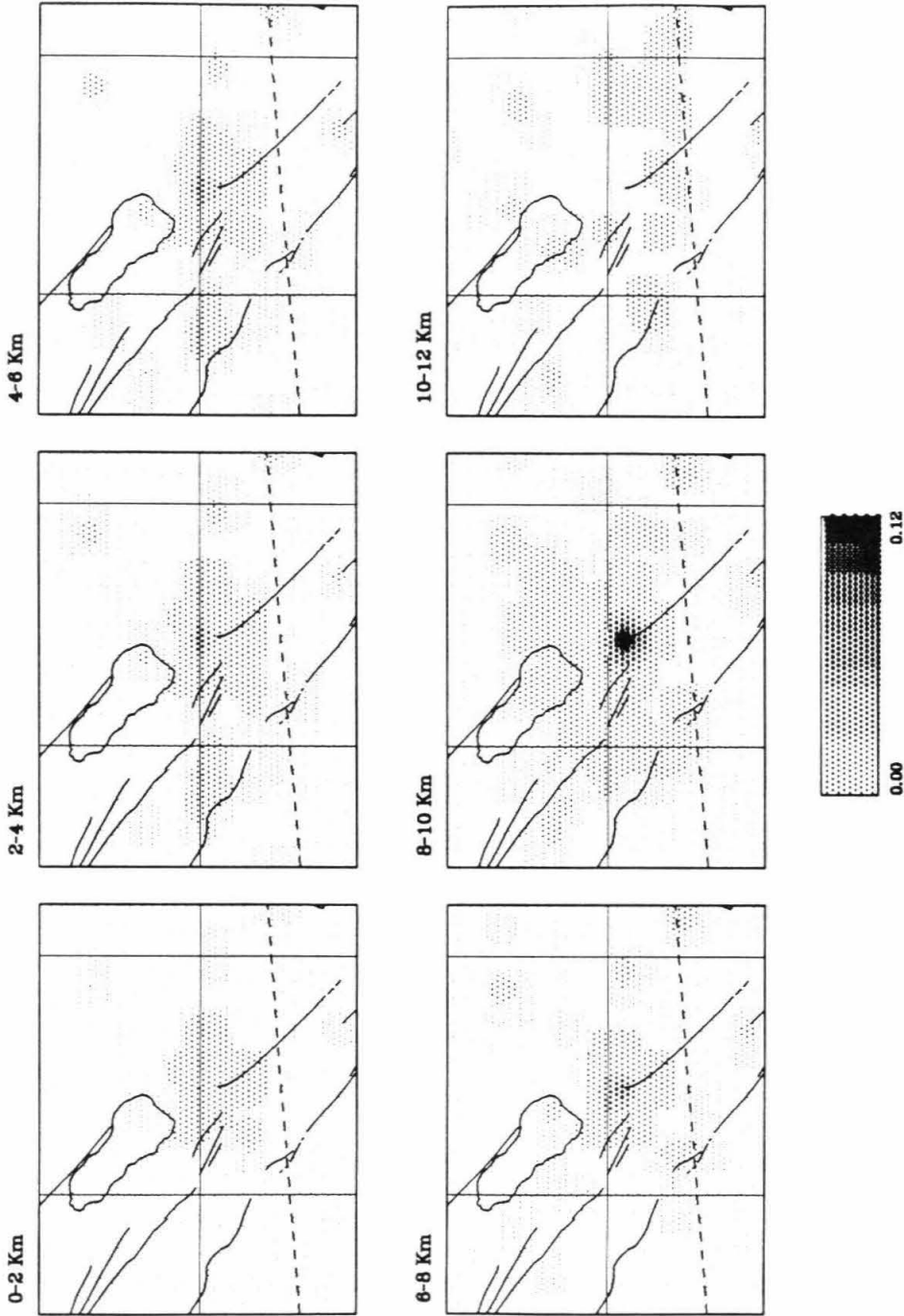
The results from the back-projection method indicate that the quality factor Q of the Coso anomaly is approximately 30, and that the Imperial Valley anomaly is approximately 20. From the no-block inversion technique with a correlation length of 8 km, we obtained a value of approximately 40 for Coso and 37 for Imperial Valley.

The resolution of a target point where the largest anomaly is located in each case is calculated using Equation 9b. The closer the result is to a delta function, the better resolved the target point is. The resolutions at the locations of the anomalies in both cases are shown in Figures 5 and 6 for Coso and Imperial Valley cases at correlation length of 8 km. In the case of Coso, the target point at which resolution is calculated is at 4 km depth and the resolution calculation has its maximum at 4 km in a form close to a delta function (Figure 5), demonstrating that the anomaly is correctly located. In the



Coso region: Resolution on Att. Inv. L=8 km

Figure 5: Resolution at the location of the Indian Wells Valley anomaly is shown in depth slices. The resolution is better if the result is more 'point-like.' We can see that this is the case for this correlation length of 8 km.



Imperial Valley: Resolution on Att. Inv. $L=8$ km

Figure 6: Resolution at the location of the Brawley anomaly is shown in this figure. Again, the result shows a very pointlike resolution at the location of the anomaly, implying good resolution at this location. The target point is situated at 6 km, and the resolution maximum is at 8 km, where the error is smaller (see Figure 3c), as a result of the tradeoff between resolution and error. So we expect that the resolution at the depth of the anomaly is associated with an error of ± 2 km in depth.

Imperial Valley, the target point is situated at 6 km, but the resolution calculation puts the maximum at 8 km depth (Figure 6), where the error is smaller than at 6 km depth (Figure 3c), suggesting a possible 2 km error in the depth of the resolved anomaly. The overall pattern on a map view, however, remains deltalike, which suggests that the resolved geometry of the anomaly is adequate.

2.7 Discussion and Conclusion

We have presented a direct comparison between two different inversion techniques: back-projection and no-block inversion. The results of inversion obtained by these two methods are very similar. Comparison of the results obtained by these two methods allows direct interpretation and investigation of the errors, resolution, and the choice of damping factor in the back-projection technique.

The back-projection technique is a more direct approach to the problem, but errors and resolution can be only indirectly estimated. It is more computationally efficient; for the problems shown in this chapter, 30 iterations take approximately 1.5 hours on a VAX 11/780.

The no-block inversion technique is a more generalized approach, making use of the *a priori* knowledge or assumption on the parameters and data. Resolution is governed not only by the path coverage, but also by the assumed covariance function (where the correlation length L defines the width of any resolved anomaly). By adjusting the covariance function, it is possible to look for the model explaining the data set with a desired resolution. Error

estimates can be directly computed from the final model. Computationally, it is more expensive, requiring more than 5 hours on a VAX 11/780.

Chapter 3

Three-Dimensional Attenuation Structure of Kilauea-East Rift Zone, Hawaii

3.1 Introduction

The Hawaiian hotspot has always been an interesting place for all kinds of geological, geophysical and geochemical studies. It is one of the most active tectonic regions on the surface of Earth and is characterized by frequent volcanic, seismic and geodetic activity. Studies done on Hawaii have concentrated on the seismicity of the island, particularly on the island of Hawaii, where the two most active volcanoes, Kilauea and Mauna Loa, are located. Measurements of gravity and ground deformations have also been done to model the magma chambers and transport systems.

Seismicity of the Island

Figure 1 shows the locations of Kilauea and Mauna Loa, the two most active volcanoes on the Hawaiian Island. Seismic activity on the island of Hawaii is mainly concentrated in the region around Kilauea before the 1975 Mauna Loa eruption. Occurrence of seismic events underneath Kilauea is generally regarded as the effect of eruptions and intrusions of magma. By accurately relocating earthquakes that are related to fluid movements, Ryan *et al.* (1981) developed a three-dimensional picture of the transport system underneath Kilauea, including a shallow magma reservoir inferred by Koyanagi *et*

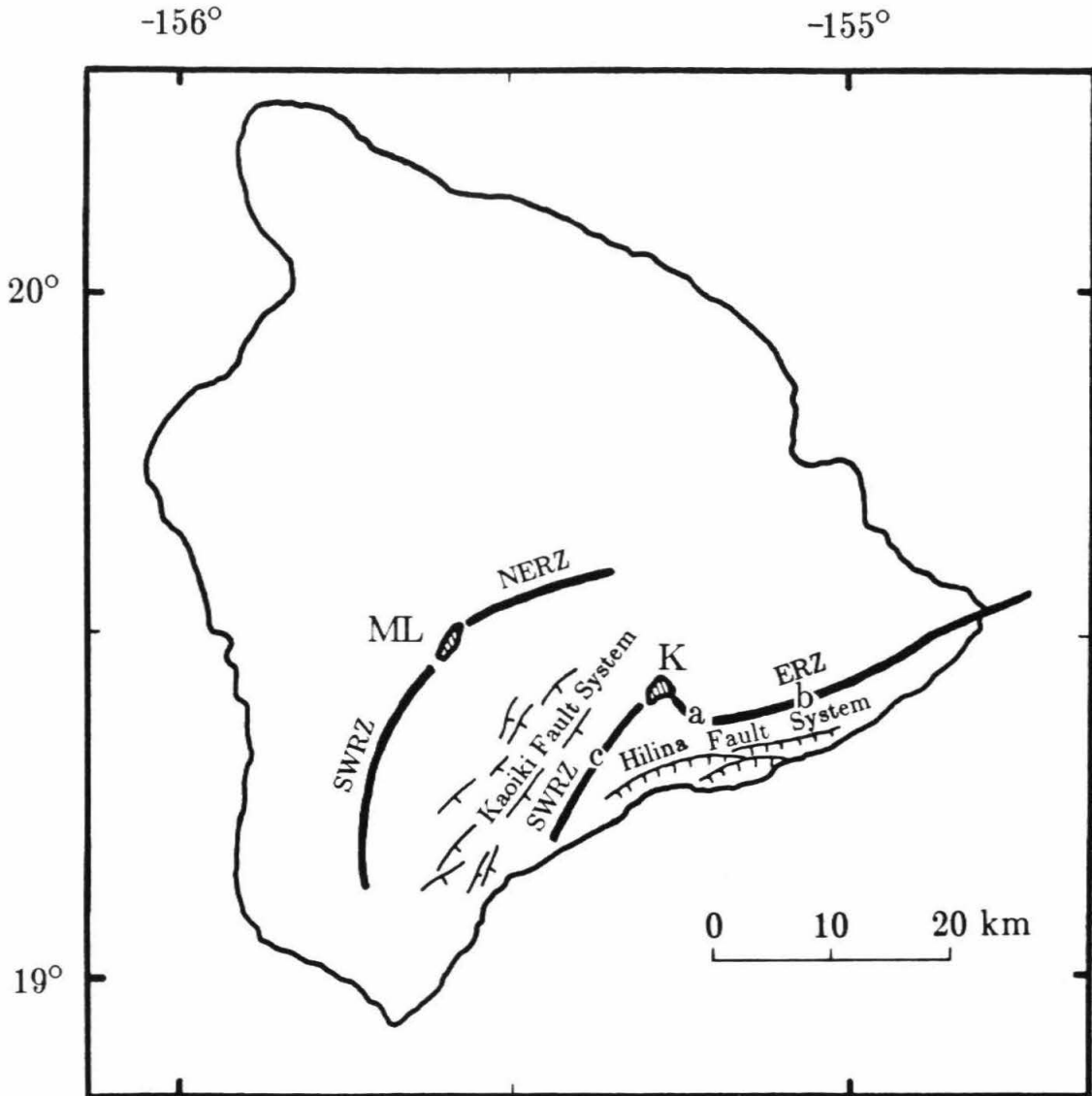


Figure 1: Simplified map of Hawaii (modified from Fornari, 1987). K: Kilauea caldera, ML: Mauna Loa caldera, ERZ: East Rift Zone, SWRZ: Southwest Rift Zone, NERZ: Northeast Rift Zone, a: Mauna Ulu, b: Puu Oo, c: Puu Kou.

al. (1976) from the lack of seismicity at a depth range of about 4-7 km below the Kilauea caldera. Large, deep earthquakes define a continuous path from 40 km upward, which is suggestive of a pathway of magma from the mantle (Klein and Koyanagi, 1986).

Mauna Loa exhibits a similar magma transport system according to seismicity data. The lack of seismicity in the depth range of 15-30 km underneath the caldera suggests the presence of a bigger magma reservoir (Decker *et al.*, 1983). The main purpose of the seismicity work is to make use of accurate locations of earthquakes to delineate the magma transport systems within the volcanoes, extending from the summit region to the laterally radiating rift zones.

Magma Transport Imaging

The inferred transport system underneath the Hawaiian volcanoes is extremely complicated. Modeling of gravity data and ground deformation (Broyles *et al.*, 1979; Eaton, 1962; Jachens and Eaton, 1980) is insufficient to determine such highly complicated structures. Locations of earthquakes were used extensively to delineate different parts of the magma transport system (Koyanagi *et al.*, 1976; Klein and Koyanagi, 1986; Decker *et al.*, 1983). With a more restricted data set, Ryan *et al.* (1981) modeled a three-dimensional magma transport system under Kilauea, but the model was based on the assumption that the earthquakes selected were related to fluid movements. Ellsworth and Koyanagi (1977) inverted teleseismic travel times for lateral variations in structure down to a depth of 70 km beneath Kilauea, but resolution was too low to recover all of the complex structure of the system.

Another inversion was done by Thurber (1984), using local earthquake data. At the aseismic depth range, which was inferred by others to be the shallow magma reservoir, the velocity was found to be low, indicating presence of a fluid phase. The conduit system beneath the shallow magma reservoir was examined by modeling volcanic tremor (Aki and Koyanagi, 1981). The dynamic regions of the magma conduit system extending to nearly 60 km beneath the active volcanoes were broadly outlined using locations of 'long-period' earthquakes (Koyanagi *et al.*, 1987). The long-period events constrain the deep source region between the active volcanoes of Kilauea, Mauna Loa and nearby developing submarine volcano Loihi.

Besides imaging the transport system, data on the petrology of lava give clues to the possible origins of magma under Kilauea and Mauna Loa. Differences in the chemistry of the Kilauea and Mauna Loa lava suggest two distinct magma reservoirs for the two volcanoes (Powers, 1955; Aramaki and Moore, 1969). Failure of the 1984 Mauna Loa event to modulate eruptive phenomena on Kilauea supports the lack of connection at shallow depths. If shallow connections exist between the two magma chambers, geophysical observations should be able to image the connecting system precisely.

Attenuation Structure

Previous geophysical work has addressed various problems like the relationship between magma movement and earthquakes (Koyanagi *et al.*, 1976; Klein and Koyanagi, 1986; Decker *et al.*, 1983, Ryan *et al.*, 1981; Aki and Koyanagi, 1981), presence of magma that causes velocity anomalies (Ellsworth and Koyanagi, 1977; Thurber, 1984), and geodetic deformation that is due to

intrusions and eruptions of magma (Mogi, 1958; Eaton, 1962; Dzurisin *et al.*, 1980, 1984; Broyles *et al.*, 1979; Jachens and Eaton, 1980). None of the previous research has investigated the attenuation of seismic waves by magma. Seismic waves traversing through a magma chamber or a magma conduit are slowed down and attenuated. In this chapter, we invert the amplitude data of local earthquakes beneath the island of Hawaii for the quality factor of the island's crust. The method we use has been described previously and applied to the vertical component data in the Imperial Valley and the Coso-Indian Wells region in southern California (Chapters 1 and 2). As was pointed out in the previous chapters, there is an uncertainty in the application of the method to the vertical components. With the availability of three-components data in the Hawaii network, we examined the horizontal components to obtain an estimate of the uncertainty term k_1 on which the inversions are based. The attenuation structure inverted from the amplitude data is presented in the form of the seismic wave quality factor, Q of the medium.

3.2 Data Analysis

Figure 2 shows the locations of the local stations on the island of Hawaii. There is a total of 53 stations and 90 components.

Events of magnitude 1.0 to 4.5 in the year 1986 are plotted on Figure 3a. Most events are located within the southeast quadrangle of the island. Since most of the geophysically interesting phenomena occur on the Mauna Loa-Kilauea-East Rift Zone quadrangle (MLKERZ), we analyze only events within the boxed area on Figure 3a. To reduce the amount of computation we

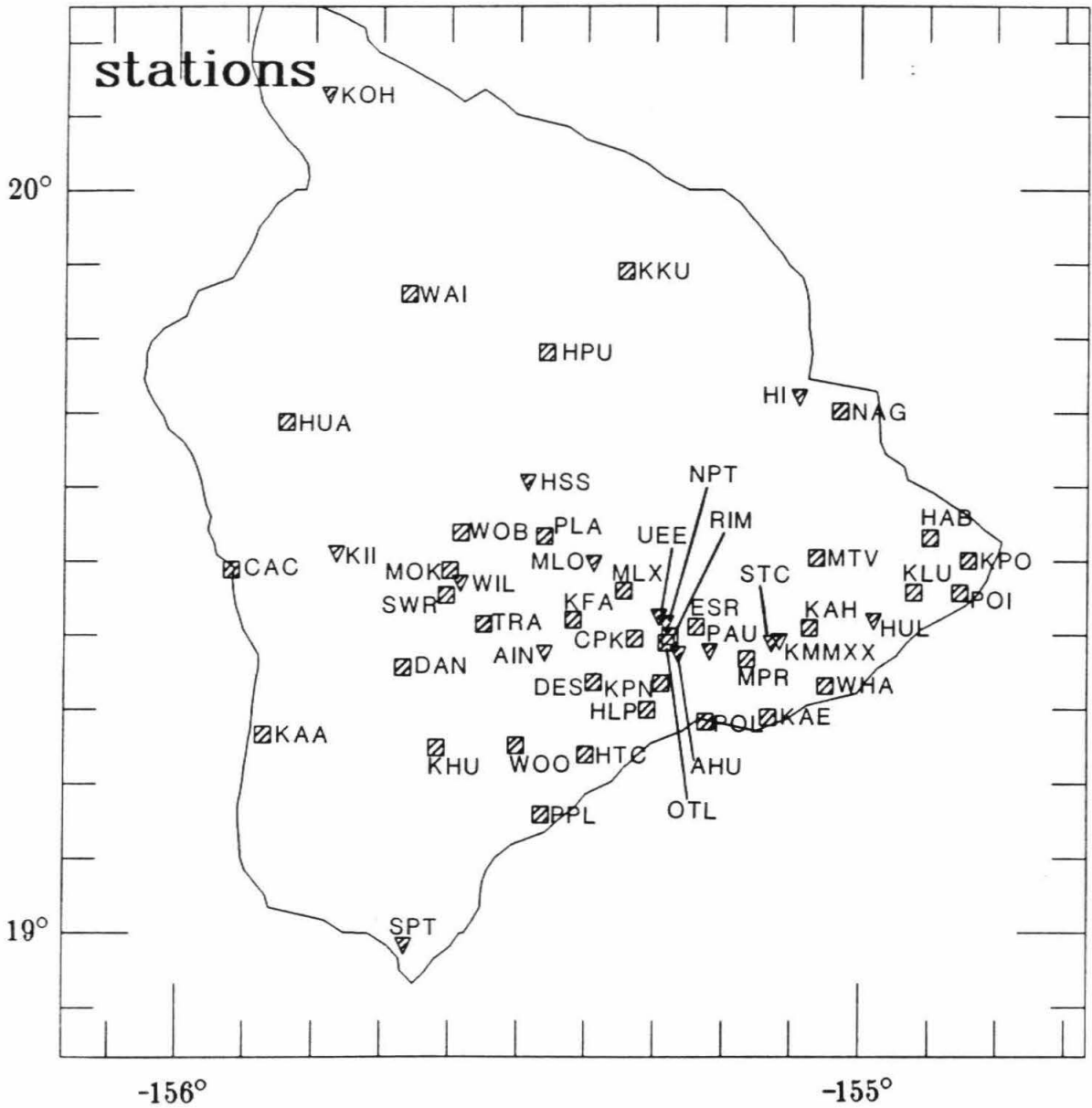


Figure 2: Station locations on the island of Hawaii. Most stations are concentrated in the Kilauea-East Rift Zone quadrangle. Triangles indicate three-component stations and squares indicate vertical-component stations.

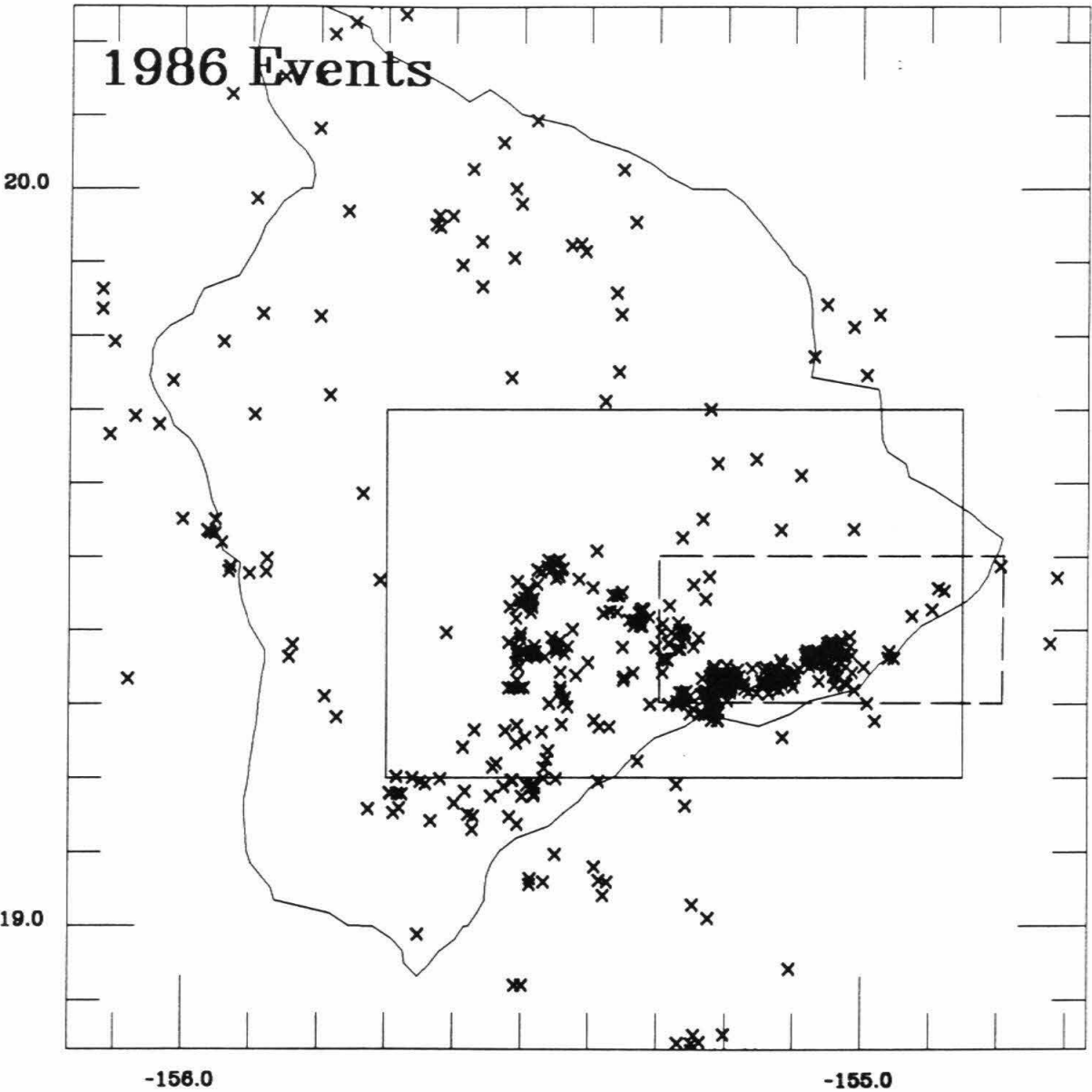
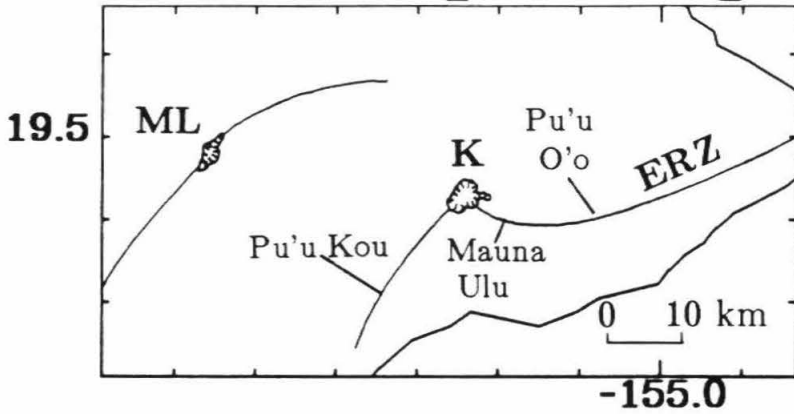


Figure 3a: All local events in the year 1986 with $1.5 \leq M_L \leq 4.5$. There is dense seismicity south of the East Rift Zone. Most seismic activity is centered inside the Kilauea-East Rift Zone quadrangle. Solid boxed area is the Mauna Loa-Kilauea-East Rift Zone (MLKERZ) quadrangle where this inversion study is concentrated. Dashed box outlines the 'zoomed-in' area of the Kilauea-East Rift Zone (KERZ) subquadrangle, where the inversion was also applied for more detailed geometry of the East Rift Zone.

MLKERZ quadrangle



KERZ region

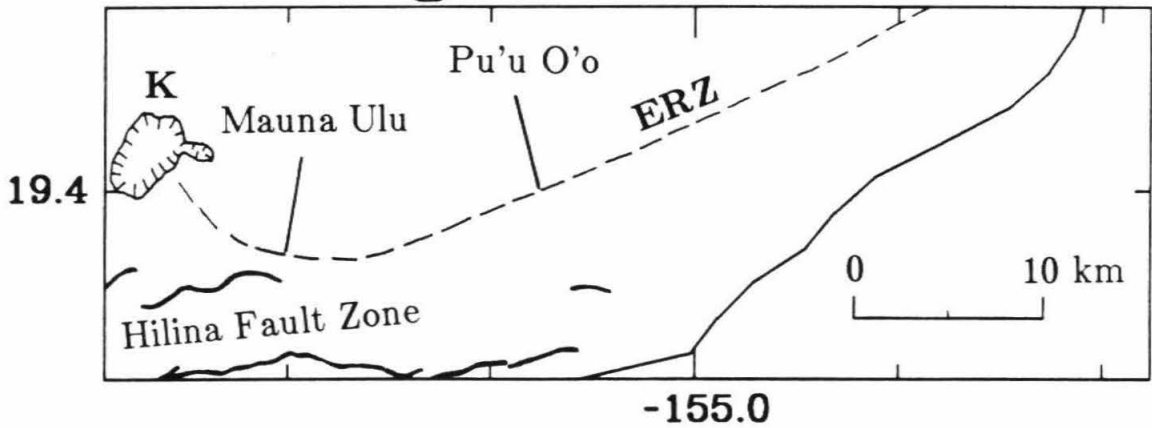


Figure 3b: Major geologic features in the (i) Mauna Loa-Kilauea-East Rift Zone quadrangle (MLKERZ) and (ii) Kilauea-East Rift Zone region (KERZ). ML-Mauna Loa caldera, K-Kilauea caldera, ERZ-East Rift Zone.

further divided the boxed area into small subareas with dimensions of less than 5 km x 5 km, and chose one event to represent each subarea. A total of 63 events was chosen, 37 from the first quarter of the year 1986 and 26 from the entire year to ensure good azimuthal and depth coverage. Tables 1a and b list the locations and depths of these events and Figure 4 shows the events within the MLKERZ quadrangle. Figure 3b shows the important geological sites that will be referenced in the later sections.

The first set of 26 events was chosen for an S-wave screening test. We observed some systematic low S-wave amplitudes in certain azimuthal ranges for some events. Two examples are shown in Figure 5a. The degree of attenuation is less than that found in our previous studies in southern California. In other words, the ratios of S-to-P amplitudes tend to be higher in this study, this is probably because of the lack of thick sedimentary layers on the island of Hawaii. Although the radiation pattern and source effects are not taken into consideration in the screening tests, we still observed possible attenuation anomalies around Kilauea caldera and along the East Rift Zone (Figure 5b). Next, we combined these 26 events and 37 more events from the first quarter of 1986, applied corrections for radiation patterns, included the effects from source amplitudes and instrument response, and inverted the amplitude ratios from more than 1380 seismograms for the attenuation structure of the MLKERZ region and the Kilauea-East Rift Zone (KERZ) subquadrangle for the summit and East Rift Zone of Kilauea. The results will be shown in a later section. A model with smaller block sizes was used for the KERZ subquadrangle but not for the subquadrangle between Kilauea and

Table 1a. List of 26 events used in screening test, back-projection and no-block inversion.

Depths are in km.

| Date | Latitude | Longitude | Depth |
|--------|----------|-----------|-------|
| 860112 | 19.4708 | -155.4157 | 9.34 |
| 860204 | 19.5528 | -155.2342 | 24.76 |
| 860206 | 19.3972 | -155.6112 | 28.05 |
| 860214 | 19.3615 | -155.1177 | 5.11 |
| 860215 | 19.3095 | -155.4357 | 9.75 |
| 860309 | 19.4748 | -155.2240 | 10.32 |
| 860410 | 19.3790 | -155.3507 | 14.08 |
| 860418 | 19.3447 | -155.2923 | 30.95 |
| 860506 | 19.5095 | -155.3897 | 13.93 |
| 860512 | 19.4027 | -155.4250 | 9.40 |
| 860603 | 19.4207 | -154.9247 | 4.76 |
| 860606 | 19.3787 | -155.0485 | 5.24 |
| 860606 | 19.5278 | -155.2643 | 25.10 |
| 860622 | 19.2864 | -154.9776 | 46.85 |
| 860709 | 19.2735 | -155.4400 | 8.89 |
| 860730 | 19.4248 | -155.4865 | 8.79 |
| 860817 | 19.2420 | -155.5853 | 7.04 |
| 860905 | 19.3012 | -155.3103 | 32.44 |
| 860917 | 19.3138 | -155.2217 | 7.55 |
| 860923 | 19.3435 | -155.3353 | 32.24 |
| 860927 | 19.5385 | -155.1185 | 24.86 |
| 861101 | 19.4640 | -155.4770 | 11.12 |
| 861101 | 19.3795 | -155.2467 | 30.63 |
| 861102 | 19.3842 | -155.5188 | 10.93 |
| 861115 | 19.2562 | -155.1153 | 43.79 |
| 861208 | 19.6125 | -155.0897 | 24.98 |

Table 1b. List of 37 events used in attenuation inversion.
Depths are in km.

| Date | Latitude | Longitude | Depth |
|--------|----------|-----------|-------|
| 860104 | 19.3320 | -155.1948 | 9.54 |
| 860104 | 19.3191 | -155.2295 | 4.95 |
| 860105 | 20.0000 | -155.5111 | 44.69 |
| 860106 | 19.3186 | -155.1658 | 4.69 |
| 860112 | 19.3628 | -155.5048 | 9.32 |
| 860113 | 19.3833 | -155.0310 | 5.60 |
| 860114 | 19.3393 | -155.1993 | 6.30 |
| 860114 | 19.3296 | -155.1940 | 4.52 |
| 860115 | 19.2953 | -155.2471 | 6.78 |
| 860117 | 19.3589 | -155.0633 | 10.23 |
| 860123 | 19.3796 | -155.4318 | 9.74 |
| 860124 | 19.3656 | -155.0740 | 7.90 |
| 860128 | 19.3771 | -155.5046 | 10.36 |
| 860128 | 19.3650 | -155.4656 | 9.55 |
| 860129 | 19.7441 | -155.5163 | 37.84 |
| 860131 | 19.3681 | -155.0663 | 2.50 |
| 860131 | 19.3043 | -155.2576 | 7.73 |
| 860202 | 19.4326 | -155.4838 | 8.63 |
| 860205 | 19.3756 | -155.4474 | 9.99 |
| 860205 | 19.3715 | -155.4488 | 10.22 |
| 860211 | 19.4156 | -155.3334 | 2.79 |
| 860215 | 19.4424 | -155.4855 | 10.08 |
| 860215 | 19.4423 | -155.5031 | 10.74 |
| 860216 | 19.3686 | -155.0345 | 4.29 |
| 860224 | 19.2633 | -155.4689 | 10.07 |
| 860224 | 18.6941 | -155.2389 | 15.67 |
| 860224 | 19.3379 | -155.0331 | 8.67 |
| 860226 | 19.3348 | -156.0793 | 40.00 |
| 860301 | 20.0628 | -155.5293 | 28.21 |
| 860301 | 19.4105 | -155.2923 | 16.19 |
| 860305 | 19.3510 | -155.1250 | 49.00 |
| 860305 | 19.3381 | -155.3483 | 30.18 |
| 860311 | 19.4271 | -155.3695 | 11.44 |
| 860311 | 19.3775 | -155.4521 | 10.16 |
| 860314 | 19.3540 | -155.0516 | 4.41 |
| 860330 | 19.3271 | -155.0383 | 4.61 |
| 860330 | 19.4261 | -155.3596 | 10.77 |

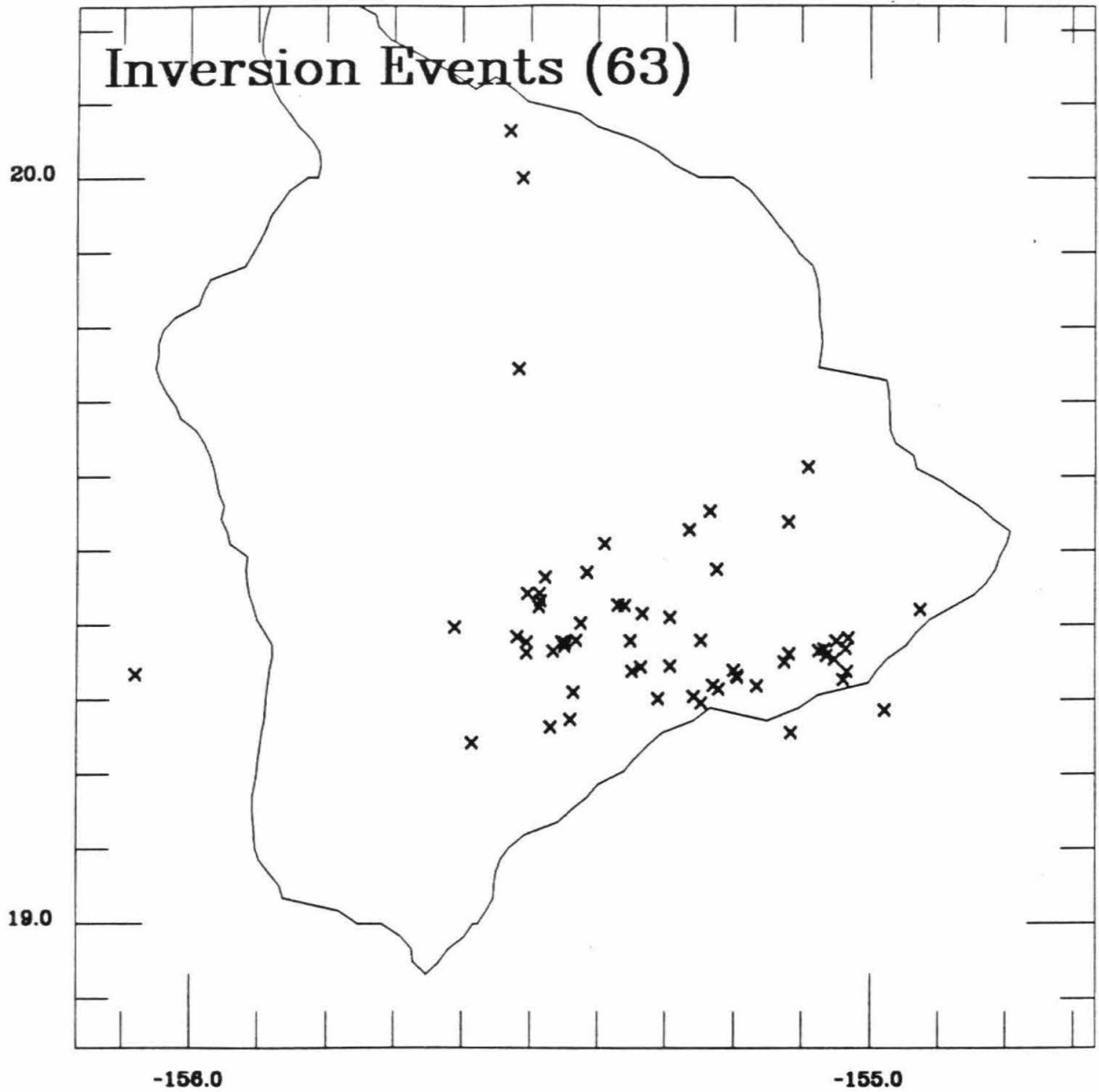


Figure 4: Locations of 63 events used in the back-projection inversion study. Events are chosen on the basis of even depth distribution and ray coverage to the stations. Some events are outside the KERZ (Kilauea-East Rift Zone) quad but were chosen to provide more ray coverage for certain azimuths or more depth coverage.

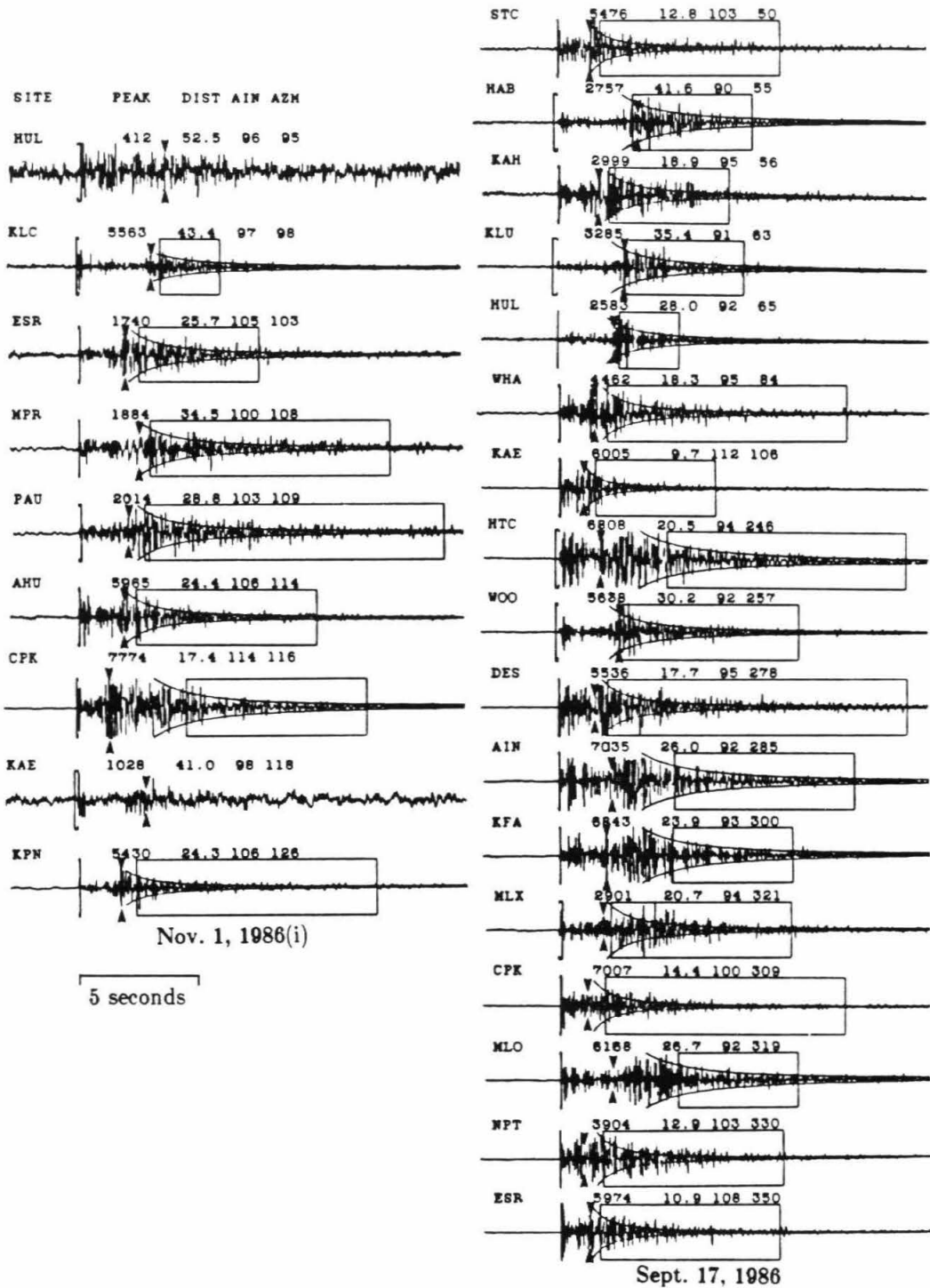


Figure 5a: Examples of azimuthal variations in *S*-to-*P* amplitude ratios. Event on the left occurred on November 1, 1986 at a depth of 11.12 km; event on the right occurred on September 17, 1986 at a depth of 7.55 km. There is more *S*-wave energy in most of the seismograms compared to the two previously studied cases in southern California. Arrows mark the expected arrival times of *S*- or *S_g*-waves.

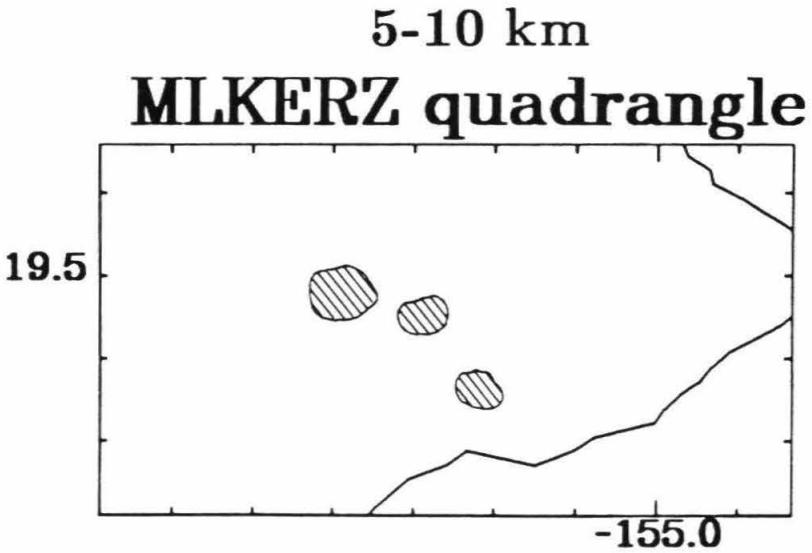
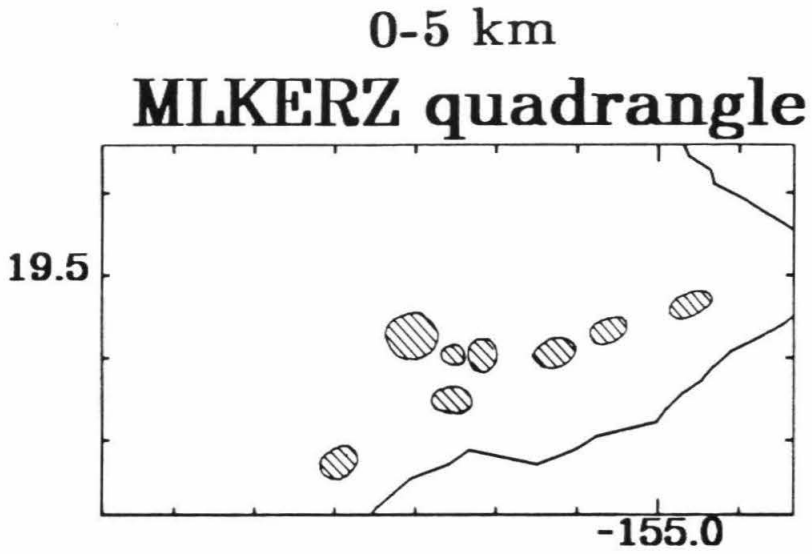


Figure 5b: Results of S-wave screening test using the 26 events listed in Table 1a. Hatched areas indicate areas where ray paths show attenuated S-waves.

Mauna Loa, because most of the 63 events of the selected data set have the densest ray coverage in the KERZ subquadrangle, and the velocity model used is more appropriate for this subquadrangle.

3.3 Description of the Model

The velocity model used is shown in Figure 6. It is the same model as that used routinely to relocate local earthquakes on the island. The model extends down to 16.5 km, below which a constant velocity layer with $V_p = 8.1$ km/s is assumed.

The MLKERZ quadrangle is a highly heterogeneous area. In order to better understand the locations of possible anomalies, we inverted the same data set of more than 1380 rays, using different grid sizes. We first used blocks of 2 km x 2 km x 1 km (46 x 26 x 50 blocks) to resolve the general geometry of the anomalies. Next, we used the same data set to invert for the attenuating structure in a 'zoomed-in' area: the subquadrangle containing the Kilauea caldera and the East Rift Zone (KERZ). Two block sizes were used in each of these areas: 2 km x 2 km x 1 km (28 x 11 x 50 blocks) and 1 km x 1 km x 1 km (55 x 22 x 50 blocks). By systematically inverting the amplitude ratios, using different block sizes for different areas, we hope to resolve more detailed attenuation structures of the subquadrangle, thereby gaining insight into the structure of the magma transport system.

The inversion technique we used is based on Comer and Clayton's (1987) back-projection algorithm and was described in detail in the previous chapters. The algorithm can be written as

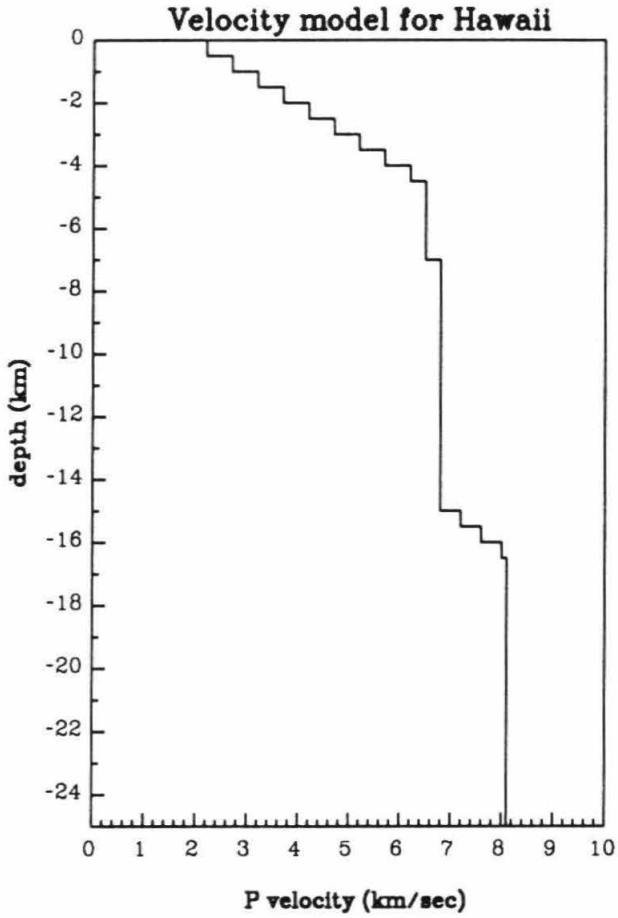


Figure 6: Velocity model used for the location of events, ray-tracing and inversions. The model consists of 14 constant-velocity-layers over a halfspace of 8.1 km/s at a depth of 16.5 km.

$$q_i^{k+1} = q_i^k + \frac{\sum_j \left(\frac{a_j^k}{L_j} \right) m_{ji}}{\mu + \sum_j m_{ji}} \quad (1a)$$

$$a_j^k = a_j^0 - \sum_i m_{ji} q_i^k, \quad (1b)$$

where q_i is the inverse of the quality factor Q_i of the i^{th} block of the medium, a_j is the amplitude ratio of the j^{th} ray, L_j is the total length of ray j , m_{ji} is a matrix equivalent to the length matrix in travel-time inversions (m_{ji} is $\pi s_i l_{ji}$ where l_{ji} is the length matrix, and s_i is the slowness in the i^{th} block), μ is a damping constant, which is empirically taken to be the average of the sum of ray lengths in a block, and superscript k denotes the index of iteration. Since an estimate of μ can be derived from the *a priori* knowledge of the errors in both data and parameters for an underdetermined system (Chapter 2), we used this estimate, which is 60, instead of an empirical estimate from the average ray length in a block, for the inversions. In fact, by using different values of μ , we found that the geometry and locations of anomalies remained the same. The amplitude of the anomalies changed but remained approximately the same. Results shown in the following section are from inversions, using blocks that have a hit count of at least four.

3.4 Results

Results presented in the two following subsections were obtained with the focal mechanism effects removed. Since the routine data processing at the Hawaii Volcano Observatory does not include focal mechanism determinations,

we determined the focal mechanisms using the first motion data. As was pointed out by Crosson and Endo (1981) and Thurber (1987), detailed knowledge of the velocity structure is necessary to determine the focal mechanisms. Since our primary purpose is to correct for the amplitude of the rays taking off from the source rather than to determine the mechanism itself we used the same simple layered structure that was used to locate the events and trace the rays. All the first motion plots and the best-fit fault plane solution for these 63 events are given in the Appendix.

We present the results in the following manner: (i) Results for the MLKERZ region and more detailed results for the KERZ subquad, both with the radiation pattern correction applied; (ii) Results with different values of $k_1 k_2$.

(i) Results of back-projection inversion

We inverted the data from 63 events to determine the structure to a depth of 50 km. Figure 7a shows the results, given in terms of $\frac{1}{Q}$, for depth slices in the MLKERZ quad. Filled circles are attenuating anomalies; size of the circles is proportional to $\frac{1}{Q}$. In general, shallow anomalies are concentrated in the East Rift Zone, the shallow Kilauea magma chamber and the Hilina fault zone. The East Rift Zone and the Hilina fault zone anomalies extend down to a depth of about 8 km. Below this 8 km depth, most of the crust becomes normal except for just west of Puu Kou on the Southwest Rift Zone at 8-12 km depth. It is interesting to note that the shallow Kilauea magma chamber shows up slightly in the 0-4 km depth slice, while the Mauna Loa

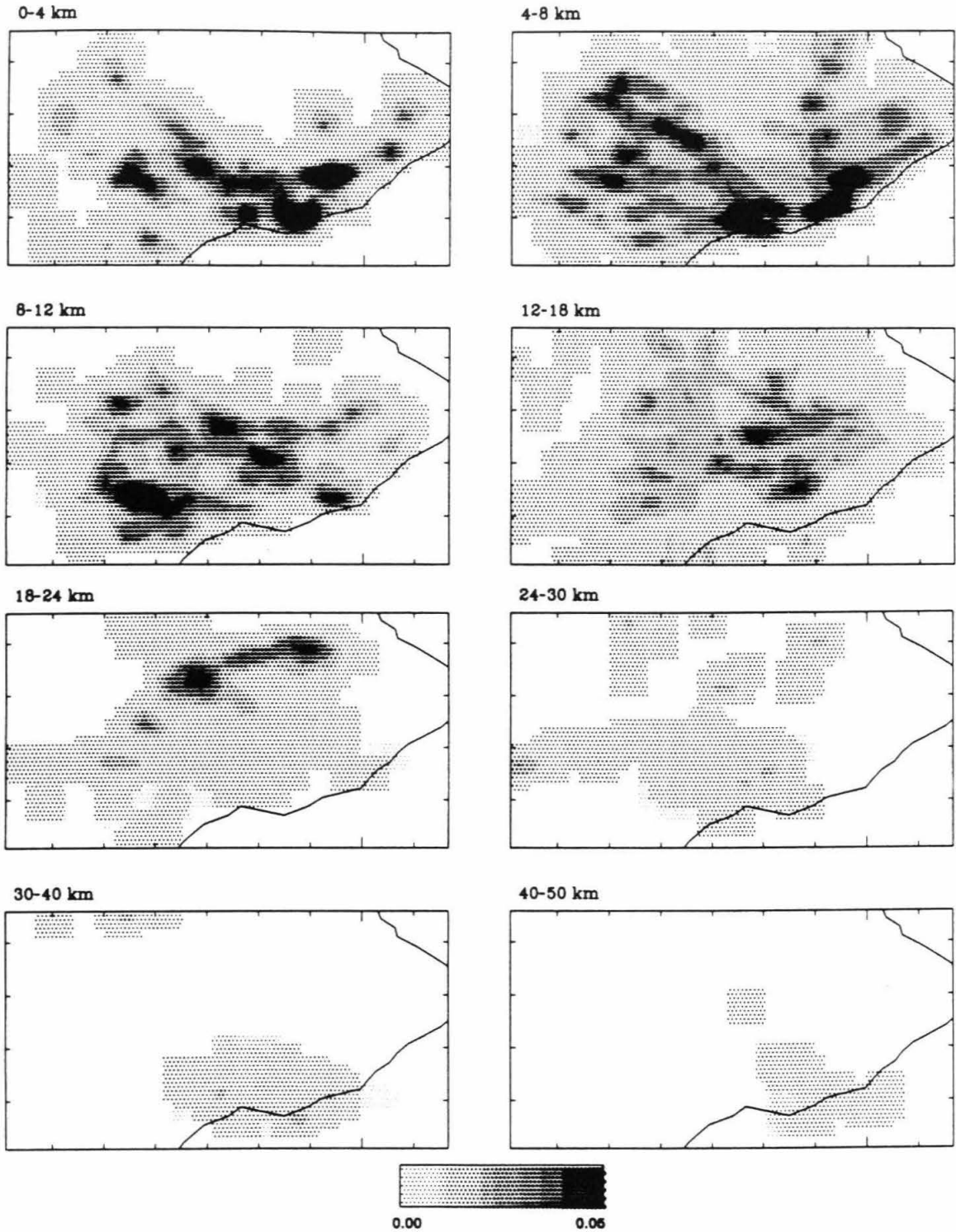


Figure 7a: Results of back-projection attenuation tomography in depth slices of 4, 6 and 10 km thick. Block sizes of 2 km x 2 km x 1 km were used in this inversion. Most attenuation anomalies are located above 18 km deep, below which resolution is poor, and no attenuation anomaly can be imaged. The shallow layers are dominated by attenuation anomalies along the ERZ, Hilina Fault Zone and the two magma chambers.

magma chamber shows up as attenuating at 4-8 km. There is a weak image of a continuous anomaly from the Kilauea chamber to the Mauna Loa chamber in the 4-8 km depth range. Below 12 km, the crust remains mostly normal, although resolution becomes poor below this depth. Only results above 16 km are presented for the MLKERZ quad and above 8 km for the KERZ subquad.

Figure 7b shows the results of the same inversion but in depth slices of 2 km thick. More details of the depth extent of these anomalies are exhibited. The most important feature in this figure is the termination of the East Rift Zone anomaly at about 6 km depth. The continuous channel between Kilauea and the Northwest rift of Mauna Loa is more obvious at the 4-6 km depth slice.

Figure 8a shows the results for the KERZ subquad. The Hilina fault zone is purposely left out of the model so that the detailed geometry of the rift zone can be seen better. This model has the finest resolution (1 km x 1 km x 1 km blocks). The major anomalies in 4-6 km depth coincide well with the geometry of the East Rift Zone. Individual sites of the anomalies also coincide well with several eruption sites, e.g., Mauna Ulu and Puu Oo, and agree very well with the magma reservoirs along the rift zone inferred from seismicity studies (Klein *et al.*, 1987). The depth slices of 4-6 and 6-8 km are very well covered (Figure 8b), so that the anomalies are probably well resolved in these two depth ranges. We will provide a more detailed discussion on the resolution of the inversion later.

(ii) *Effects of variations in $k_1 k_2$*

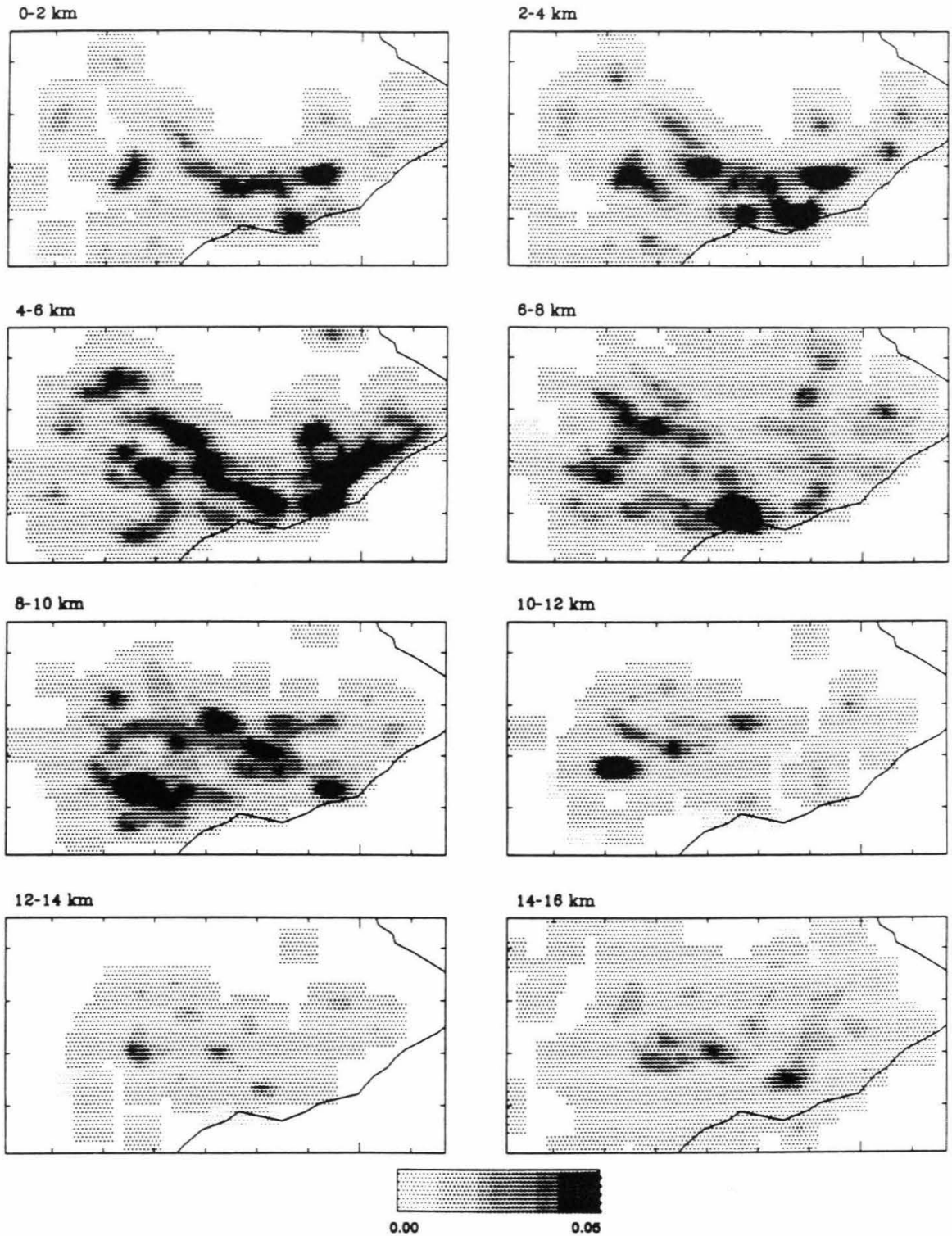


Figure 7b: Results of back-projection attenuation tomography in depth slices of 2 km thick. These are the same results as in Figure 7a but plotted in depth slices of different thickness. More details in the geometry of the anomalies can be resolved. The ERZ anomaly apparently terminates at a depth of about 6-8 km. An interesting 'pipeline' between the Kilauea magma chamber and the Mauna Loa magma chamber appears at a depth of 4-6 km. There is also a dominating anomaly west of Puu Kou along the Southwest Rift Zone in the depth range of 8-10 km.

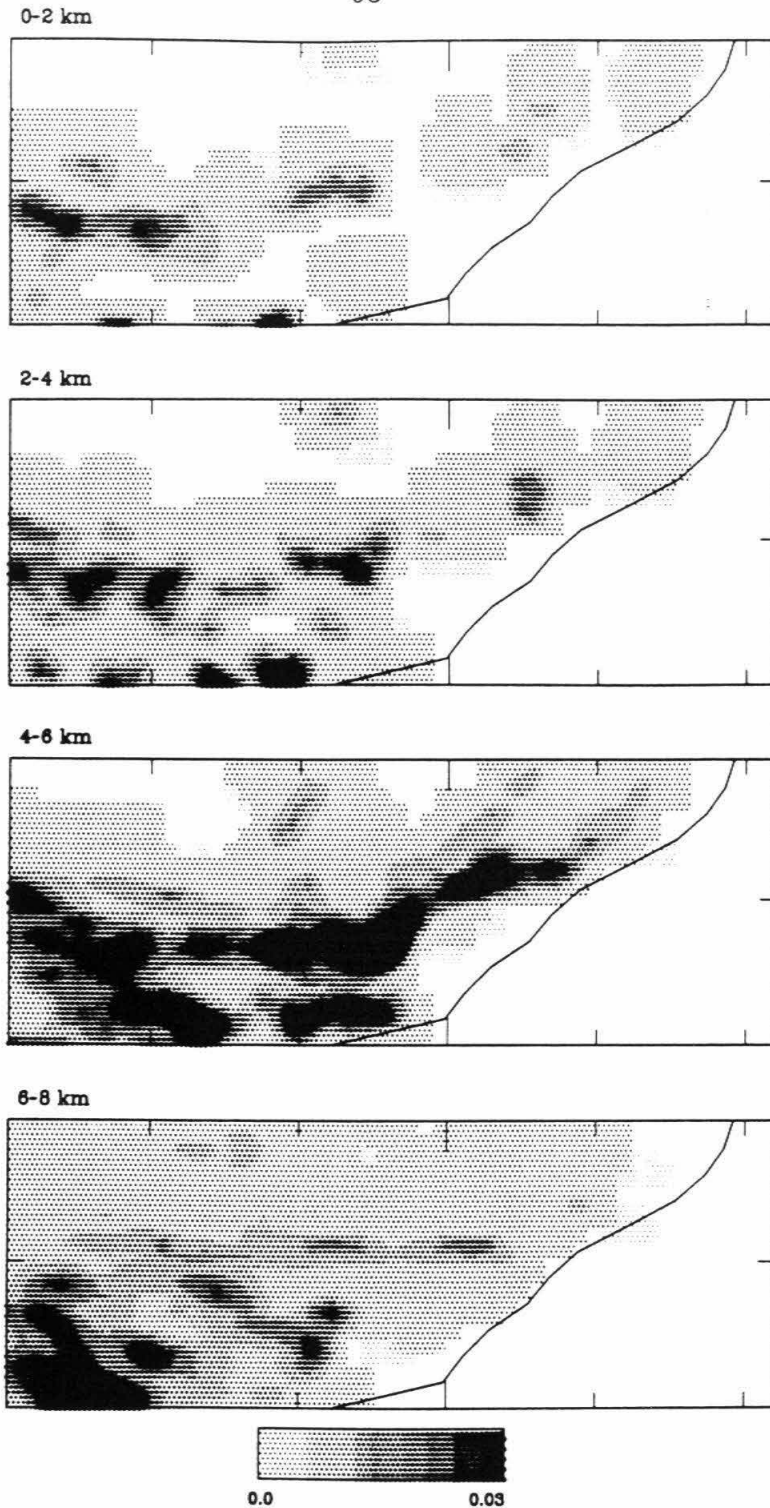


Figure 8a: Results of attenuation tomography in a 'zoomed-in' area of the Kilauea-East Rift Zone subquadrangle (KERZ) in depth slices of 2 km thick. Block sizes are 1 km x 1 km x 1 km. The East Rift Zone is delineated very nicely in the depth slice of 4-6 km. There are indications of small magma reservoirs at Mauna Ulu and Puu Oo, current sites of magma eruptions.

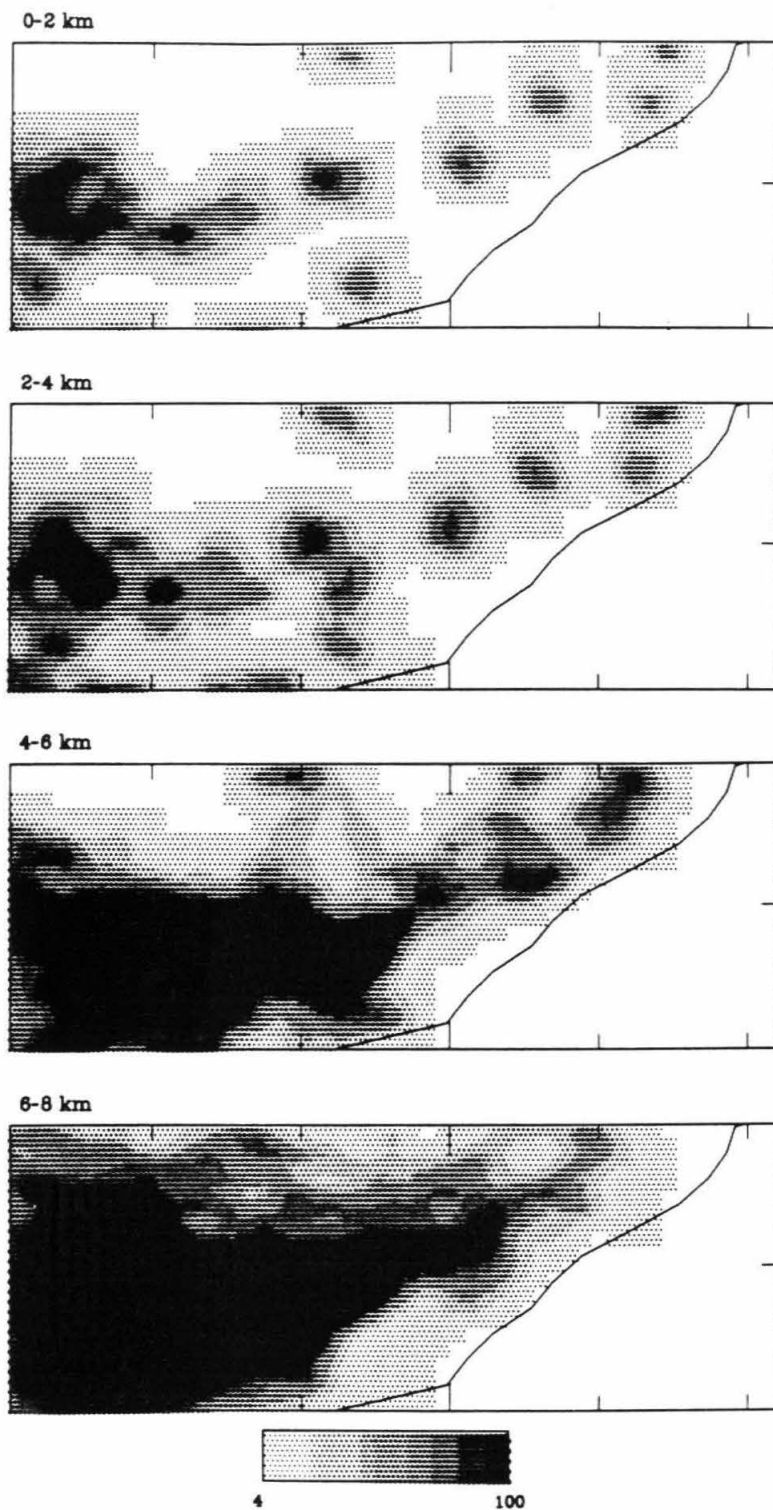


Figure 8b: Hitcount map of the inversion results in Figure 8a. Only blocks with a minimum hitcount of 4 are shaded. The depth slice of 4-6 km where there is an attenuation anomaly is densely covered and therefore is likely to be well resolved.

Results shown in this section are obtained by inversion and include the radiation pattern correction. As was shown in Chapter 1, we have uncertainties in two terms: $k_1 = \frac{I_s}{I_p}$ and $k_2 = \frac{A_s^o}{A_p^o}$, where $I_{s,p}$ are the instrument response for S and P waves and $A_{s,p}^o$ are the initial S,P wave amplitudes at the source (see Chapter 1). For normal double-couple sources, $k_2 \approx \left(\frac{\alpha}{\beta}\right)^3 \approx 5$. In cases where thick layers of soft sediments exist near the surface (e.g., Imperial Valley and the Coso-Indian Wells region, southern California), $k_1 < 1$, which gives the product $k_1 k_2 \approx 1$. We do not expect this situation at Kilauea, and most likely $k_1 \approx 1$, which then gives $k_1 k_2 \approx 5$. Therefore, a higher S-to-P amplitude ratio should be observed in Hawaii compared to the two cases in southern California, if other factors are the same. As was pointed out previously in this chapter, we do observe, in general, a larger amount of S-wave energy on the seismograms compared to the two case studies in southern California presented in Chapter 1. However, there are complications in the Hawaii case too. Stations used in this study are not necessarily located on hard rock sites. Some of the stations are located on hard-fill material, some on loose solidified lava flows, some on ash and cinder deposits. In fact, some stations are situated on nearly a km-thick layer of low-velocity ($\alpha = 1$ km/sec) material. Effects of these complications are hard to assess, because the site responses of the individual stations are not known. In order to examine the effect that is due to the variations in the k_1 term, we tested the inversion by varying the product $k_1 k_2$. A value of $k_1 k_2 > 1$ means that most of the P- and S- waves are arriving at the stations at a large incidence angles, while $k_1 k_2 < 1$

means that rays are arriving at small incidence angles (close to vertical incidence).

We increase k_1k_2 from 1 to 10. The attenuation pattern remains approximately the same with an increase in k_1k_2 value (Figure 9a, b and c). In areas that are densely covered by rays (Figure 9d), attenuating anomalies are well imaged and retain the same geometry with changes in the values of k_1k_2 .

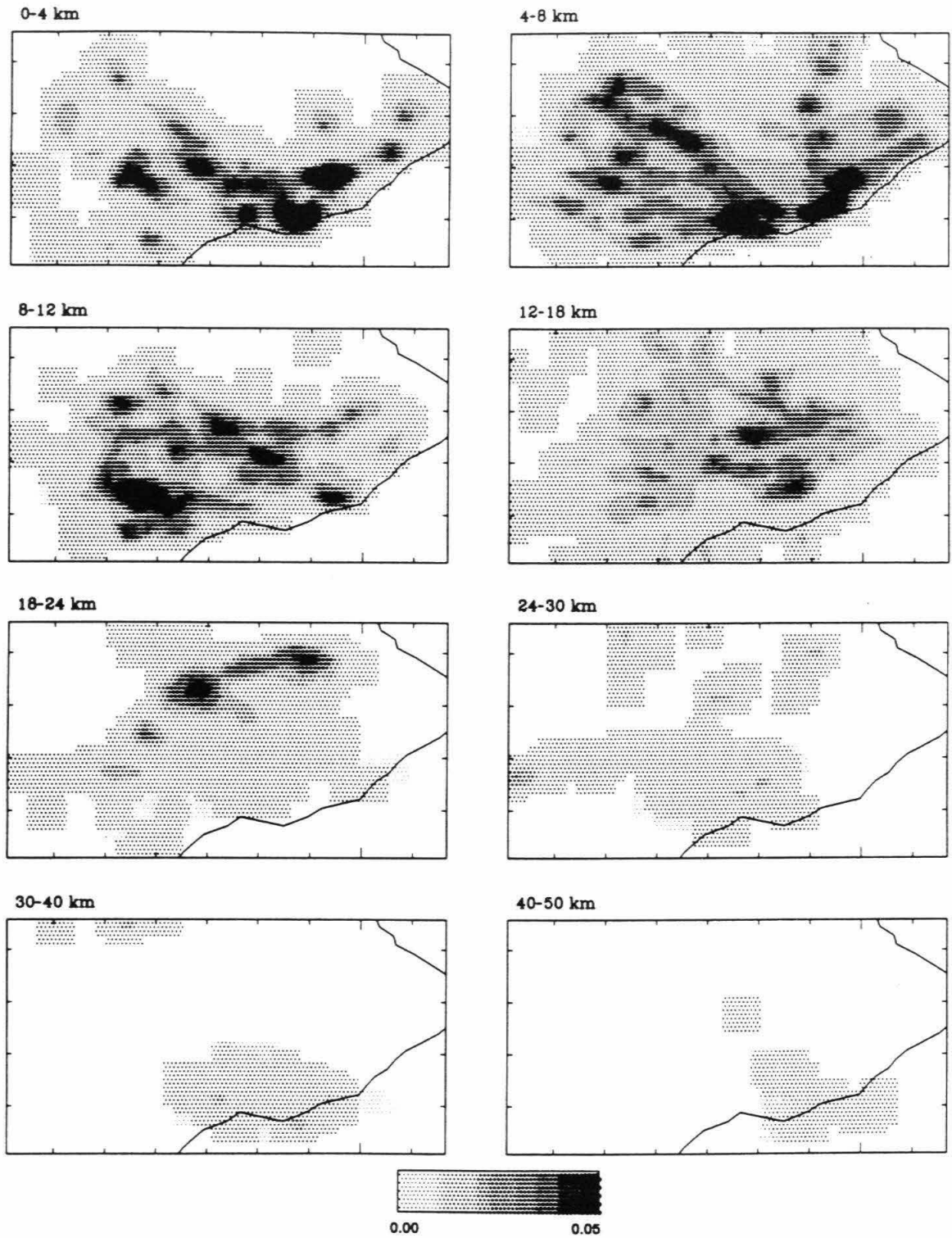
At most stations, we expect that P- and S-waves are arriving at an incidence angle large enough to make $k_2 \approx 1$ (i.e., $k_1k_2 \approx 5$). Since we see from Figures 9a ($k_1k_2=1$) and b ($k_1k_2=5$) that the results are very similar, and that the quality factor is about 20 and 15 for $k_1k_2 = 5$ and 1, respectively, we believe that inversion results with $k_1k_2=1$ are reasonable.

3.5 Resolution of Inversion and Error Estimates

The iterative back-projection tomographic inversion does not provide a direct estimate of the resolution of the inversion and the error estimates of the results. Since the data set used in this study consists of more than 1380 rays, it is not practical to apply the generalized no-block inversion technique as we did in Chapter 2.

In order to utilize the no-block inversion method, we selected the same 26 events as those used in the screening test.

We also applied the iterative back-projection method to this reduced data set to ensure that the results are approximately the same as that obtained using a larger number of events. Blocks of 4 km x 4 km x 1 km were used. Results of the no-block inversion and the back-projection inversion are shown



Hawaii: Attenuation Inversion $k_1k_2=1$

Figure 9a: Attenuation inversion with $k_1k_2 = 1$. Results are the same as in Figure 7a.

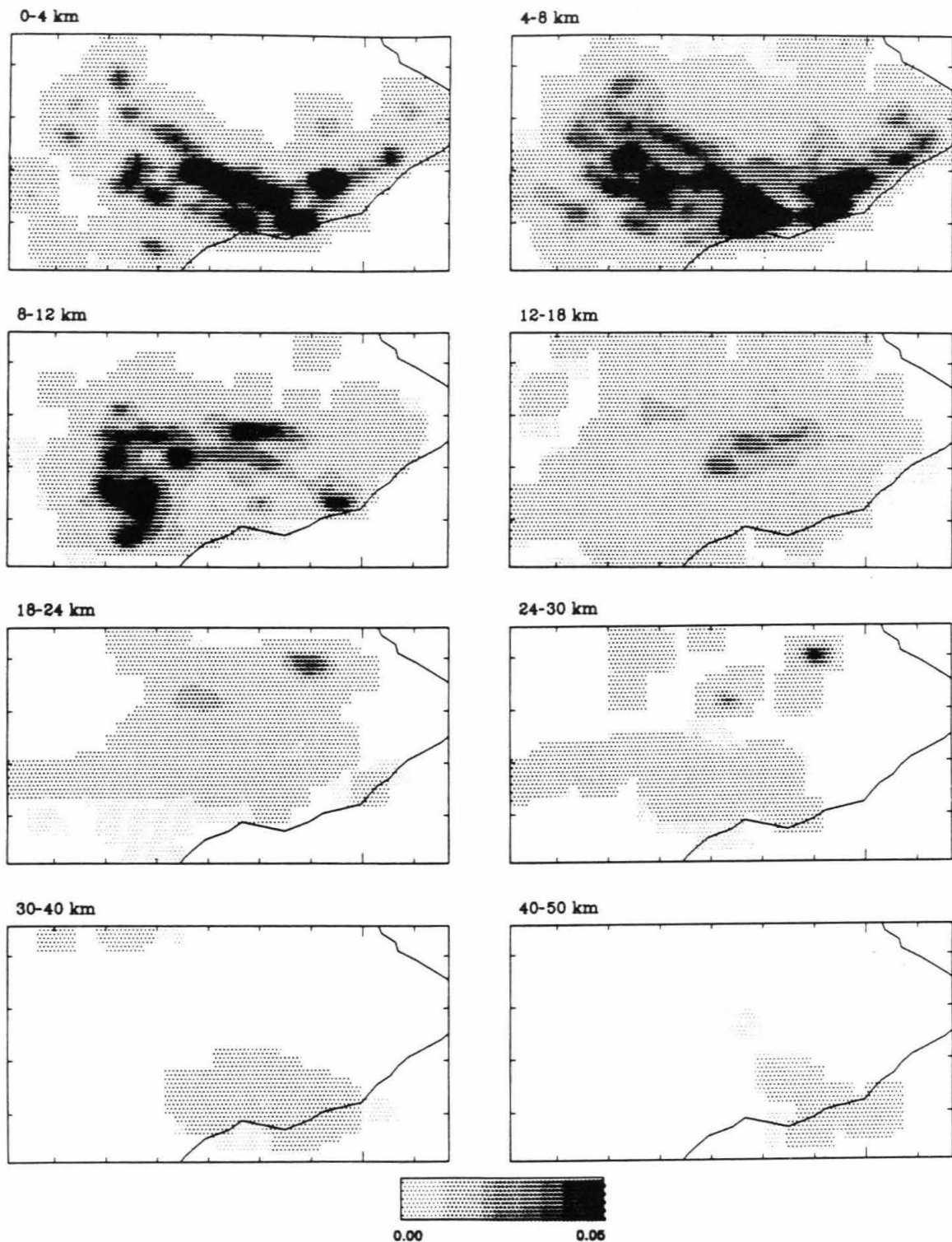


Figure 9b: Attenuation inversion with $k_1k_2 = 5$. This value of k_1k_2 means that rays are in general arriving at a station at an angle further from vertical incidence. More intense anomalies are imaged in this case, but in general the geometry of the anomalies imaged remain the same. Minimum Q value remains approximately at 20.

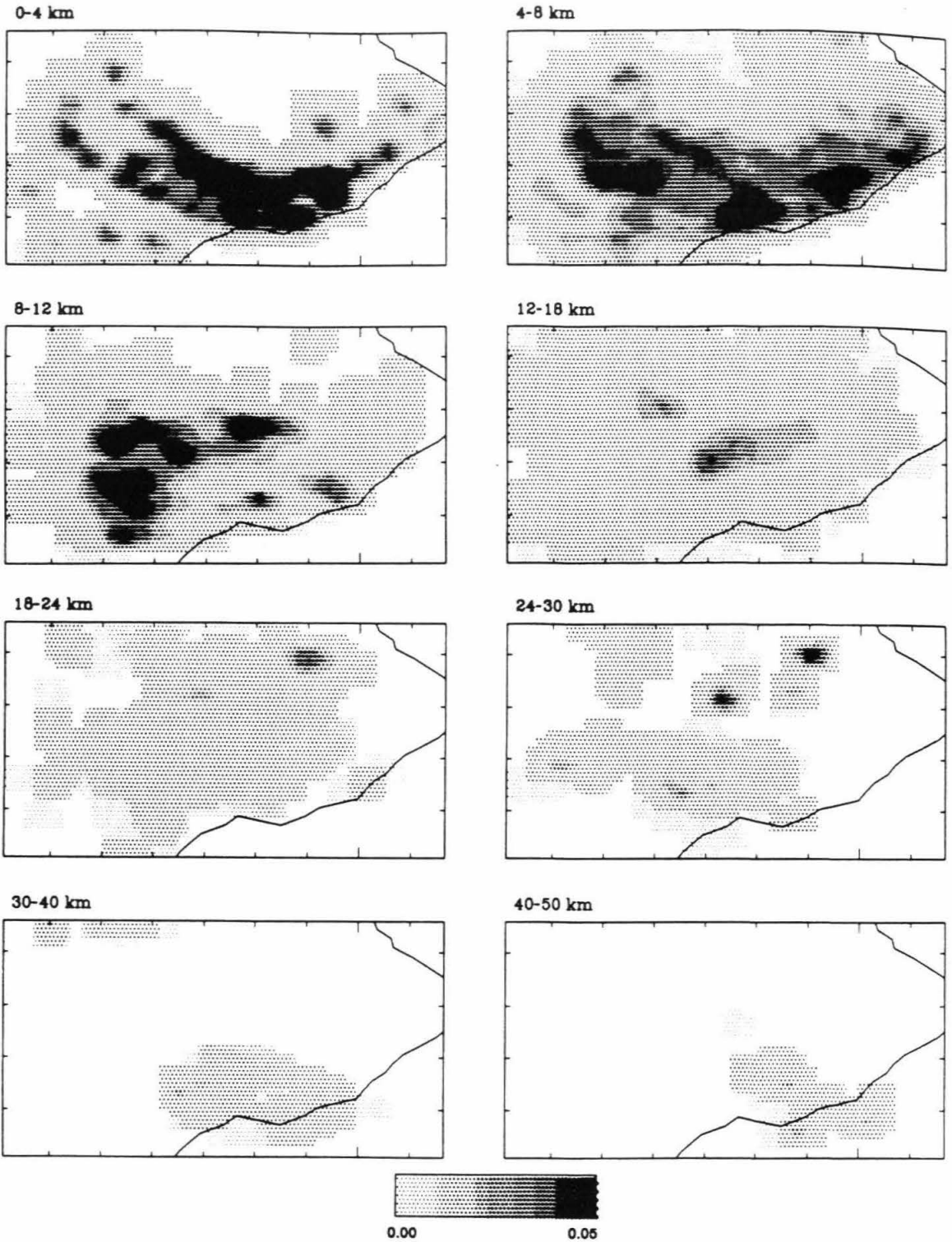


Figure 9c: Attenuation inversion with $k_1k_2 = 10$. This value of k_1k_2 means that rays are in general arriving at a station at an angle far from vertical incidence. Even more intense anomalies are imaged in this case, compared to Figure 9b, but again in general the geometry of the anomalies imaged remain the same as in Figure 9a. Minimum Q value remains approximately at 20.

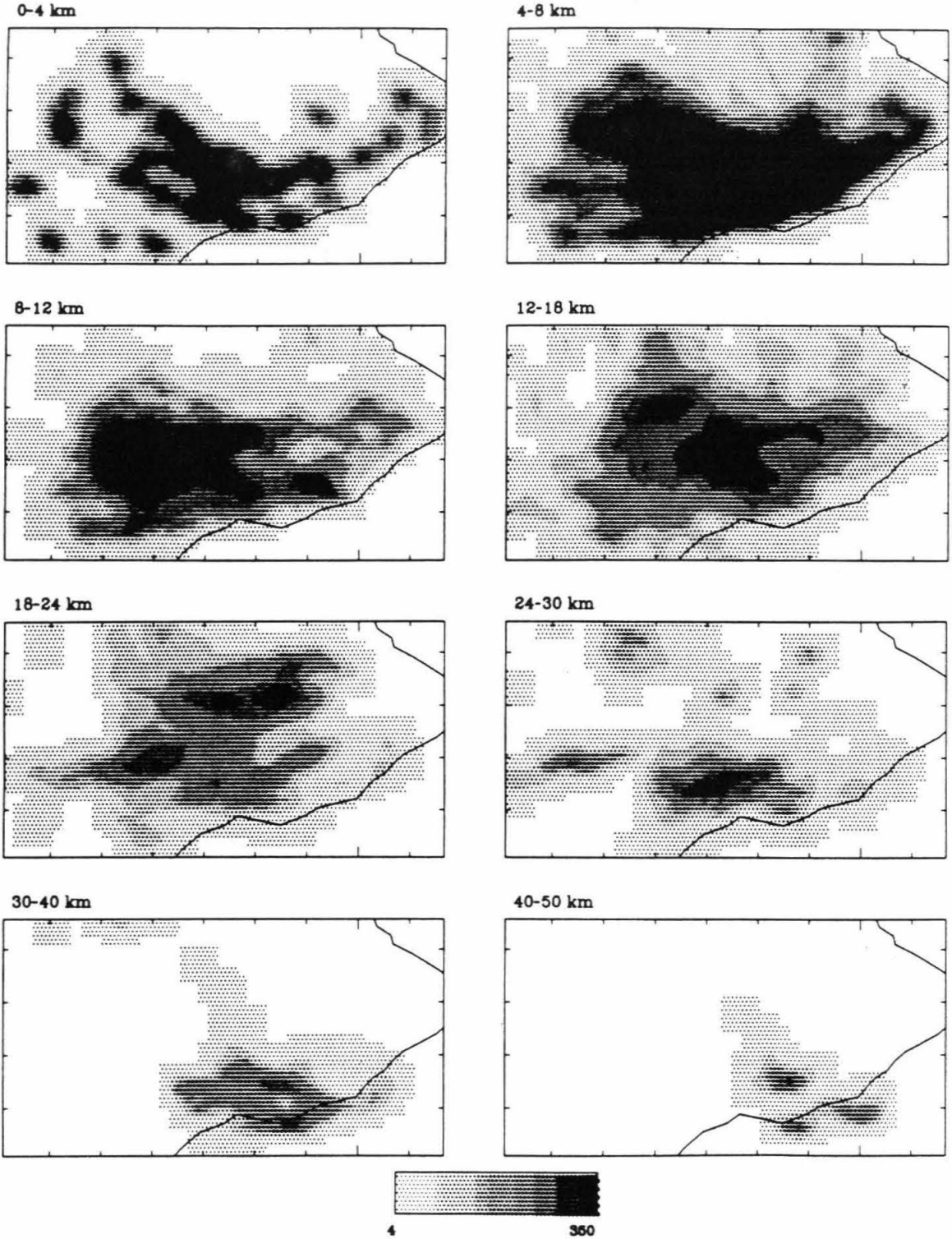


Figure 9d: Hitcount map of attenuation inversion. Only the shallow depth slices above 12 km are well covered by rays.

in Figures 10a and c for correlation lengths of 4 and 8 km, respectively. Figures 10b and d are the *a posteriori* error of the no-block inversion compared to the hitcount in the corresponding depth ranges for correlation lengths of 4 and 8 km, respectively. In general, the resolved anomalies explain the data fairly well, and errors are smaller than the amplitude of resolved anomalies in both the cases with $L = 4$ and 8 km. The case with $L = 4$ km has larger error relative to the anomalies, and this is an expected trade-off between the resolution and error.

Figures 11a, b, c and d show the resolution of the inversion for target points at (a) the East Rift Zone at a depth of 5 km, (b) the hypothesized Kilauea magma chamber at a depth of 7 km, (c) the hypothesized Mauna Loa magma chamber, and (d) the anomaly imaged west of Puu Kou at a depth of 8 km in this study. The target point is considered well-resolved if the image is localized near the target point. Both points (a) and (b) are fairly well resolved, with little east-west spreading. Point (c) is not expected to be well resolved because of the limited ray coverage in the Mauna Loa caldera area. Indeed, the maximum point is shifted to a shallower depth with less error (Figure 10b), but the overall geometry is not near the target point. Hence, we do not believe that the Mauna Loa magma chamber is well resolved. There is a trade-off between the depth extent of this anomaly and the error in the inversion. Figure 11d shows the resolution for a target point at the anomaly west of Puu Kou. The hitcount map (Figure 9d) shows that the anomaly is located at the edge of an area of good ray coverage, and we expect fairly good resolution at this location. Figure 11d supports the above observation: the

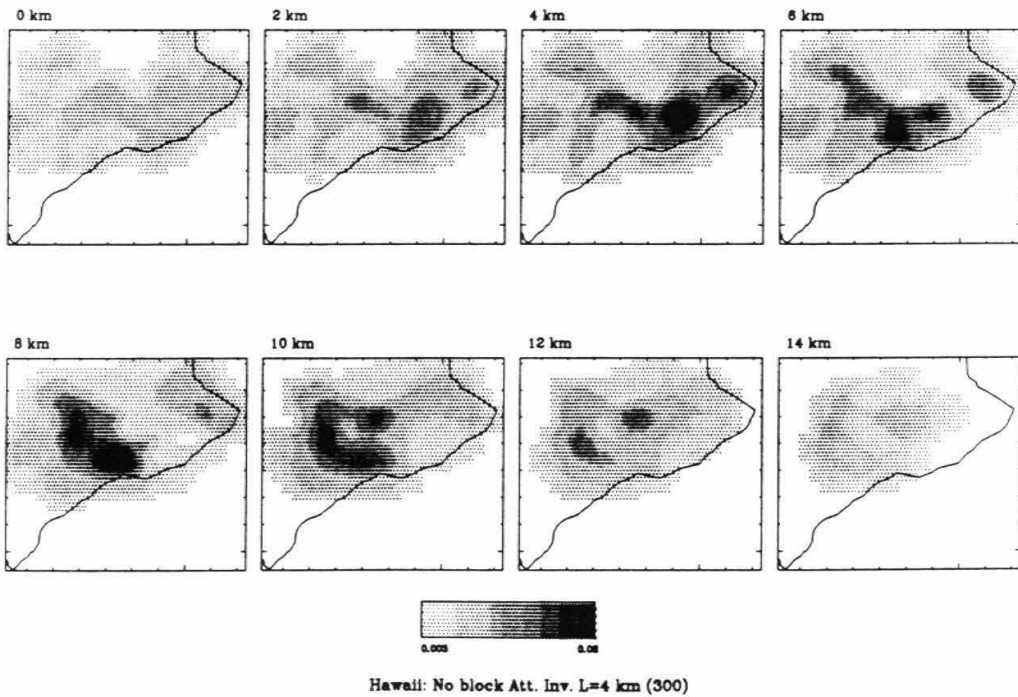
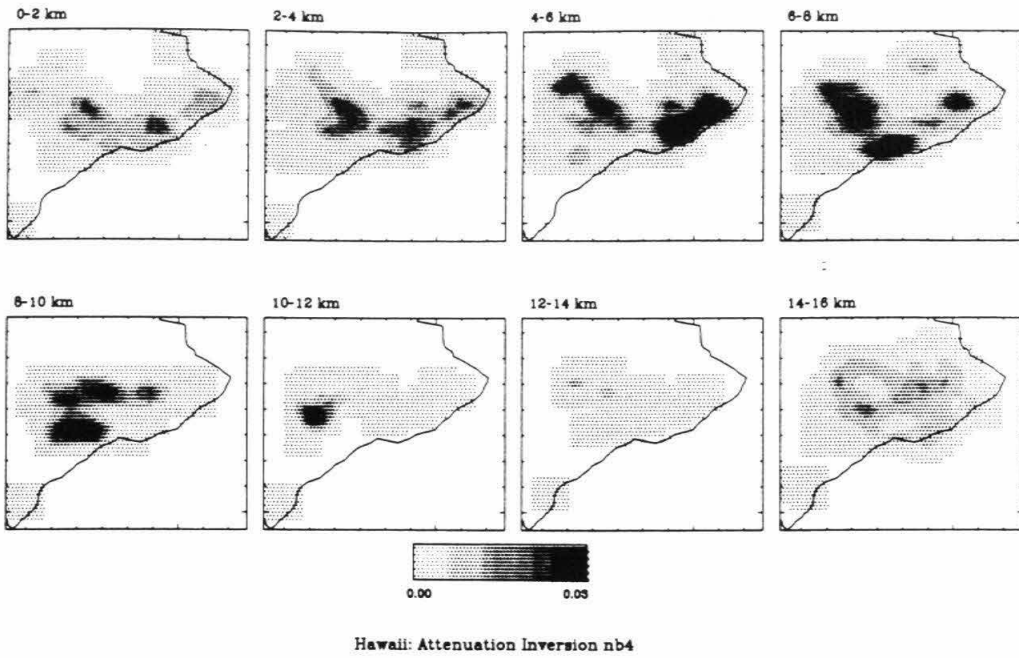
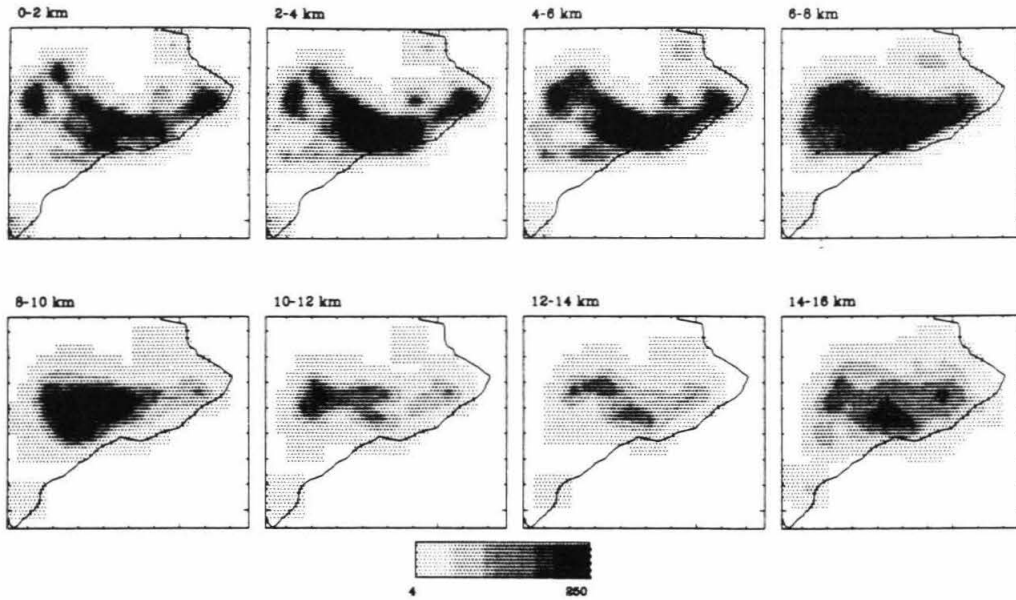
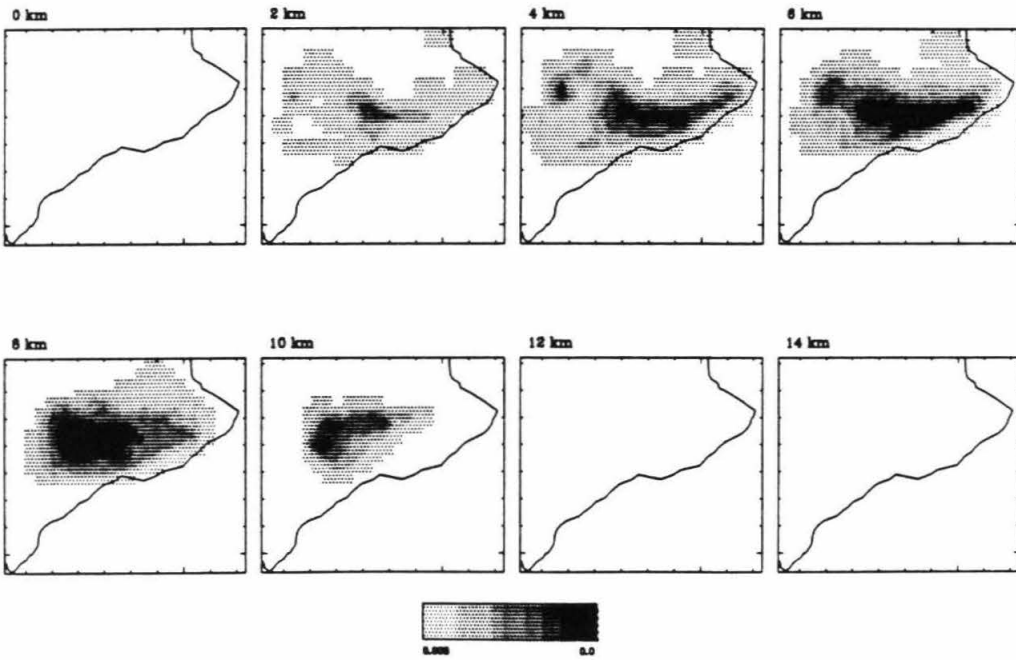


Figure 10a: Comparison between back-projection inversion and no-block generalized inversion on a smaller data set of 26 events. The top panel shows results from back-projection inversion with block sizes of 4 km x 4 km x 1 km, plotted in depth slices of 2 km thick. Bottom panel shows results from no-block inversion at depth intervals of 2 km. Results from these two different methods are very similar. Correlation length used in the no-block inversion is 4 km.



Hawaii: Attenuation Hitcount nb4



Hawaii: Error on No-Block Inv. L=4 km (300)

Figure 10b: Comparison between hitcount map of the back-projection attenuation inversion and the error of the inversion using the no-block inversion method. In general, anomalies imaged in Figure 10a are located in areas where errors are relatively small, indicating that the anomalies are well resolved.

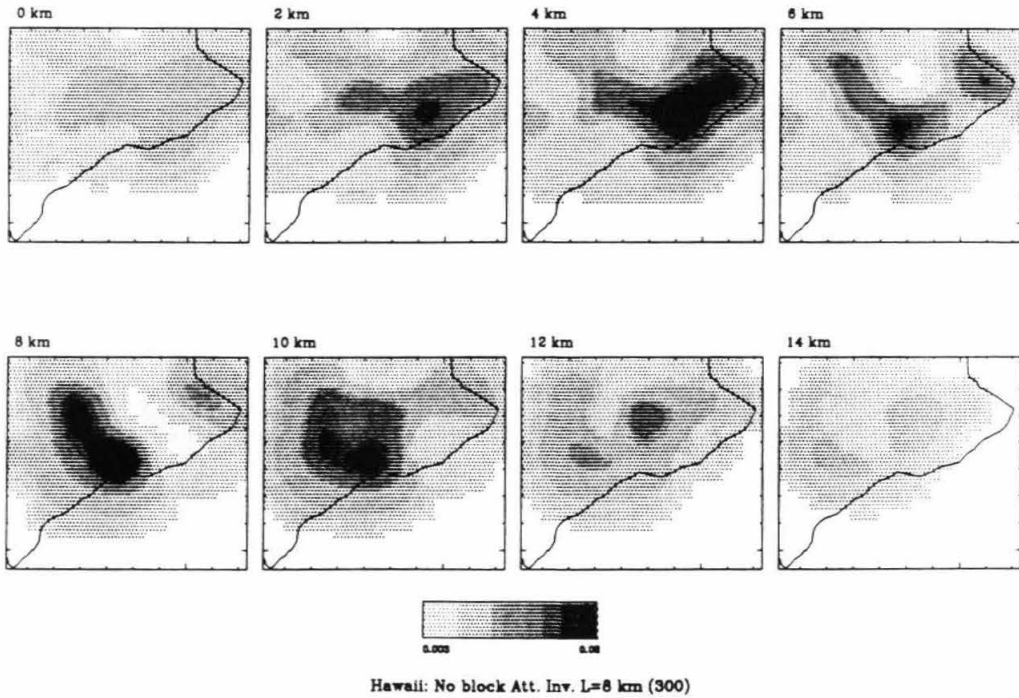
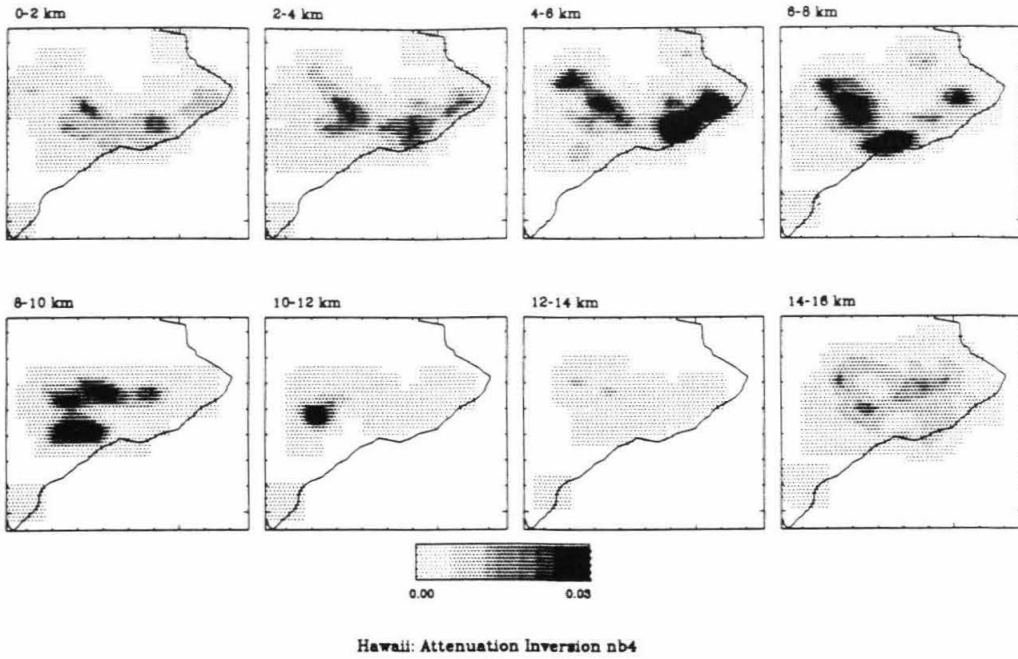


Figure 10c: Comparison between back-projection inversion and no-block generalized inversion on a smaller data set of 26 events. Bottom panel shows results from no-block inversion at depth intervals of 2 km with a correlation length of 8 km. Because of this larger correlation length, anomalies imaged are more extensive spatially than in Figure 10a.

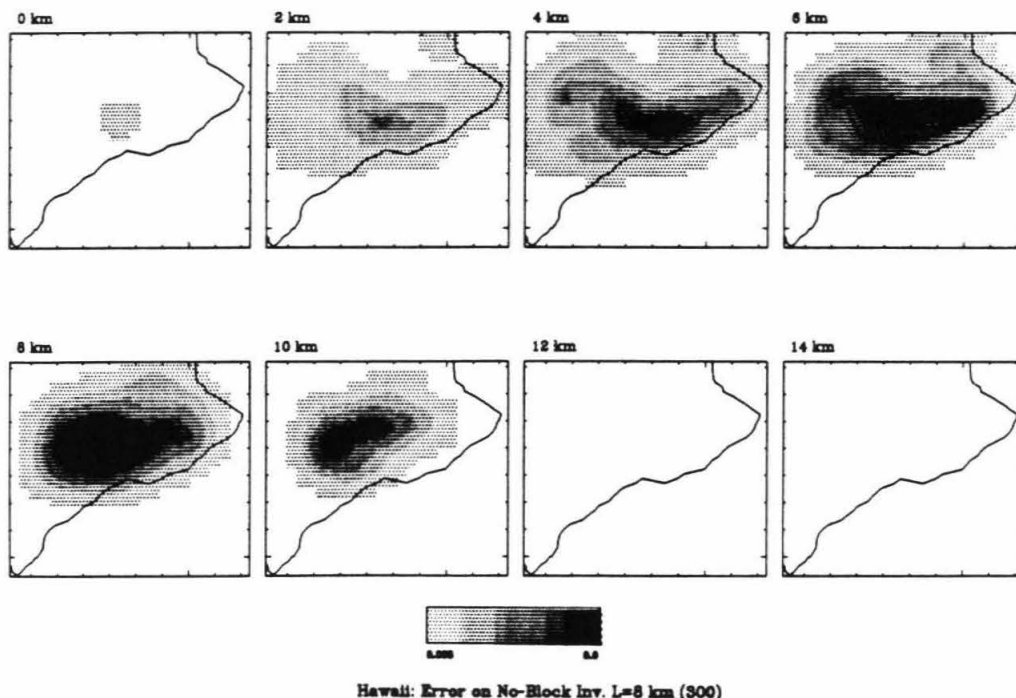
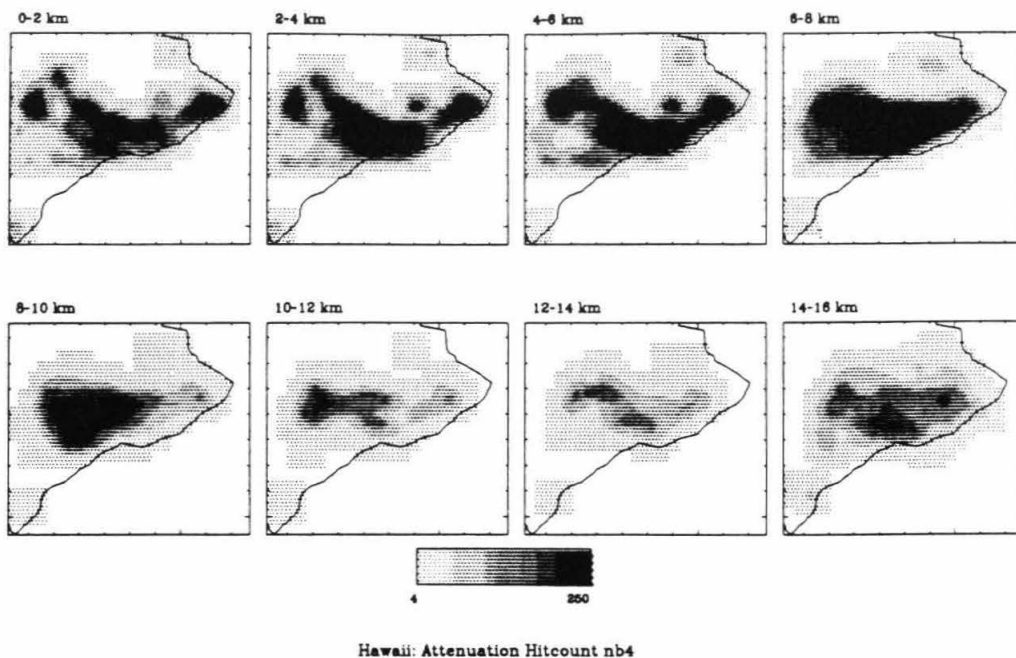


Figure 10d: Comparison between hitcount map of the back-projection attenuation inversion and the error of the inversion using the no-block inversion method. Errors of the inversion for this correlation length are smaller than those for a correlation length of 4 km. Once again, anomalies imaged in Figure 10c are located in areas where errors are small, indicating that the anomalies are well resolved.

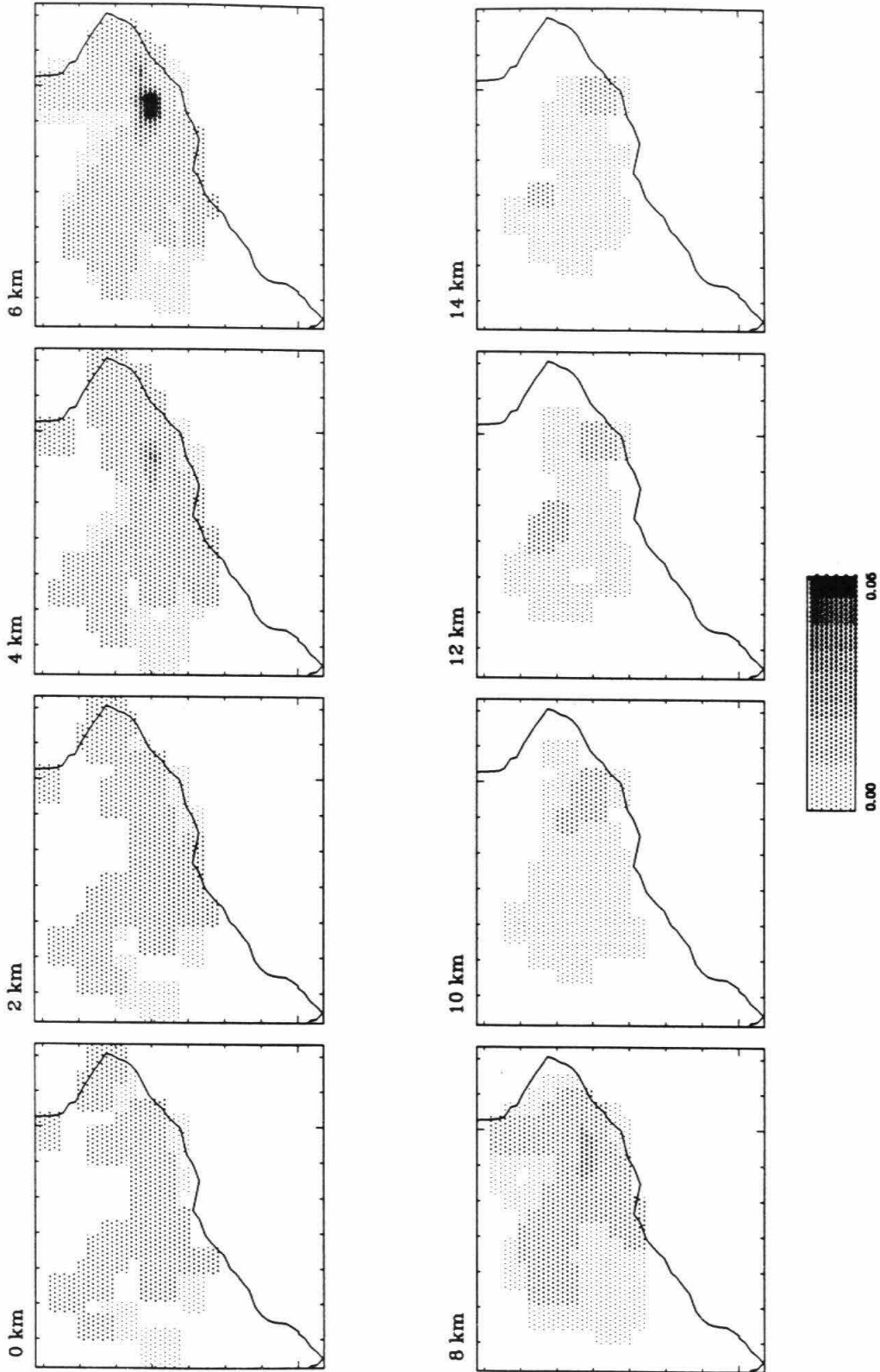


Figure 11a: Resolution test using the no-block inversion method with correlation length of 2 km. The target point is located along the ERZ at a depth of 5 km. The results are very 'pointlike' which means that the anomaly imaged at this location is very well resolved spatially.

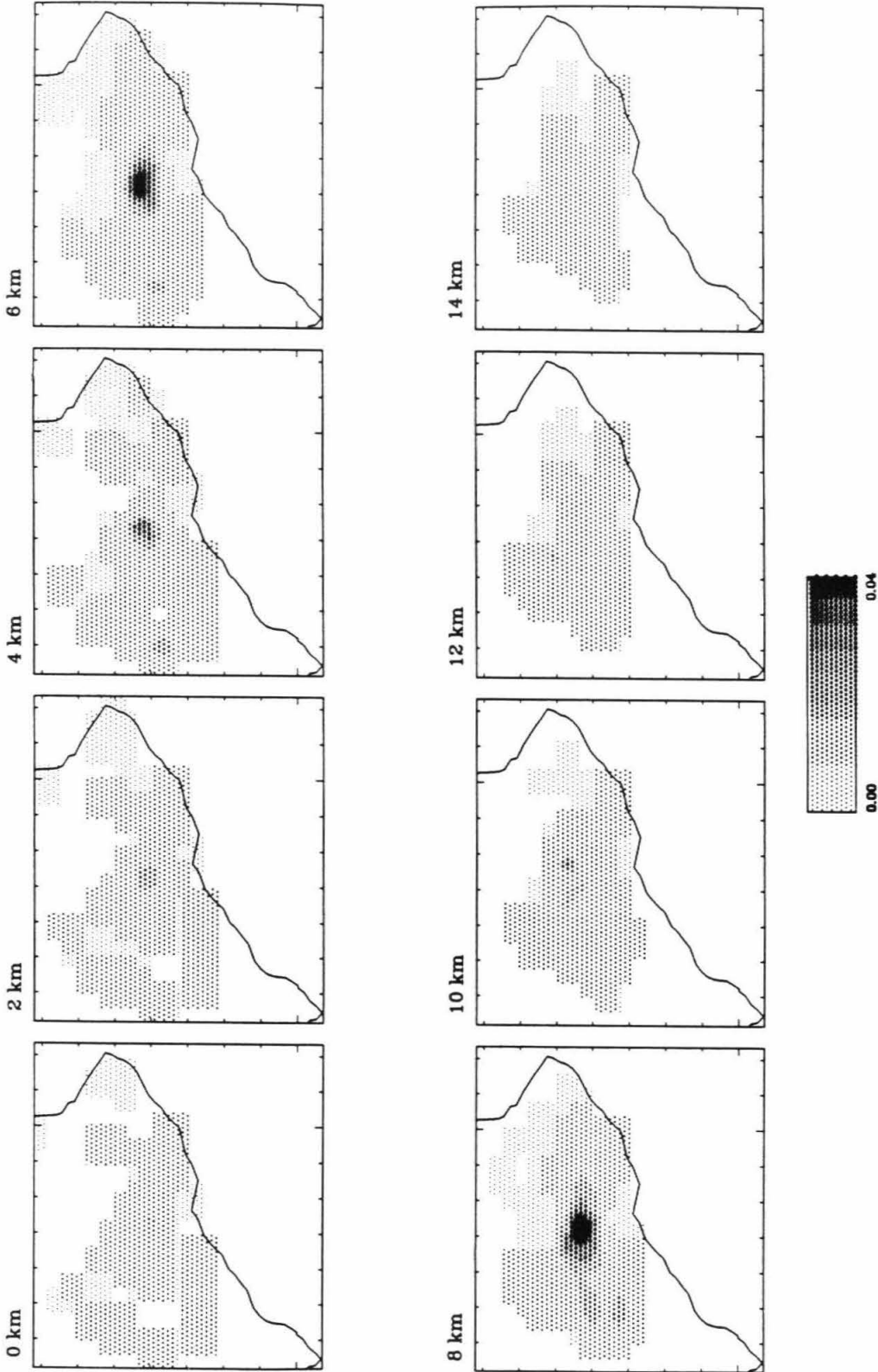


Figure 11b: Resolution test with the target point at Kilauea magma chamber at a depth of 7 km. There is some minor east-west 'spreading'; the depth resolution is better than in Figure 12a because we can see the maximum point between 6 and 8 km depth in this case, while the maximum point is located closer to a depth of 6 km in Figure 11a. The magma chamber imaged in this study should then be well resolved.

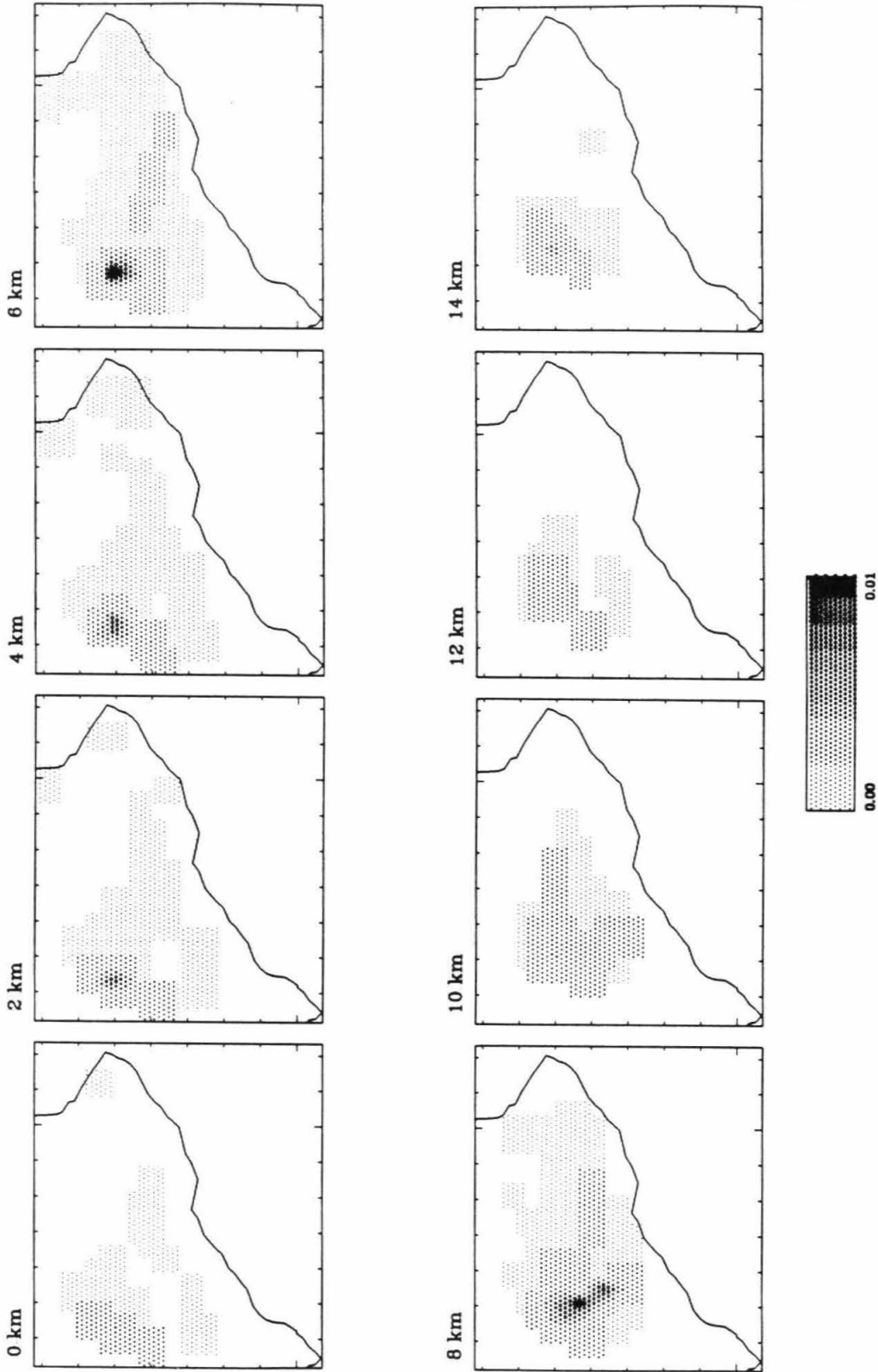


Figure 11c: Resolution test with the target point at Mauna Loa magma chamber at a depth of 8 km. The maximum value is more spread out in this case and is actually placed at a depth of 6 km where the error is less than at a depth of 8 km, indicating the limited resolution of the Mauna Loa magma chamber with the data set we used.

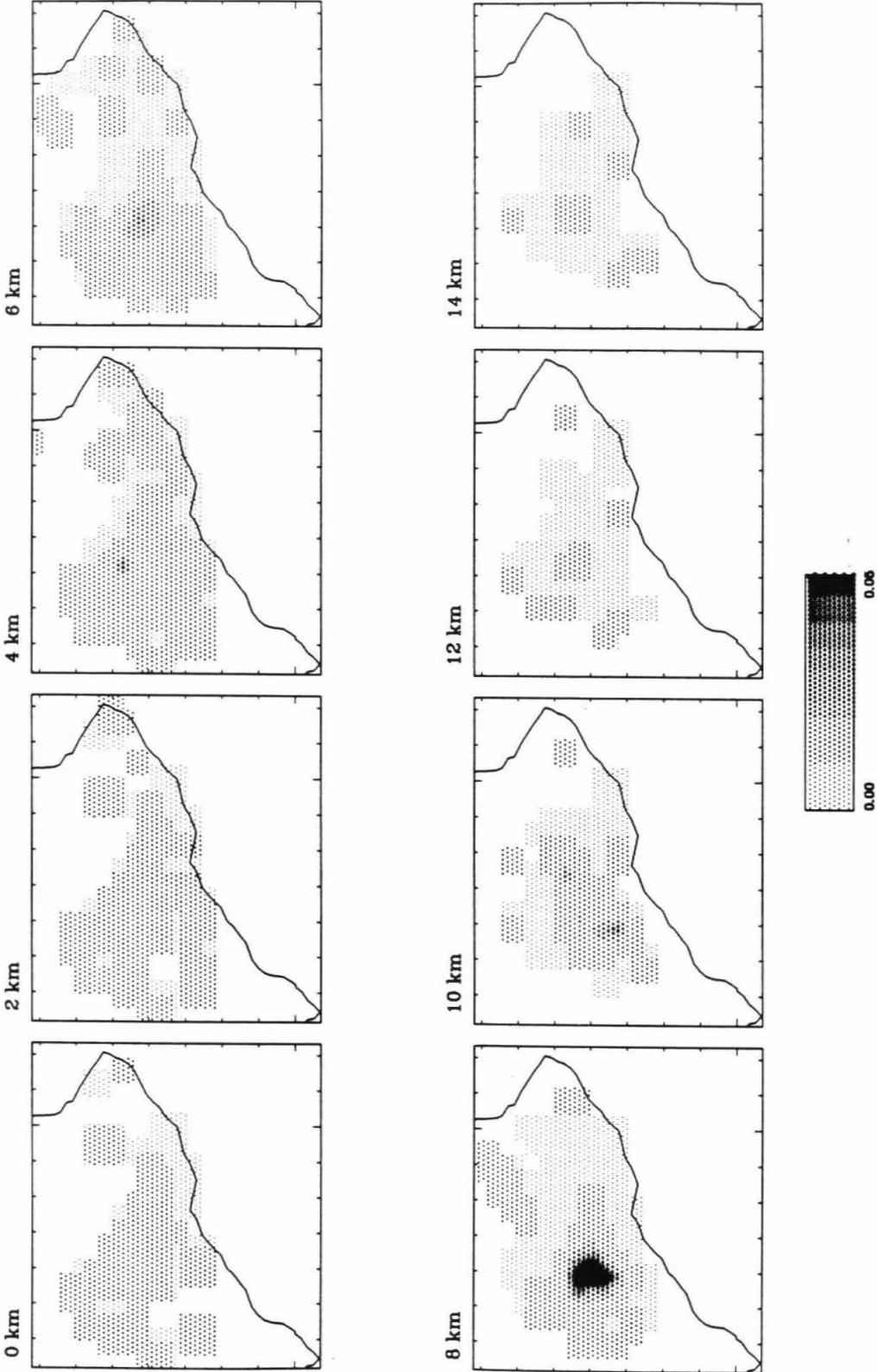


Figure 11d: Resolution test with the target point at the unknown attenuation anomaly west of Puu Kou at a depth of 8 km. The maximum value is well located at the target point, but the shape is less than a 'pointlike' function, indicating some trade-off that is due to less ray coverage. The depth of the maximum is well resolved.

maximum value is located at the target point at the correct depth, with little spreading in the depth direction. However, the shape of the anomaly is not a 'pointlike' function, which means that there is a probable trade-off between the spatial resolution and error. In general, we believe that the anomaly imaged at this location is not an artifact of ray coverage but is well resolved.

3.6 Discussion

The inversion results obtained for the KERZ sub-quadrangle clearly delineate the East Rift Zone to a depth of about 6 km (Figure 8a). The East Rift Zone dike complex is inferred to have a trapezoidal shape in cross section perpendicular to the rift zone, with a widened bottom extending to a depth of about 10 km (Hill and Zucca, 1987). Magma is considered to intrude into the dike complex from a depth of 10 km. Ryan *et al.* (1981) hold a different view, that intrusive magma flows along narrow pipelines at a depth of about 3-4 km and that intrusion of magma mainly involves movements along horizontal pipelines. Results from this study indicate that intrusive magma can probably be traced to a depth of about 4-6 km.

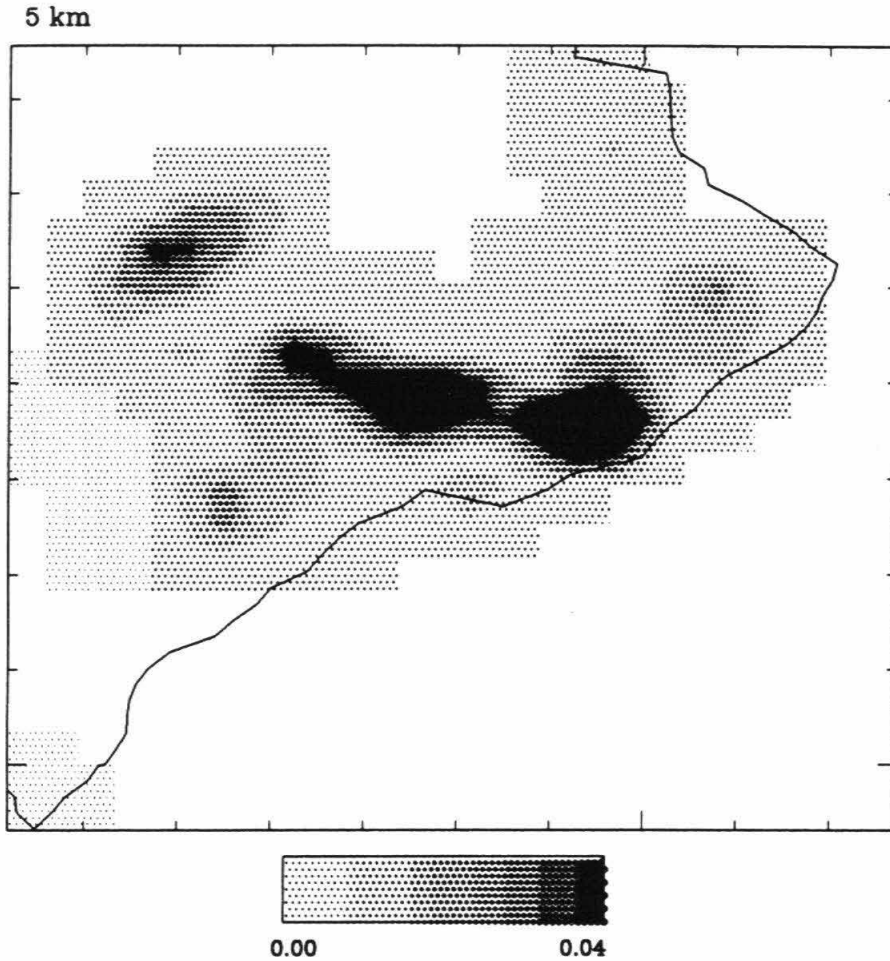
We also notice that there are distinct sites of attenuating anomalies along the rift zone, suggesting some magma pooling along the rift zone. Some of them coincide with the proposed sites of magma reservoirs, for example, Mauna Ulu and Puu Oo (Dzurisin *et al.*, 1984).

The Kilauea magma chamber is imaged at a depth of about 4-8 km. The image of this shallow magma chamber is not very clear, but if we examine the results from no-block inversion (Figure 10a), we see that at a 6 km depth, the

shallow chamber is imaged very clearly. Since the hypothesized magma chamber has a radius of about 2 km (Koyanagi *et al.*, 1975), averaging the anomaly over a large depth will tend to reduce the amplitude of the anomaly. The inversion results for the 5-6 km depth range show the image of the shallow chamber at the hypothesized location, south of Halemaumau (Figure 12). The location of this magma chamber agrees very well with the center of inflation as reported by Fiske and Kinoshita (1969) and by Dvorak *et al.*, (1983).

The data set we selected, unfortunately, does not cover the area between Mauna Loa and Kilauea densely enough to obtain good resolution in this area. Nevertheless Figure 7a shows a fairly clear anomaly at the hypothesized Mauna Loa magma chamber at a depth of 4-8 and 8-12 km. This suggests that the Mauna Loa chamber is larger and deeper than the Kilauea chamber, which is consistent with other geophysical studies (Decker *et al.*, 1983 and Koyanagi *et al.*, 1976). Resolution test done at this location shows that the Mauna Loa chamber image could be smeared out in depth. More ray coverage is needed to resolve this larger magma chamber effectively.

There is an apparent link between the Kilauea and the Mauna Loa magma chambers at a shallow depth, about 4-6 km. The image of this anomaly is more apparent in Figure 10a. The East Rift Zone anomaly dominates at the shallow 4-6 km depth and is connected to the Kilauea chamber at about 6 km, which also connects farther west and deeper at about 6-8 km to the Mauna Loa chamber. The pattern of seismicity and ground deformation associated with magma intrusion and eruptions do not support a shallow (<



Hawaii: Attenuation Inversion nb4

Figure 12: Attenuation inversion result with block size of 4 km x 4 km x 1 km at a depth of 5-6 km. The magma chamber under Kilauea is very clearly imaged in this figure. The size of the chamber is likely to be small, so when results are averaged over several layers, each 1 km thick, the anomaly is less intense, as is the case in Figures 10a and c.

10 km deep) connection between the summit reservoirs of Mauna Loa and Kilauea. There are no swarms of earthquakes with tremor in the Kaoiki region between Mauna Loa and Kilauea associated with the typical tilt changes at the summit that repeatedly characterize summit-to-rift type intrusions. Alternatively, the high seismicity in the Kaoiki region may be attributed to a tectonic response to lateral stresses induced by the growth of the two active volcanoes (as inferred by Koyanagi *et al.*, 1976). It may be a region of secondary melting that perhaps does not actively participate in intrusive activity. The south flank of Kilauea may also be a tectonic feature, responding to lateral stresses induced by magma intrusions along the East Rift Zone. Hence, this anomaly could be an image of an area of secondary melting in the Kaoiki region.

It is interesting to note that the Hilina fault zone is also delineated by attenuating anomalies. It is most likely that the highly fractured material in the fault zone attenuates seismic waves.

The Southwest Rift Zone, however, is not imaged as an attenuating region, except at a depth of 8-12 km, where an attenuating anomaly is imaged west of the Puu Kou. The resolution test done at this location indicates that the anomaly is well resolved spatially and is not an artifact of poor ray coverage. There is slight horizontal smearing but the geometry is still well resolved. The nature of this anomaly is not clear; seismicity at this location is not very high, but areas north and east of this anomaly have high seismicity. There is an overlap between this anomaly and the termination of the seismicity along the Southwest Rift Zone. Because of this termination of rift seismicity and

spreading of earthquakes into the south flank, this location has been thought of as a possible site of secondary magma storage (Koyanagi, R., personal communications). The Southwest Rift Zone is not as active in terms of magma eruptions and seismicity as the East Rift Zone at the present time. Hence it is not surprising that no clear continuous trend of attenuating anomalies outlines the rift zone as it does along the East Rift Zone.

3.7 Conclusions

In this chapter, we inverted S -to- P wave amplitude ratios for a three-dimensional attenuation structure beneath Kilauea and Mauna Loa using a simple velocity model. The results are consistent with other geophysical observations.

Resolution of the inversion for the area covering Mauna Loa is not as good as that covering Kilauea and the East Rift Zone. Anomalies imaged under Mauna Loa are, nevertheless, consistent with the hypothesized location of the magma chamber. The magma chamber is located at about 4-6 km for Kilauea and 6-10 km for Mauna Loa, though it is less well resolved for Mauna Loa because of less dense ray coverage. The East Rift Zone is characterized by an attenuating structure down to a depth of 6 km. Secondary sites of magma reservoirs are imaged at Mauna Ulu and Puu Oo, sites of current eruptions. The Southwest Rift Zone does not exhibit high attenuation except at Puu Kou, where an attenuating anomaly is imaged west of the site. The nature of this anomaly is not clear. A continuous trend of attenuating anomaly is found between Mauna Loa and Kilauea at a depth of about 8-10

km.

Because of the lack of accurate calibration on the horizontal component stations, we have utilized only the vertical component data in this study. With more accurate calibration on all horizontal component stations, we hope to utilize fully all three components data to obtain the attenuation structure of the island of Hawaii.

Because of the very simplified structure used, and the relatively sparse station distribution, the results of this study should be considered preliminary. With better velocity models from results of local travel-time tomography studies in progress (Rowan and Clayton, 1988), we hope to better determine the focal mechanisms and the ray paths in a three-dimensional medium. This will help to remove some of the uncertainties involved in the attenuation tomography, a technique that may be applied with increasing effectiveness with additional instrumental coverage and structural understanding. Finally, more local studies are necessary to sharpen the focus on some of the major volcanological problems for Hawaii, such as the Kilauea summit resolution, or the more detailed aspects of the East Rift Zone magma storage.

References to Part I

- Aki, K. and W.H.K. Lee, 1976. Determination of three-dimensional velocity anomalies under a seismic array, using first P arrival times from local earthquakes, 1. A homogeneous initial model, *J. Geophys. Res.*, **81**, 4381-4399.
- Aki, K. and R.Y. Koyanagi, 1981. Deep volcanic tremor and magma ascent mechanism under Kilauea, Hawaii, *J. Geophys. Res.*, **86**, 7095-7109.
- Anderson, D.L. and C.B. Archambeau, 1964. The anelasticity of the Earth, *J. Geophys. Res.*, **69**, 2071-2084.
- Anderson, D.L., 1967. The anelasticity of the mantle, *Geophys. J. R. astr. Soc.*, **14**, 135-164.
- Aramaki, S. and J.G. Moore, 1969. Chemical composition of prehistoric lavas at Makaopuhi crater, Kilauea volcano, and periodic change in alkali content of Hawaiian tholeiitic lavas, *Bull. Earthquake Res. Inst. Tokyo Univ.*, **47**, 257-270.
- Backus, G. and F. Gilbert, 1968. The resolving power of gross earth data, *Geophys. J.R. astr. Soc.*, **16**, 169-205.
- Backus, G. and F. Gilbert, 1970. Uniqueness in the inversion of inaccurate gross earth data, *Phil. Trans. R. Soc. London*, **266**, 123-192.
- Broyles, M.L., W. Suyenaga and A.S. Furumoto, 1979. Structure of the lower east rift zone of Kilauea volcano, Hawaii, from seismic and gravity data, *J. Volcanol. Geother. Res.*, **5**, 317-336.
- Chou, W.C. and R.J. Booker, 1979. A Backus-Gilbert approach to inversion of travel-time data for three-dimensional velocity structure, *Geophys. J.R. astr. Soc.*, **59**, 325-344.
- Clayton, R.W. and R.P. Comer, 1987. Reconstruction of mantle heterogeneity by iterative back-projection of travel times: 2. Results for P waves, *submitted for publication*.
- Comer, R.P. and R.W. Clayton, 1987. Reconstruction of mantle heterogeneity by iterative back-projection of travel times: 1. Theory and Reliability, *submitted for publication*.
- Crosson, R.S. and E.T. Endo, 1981. Focal mechanisms of earthquakes related to the 29 November, 1975 Kalapana earthquake: The effect of structure models, *Bull. Seismol. Soc. Am.*, **71**, 713-729.
- Decker, R.W., R.Y. Koyanagi, J.J. Dvorak, J.P. Lockwood, A.T. Okamura, K.M. Yamashita and W.R. Tanigawa, 1983. Seismicity and surface deformation of Mauna Loa Volcano, Hawaii, *EOS Trans. AGU*, **64**, 545-547.
- Dines, K.A. and R.J. Lytle, 1979. Computerized geophysical tomography, *Proc. IEEE*, **67**, 1065-1073, 1979.
- Doser, D.I. and H. Kanamori, 1986. Depth of seismicity in the Imperial Valley region (1977-1983) and its relationship to heatflow, crustal structure, and the October 15, 1979 earthquake, *J. Geophys. Res.*, **91**, 675-688.

- Dvorak, J., A. Okomura and J.H. Deiterich, 1983. Analysis of surface deformation data, Kilauea Volcano, Hawaii, October 1966 to September 1970, *J. Geophys. Res.*, **88**, 9295-9304.
- Dzurisin, D., L.A. Anderson, G.P. Eaton, R.Y. Koyanagi, P.W. Lipman, J.P. Lockwood, R.T. Okamura, G.S. Puniwai, M.K. Sako and K.M. Yamashita, 1980. Geophysical observations of Kilauea Volcano, Hawaii, 2. Constraints on the magma supply during November 1975-September 1977, *J. Volcanol. Geother. Res.*, **7**, 241-269.
- Dzurisin, D., R.Y. Koyanagi and T.T. English, 1984. Magma supply and storage at Kilauea Volcano, Hawaii, 1956-1983, *J. Volcanol. Geotherm.*, **21**, 177-206.
- Eaton, J.P., 1962. Crustal structure and volcanism in Hawaii, in *The Crust of the Pacific Basin, Geophys. Monogr. Ser.*, **6**, 13-29.
- Ellsworth, W.L. and R.Y. Koyanagi, 1977. Three-Dimensional Crust and Mantle Structure of Kilauea Volcano, Hawaii, *J. Geophys. Res.*, **82**, 5379-5394.
- Fawcett, J.A. and R.W. Clayton, 1984. Tomographic reconstruction of velocity anomalies, *Bull. Seismol. Soc. Am.*, **74**, 2201-2219.
- Fiske, R.S. and W.T. Kinoshita, 1969. Inflation of Kilauea Volcano prior to its 1967-1968 eruption, *Science*, **165**, 341-349.
- Fornari, D.J., 1987. The geomorphic and structural development of Hawaiian submarine rift zones, *U.S. Geol. Surv. Prof. Paper*, **1350**, 125-132.
- Frankel, A., 1982. The effects of attenuation and site response on the spectra of microearthquakes in the Northeastern Caribbean, *Bull. Seismol. Soc. Am.*, **72**, 1379-1402.
- Franklin, J.N., 1970. Well-posed stochastic extensions of ill-posed linear problems, *J. Math. Anal. Appl.*, **31**, 682-716.
- Fuis, G.S., W.D. Mooney, J.H. Healy, G.A. McMechan and W.J. Lutter, 1982. Crustal structure of the Imperial Valley region in the Imperial Valley, California earthquake of Oct. 15, 1979, *U.S. Geol. Survey Prof. Paper*, **1254**, 25-49.
- Hearn, T.M. and R.W. Clayton, 1986a. Lateral velocity variations in southern California: 1. Results for the upper crust from Pg-waves, *Bull. Seismol. Soc. Am.*, **76**, 511-520.
- Hearn, T.M. and R.W. Clayton, 1986b. Lateral velocity variations in southern California: 2. Results for the lower crust from Pn-waves, *Bull. Seismol. Soc. Am.*, **76**, 495-509.
- Hill, D.P., 1977. A model for earthquake swarms, *J. Geophys. Res.*, **82**, 1347-1352.
- Hill, D.P. and J.J. Zucca, 1987. Geophysical constraints on the structure of Kilauea and Mauna Loa Volcanoes and some implications for seismomagmatic processes, *U.S. Geol. Surv. Prof. Paper*, **1350**, 903-918.
- Humphreys, E.D., R.W. Clayton and B.H. Hager, 1984. A tomographic image of mantle structure beneath southern California, *Geophys. Res. Lett.*, **11**, 625-627.
- Jachens, R.C. and G.P. Eaton, 1980. Geophysical observations of Kilauea Volcano, Hawaii, 1. Temporal gravity variations related to the 29 November, 1975, M=7.2

- earthquake and associated summit collapse, *J. Volcanol. Geother. Res.*, **7**, 225-240.
- Jackson, D.D., 1979. The use of *a priori* data to resolve non-uniqueness in linear inversion, *Geophys. J.R. astr. Soc.*, **57**, 137-157.
- Klein, F.W., 1981. A linear gradient crustal model for south Hawaii, *Bull. Seismol. Soc. Am.*, **71**, 1503-1510.
- Klein, F.W. and R.Y. Koyanagi, 1986. The seismicity and tectonics of Hawaii, in *The Eastern Pacific Ocean and Hawaii volume of the Decade of North American Geology series (preprint)*.
- Klein, F.W., R.Y. Koyanagi, J.S. Nakata and W.R. Tanigawa, 1987. The seismicity of Kilauea's magma system, *U.S. Geol. Surv. Prof. Paper*, **1350**, 1019-1186.
- Kobayashi, A., I. Furuya and K. Uhira, 1986. Re-examination of magma reservoirs by spectral analysis of P and S waves, *Geophys. Magazine*, **41**, 173-187.
- Koyanagi, R.Y., E.T. Endo and J.S. Ebusu, 1975. Reawakening of Mauna Loa Volcano, Hawaii: A preliminary evaluation of seismic evidence, *Geophys. Res. Letter*, **2**, 405-408.
- Koyanagi, R.Y., E.T. Endo and P.L. Ward, 1976. Seismic activity on the island of Hawaii, 1970-1973, in *The geophysics of the Pacific Ocean Basin and its margin*, *Geophys. Monogr.*, **19**, 169-173.
- Lee, W.H.K. and J.C. Lahr, 1975. HYPO71(revised): a computer program for determining hypocenter, magnitude and first-motion patterns of local earthquakes, *U.S. Geol. Surv. Open File Rept.*, 75-311.
- Liu, H.L., 1983. Interpretation of near-source ground motion and implications, Ph.D. thesis, California Institute of Technology, 184pp..
- Mogi, K., 1958. Relationship between the eruptions of various volcanoes and the deformations of the ground surfaces around them, *Bull. Earthquake Res. Inst. Tokyo Univ.*, **36**, 99-134.
- Nercessian, A., A. Hirn and A. Tarantola, 1984. Three-dimensional seismic transmission prospecting of the Mont Dore volcano, France, *Geophys. J.R. astr. Soc.*, **76**, 307-315.
- Powers, H.A., 1955. Composition and origin of basaltic magma of the Hawaiian Islands, *Geochim. et Cosmochim. Acta.*, **7**, 77-107.
- Rautian, T.G., V.I. Khalturin, V.G. Martynov and P. Molnar, 1978. Preliminary analysis of the spectral content of P and S waves from local earthquakes in the Garm, Tadjikistan region, *Bull. Seismol. Soc. Am.*, **68**, 949-971.
- Rowan, L. and R.W. Clayton, 1988. Local travel-time tomographic study of Kilauea volcano, *Seismol. Res. Lett.*, **59**, 30.
- Ryan, M.P., R.Y. Koyanagi and R.S. Fiske, 1981. Modelling the three-dimensional structure of macroscopic magma transport system: application to Kilauea Volcano, Hawaii, *J. Geophys. Res.*, **86**, 7111-7129.
- Sanders, C.O., 1984. Location and configuration of magma bodies beneath Long Valley, California determined from anomalous earthquake signals, *J. Geophys. Res.*,

- 89**, 8287-8392.
- Sanders, C.O., P. Ho-Liu, D. Rinn and H. Kanamori, 1988. Anomalous shear-wave attenuation in the shallow crust beneath the Coso volcanic region, California, *J. Geophys. Res.*, **93**, 3321-3338.
- Sudo, Y., 1987. Attenuation of seismic wave in the Aso Caldera, Kyushu, Japan, *Hawaii Symposium on How Volcanoes Work Abstract Volume*, 243.
- Tarantola, A. and A. Nercessian, 1984. Three-dimensional inversion without blocks, *Geophys. J.R. astr. Soc.*, **76**, 299-306.
- Tarantola, A. and B. Valette, 1982. Generalized nonlinear inverse problems solved using the least squares criterion, *Rev. Geophys. Space Phys.*, **20**, 219-232.
- Thurber, C.H., 1984. Seismic detection of the summit magma complex of Kilauea volcano, Hawaii, *Science*, **223**, 165-167.
- Thurber, C.H., 1987. Seismic structure and tectonics of Kilauea Volcano, *U.S. Geol. Surv. Prof. Paper*, **1350**, 919-934.
- Walck, M.C. and R.W. Clayton, 1988. P-wave velocity variations in the Coso region, California, derived from local earthquake travel times, *J. Geophys. Res.*, **92**, 393-406.
- Walck, M.C., 1988. Three-dimensional V_p/V_s variations for the Coso region, California, *J. Geophys. Res.*, **93**, 2047-2052.
- Walter, A.W. and C.S. Weaver, 1980. Seismicity of the Coso Range, California, *J. Geophys. Res.*, **85**, 2441-2458.
- Ward, R.W. and C.Y. Young, 1980. Mapping seismic attenuation within geothermal systems using teleseisms with application to the Geysers-Clear Lake region, *J. Geophys. Res.*, **85**, 5227-5236.
- Weaver, C.S. and D.P. Hill, 1978. Earthquake swarms and local crustal spreading along major strike-slip faults in California, *Pageoph.*, **117**, 51-64.
- Wiggins, R.A., 1972. The general inverse problem: implications of surface waves and free oscillations for earth structure, *Rev. Geophys. Space Phys.*, **10**, 251-285.
- Wong, J., P. Hurley and G.F. West, 1983. Crosshole seismology and seismic imaging in crystalline rocks, *Geophys. Res. Lett.*, **10**, 686-689.

Appendix

The best-fit fault plane solutions shown in this Appendix were obtained from first motion picks at HVO stations for the 63 events. Compressions are symbolized by filled circles and dilatations by open circles. The numbers on the top left corners are numbers of the events in the same order as listed in Tables 1a and b.

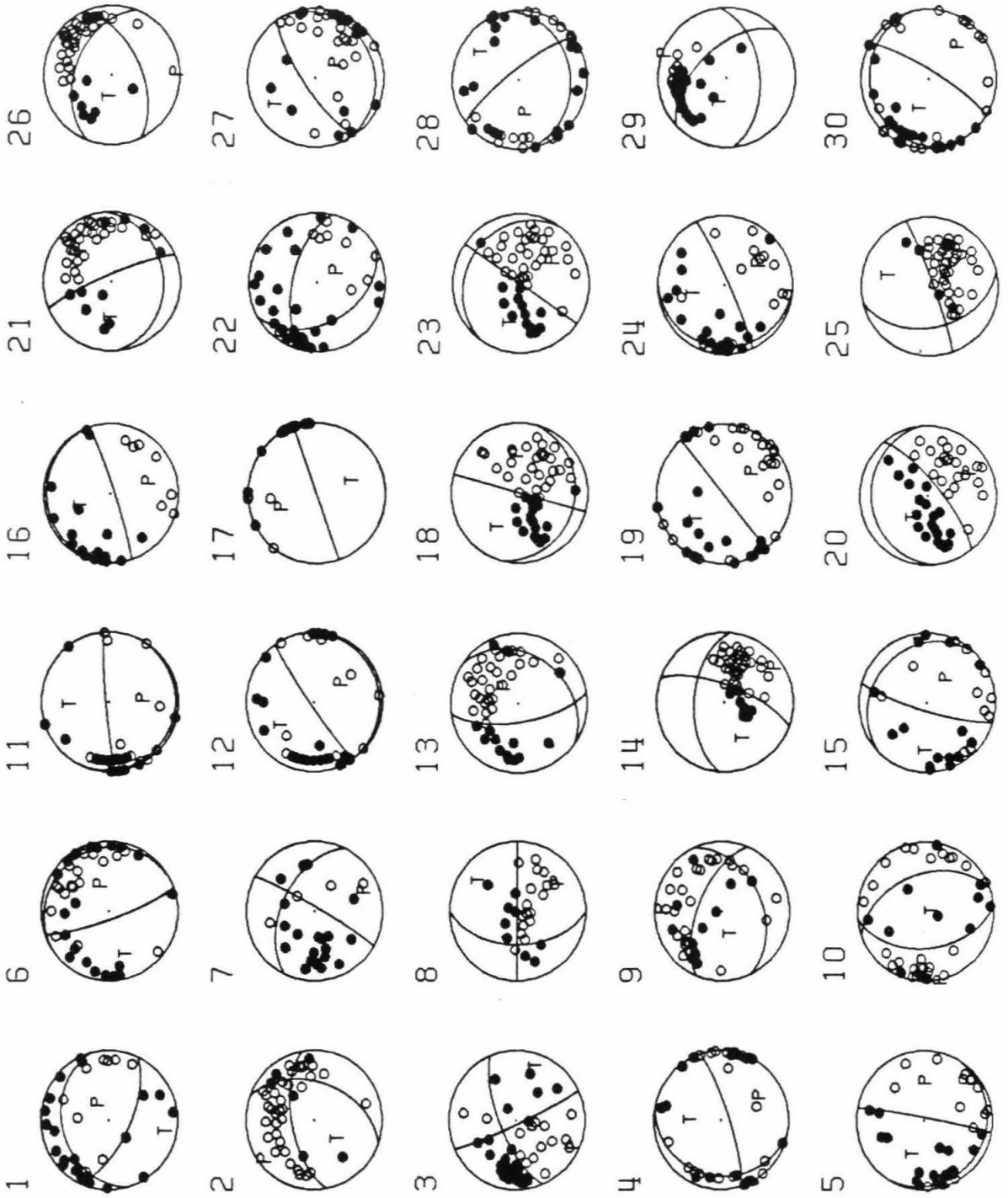


Figure A1

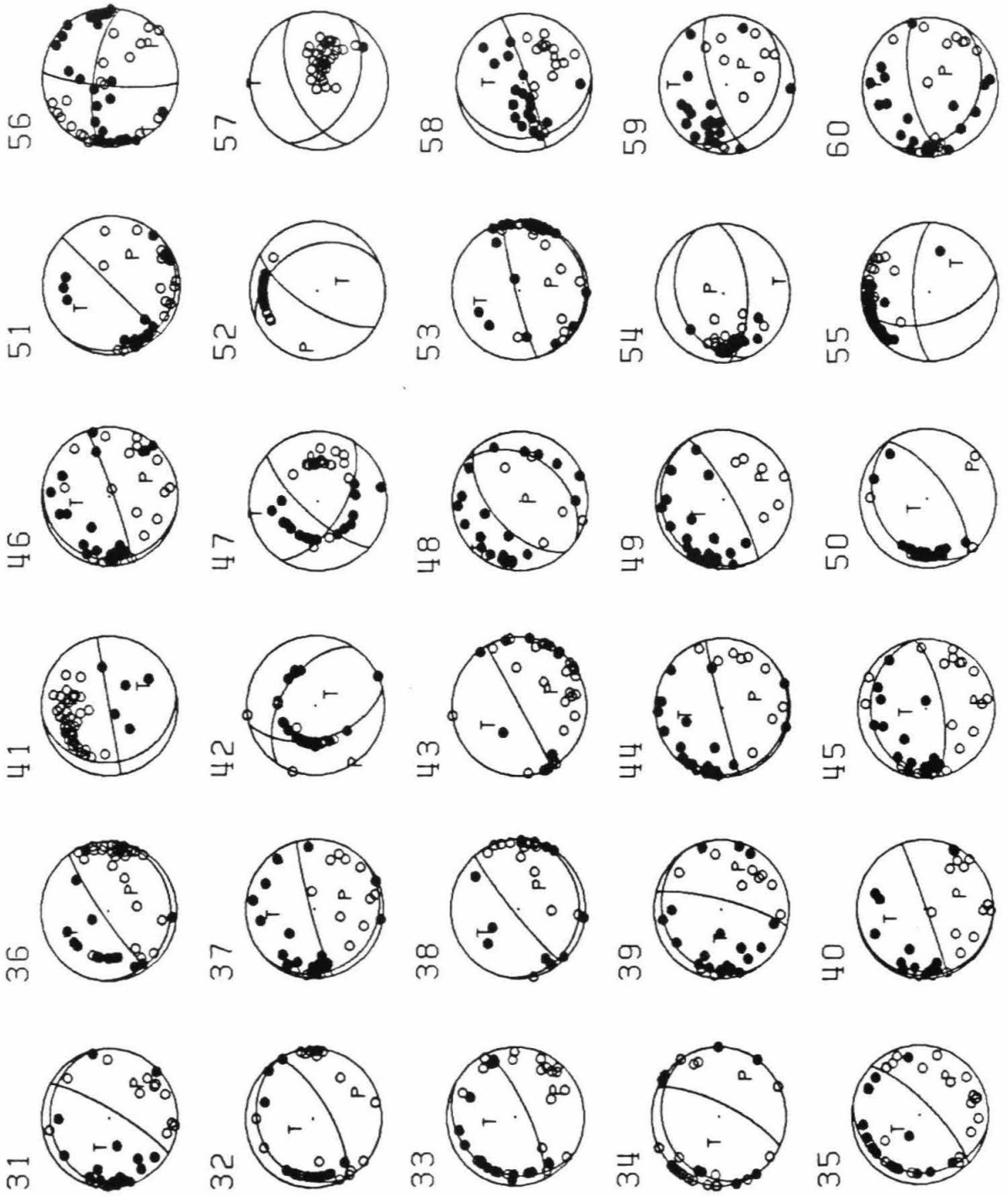


Figure A1 (cont.)



Figure A1 (cont.)

Abstract to Part II

Long period seismograms recorded at Pasadena of earthquakes occurring along a profile to Imperial Valley are studied in terms of source phenomena (e.g., source mechanisms and depths) versus path effects. Some of the events have known source parameters, determined by teleseismic or near-field studies, and are used as master events in a forward modeling exercise to derive the Green's functions (SH displacements at Pasadena that are due to a pure strike-slip or dip-slip mechanism) that describe the propagation effects along the profile. Both timing and waveforms of records are matched by synthetics calculated from 2-dimensional velocity models. The best 2-dimensional section begins at Imperial Valley with a thin crust containing the basin structure and thickens towards Pasadena. The detailed nature of the transition zone at the base of the crust controls the early arriving shorter periods (strong motions), while the edge of the basin controls the scattered longer period surface waves. From the waveform characteristics alone, shallow events in the basin are easily distinguished from deep events, and the amount of strike-slip versus dip-slip motion is also easily determined. Those events rupturing the sediments, such as the 1979 Imperial Valley earthquake, can be recognized easily by a late-arriving scattered Love wave that has been delayed by the very slow path across the shallow valley structure.

Part II

Modeling Regional Love Waves: Imperial Valley to Pasadena

1 Introduction

The major objectives of this part of the thesis are to initiate a field of study that will allow for the investigation of regional events at wavelengths shorter than their characteristic dimension and to provide a basis for source retrieval from sparsely recorded historic events. Thus, we will begin with a brief review of the types of seismograms available at the Seismological Laboratory at Caltech for the last 50 years of recording and how they could be used to full advantage.

Currently, there are very few on-scale recordings of major earthquakes (magnitude > 5.8) at near-regional ranges of 10 to 500 km except for a small number of low-gain (gain = 100) Wood-Anderson (WA) type seismograms. Moderate earthquakes in southern California with magnitudes between 4 and 5.5 are usually recorded on one or more of the following instruments in Pasadena: 1. The normal WA instrument ($T_o = 0.8$ sec.) with a gain of 2800. WA seismograms provide the basis for the Richter scale and the local magnitude, M_L ; 2. The long-period ($T_o = 6$ sec.) torsion instrument that operates at a gain near 900; 3. The Press-Ewing ($T_o = 30$ sec.) instrument (LP 30-90) that operates at a gain of about 2250. The instrumental responses for these

three systems are given in Figure 1. Two examples of the tangential component of the low-gain WA are displayed in Figure 2 along with examples of aftershock tangential recordings on the long-period ($T_o = 6$ sec.) torsions.

In the lower comparison, we display an earthquake of magnitude 6.5 in Northern Baja (Feb. 15, 1956), as recorded on the 100X WA and one of its aftershocks (magnitude = 5.0) on the high gain long-period torsion. In this example, we chose an aftershock that looks similar to the main event. Note that the main event is probably 100 times stronger at the longer periods, but because of differences in instrumental response they appear similar. Apparently, a complete trade-off between shifts in corner-frequency of the source spectrum and instrument response has occurred. The upper two records are not so similar, but these two events are located at different distances from Pasadena. The bottom event is actually an aftershock from an earlier event, the 1954 Borrego Mountain earthquake, and the top event is the 1969 Coyote Mountain earthquake recorded on the 100X WA filtered through a 0.5 sec. up and down triangle. Figure 3 shows the location of all events used in this study. If we knew the mechanisms of these aftershocks, we probably could make some good estimates of the faulting parameters of the main events by using the empirical Green's function approach (Hartzell, 1978). This approach has proven very useful in strong-motion simulations of main events from their aftershocks by assuming that the aftershock and the main event have the same mechanism. The strength of this procedure lies in eliminating the path effects by assuming that they are included in the aftershock record automatically. The main problem in applying this method is that it is difficult

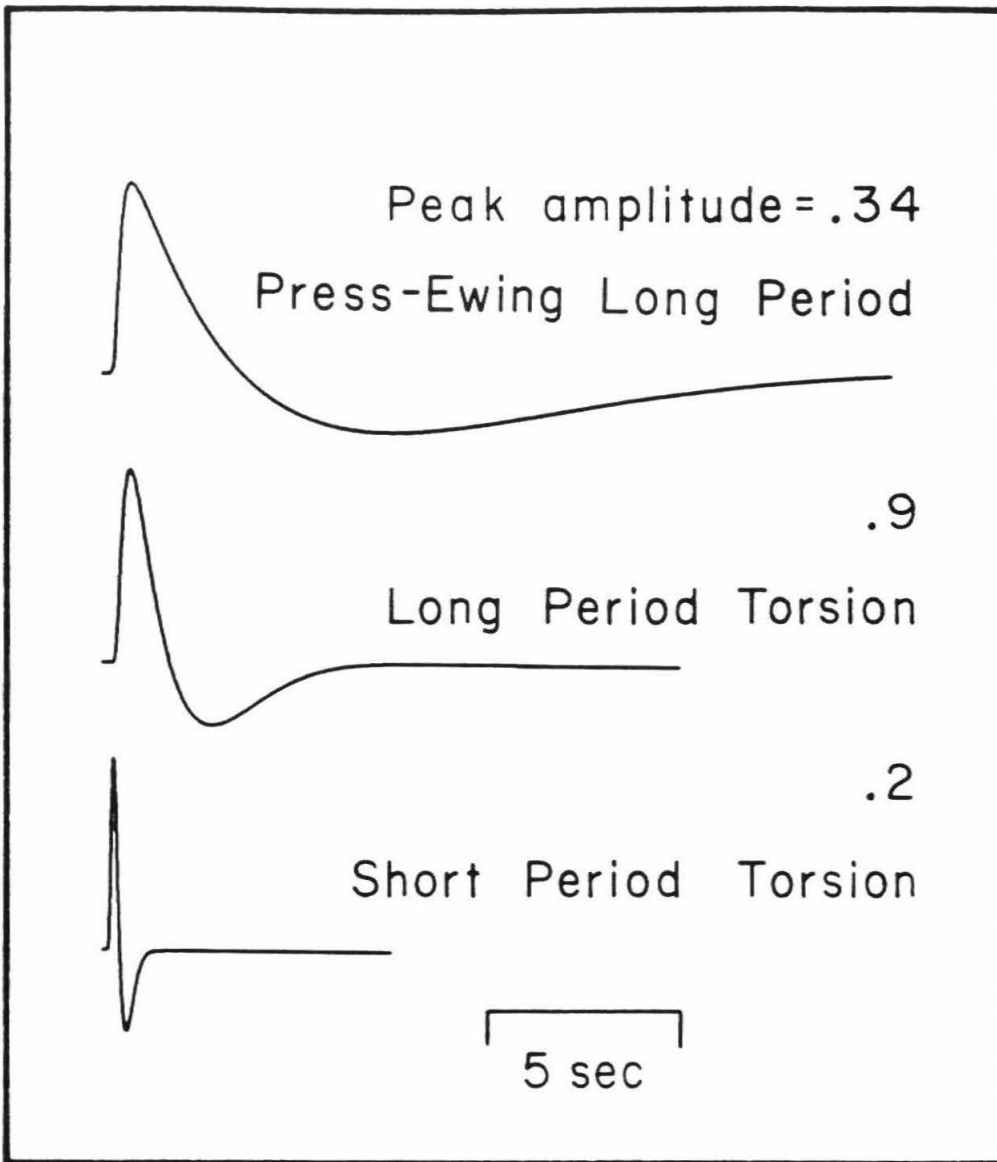


Figure 1: The instrument responses of the instruments recording the events used in this study.

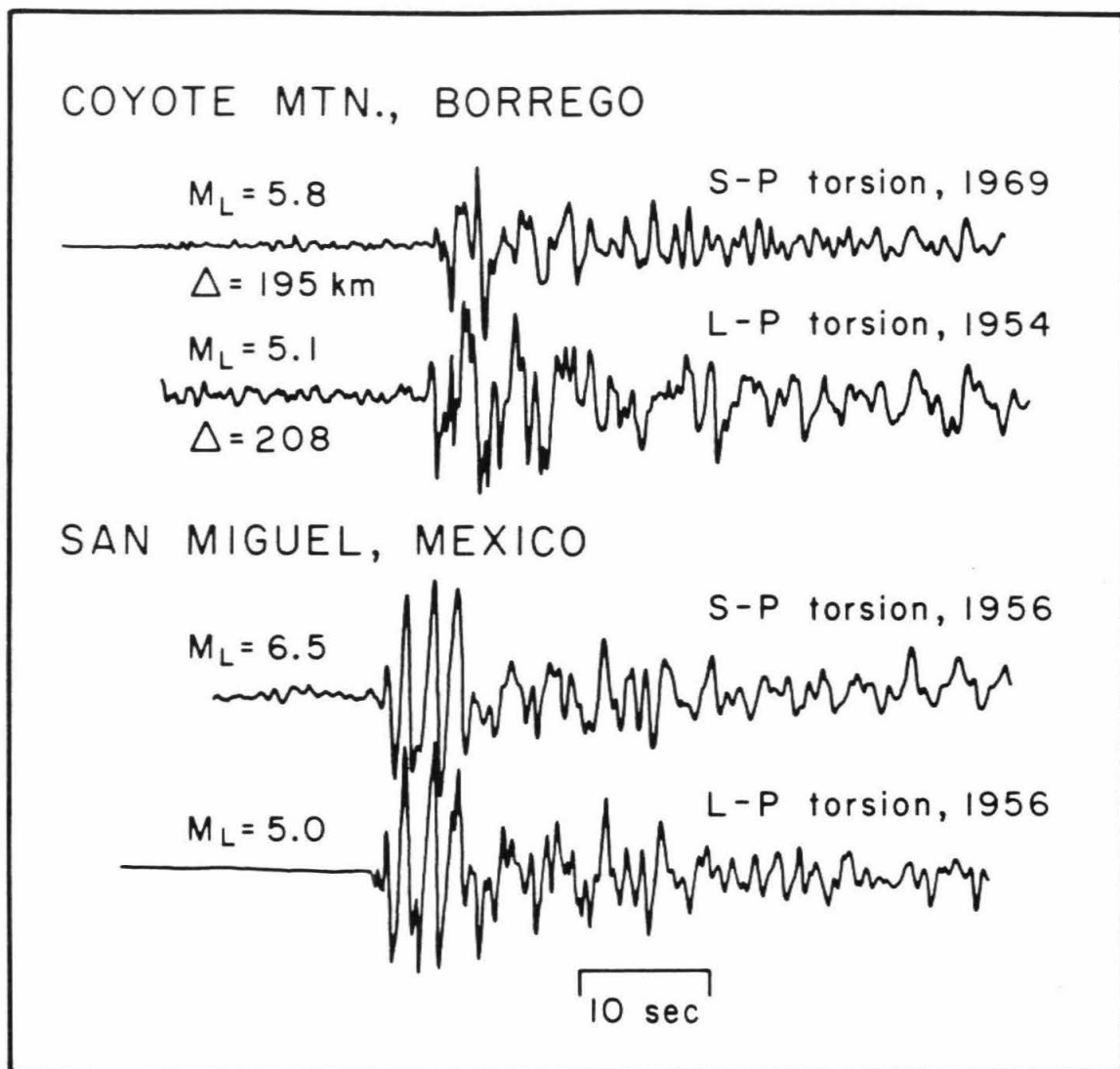


Figure 2: Comparison of aftershocks to main events on different Wood-Anderson (WA) torsion instruments. Top: 100X WA record of the Coyote Mountain event (filtered through a 0.5 sec up-and-down triangle) and an aftershock of the 1954 Borrego Mountain earthquake recorded on the long-period WA instrument. Bottom: 100X WA record of the San Miguel earthquake and one of its aftershocks recorded on a high-gain (gain is about 900) long-period WA torsion instrument. (San Miguel records were provided by Joanne Yoshimura).

EVENT LOCATIONS

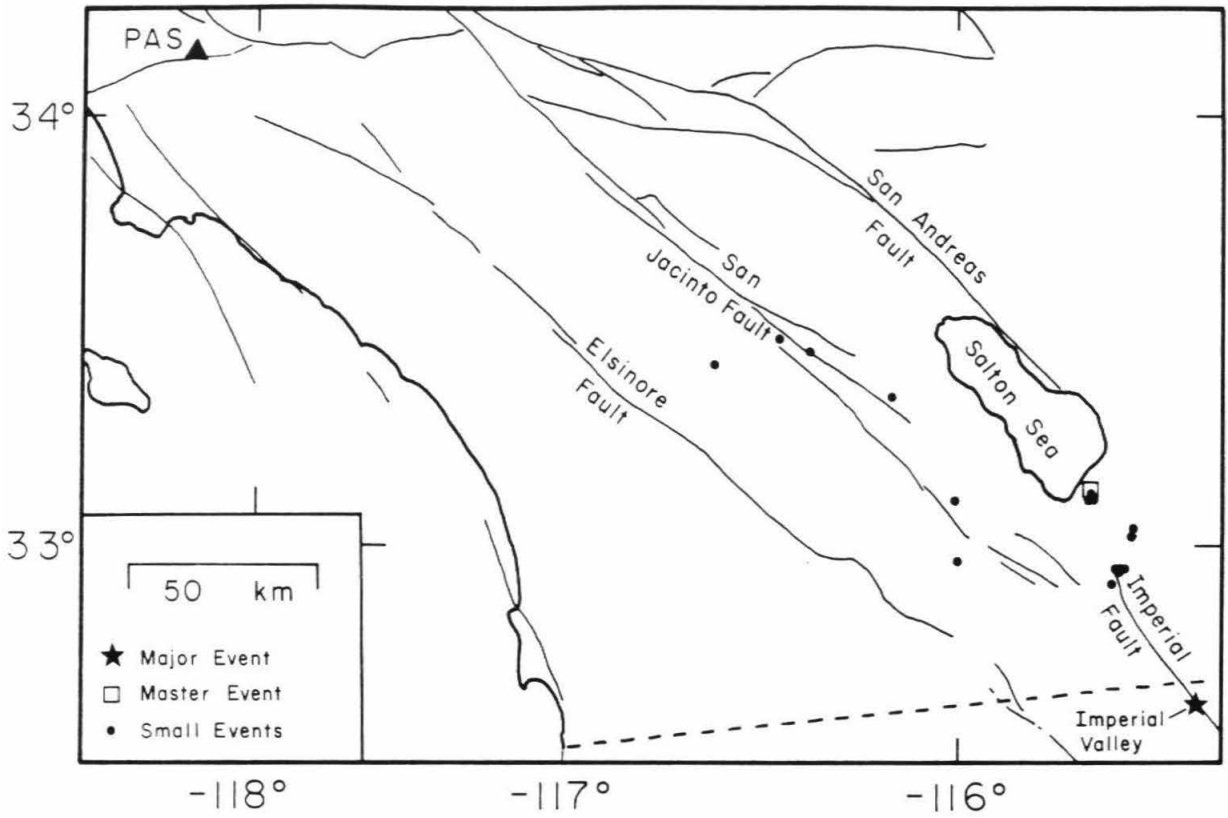


Figure 3: Map showing locations of Pasadena, PAS, and events used in this study.

to find an aftershock with the same orientation as the main event at the appropriate depth and range.

Generally, we do not know the mechanisms of many of these moderate aftershocks because they are too large for local arrays and too small for global networks. In addition, waveforms of different aftershocks are often so different, even if they are spatially close to each other, that it is not easy to determine which aftershock can be used as an empirical Green's function to simulate the main event. Examples of this category of events are the series of aftershocks of the 1979 Imperial Valley earthquakes recorded on *LP* 30-90 at Pasadena (Figure 4). Notice that for the three aftershocks labelled A, B and C, motions for all three events are about the same size on the vertical (UP) component but distinctly different on the horizontals (EW and NS). Differences in waveforms are also apparent on all three components. Since the paths from the Imperial Valley to Pasadena are essentially the same for the three events, we would conclude that the source characteristics (depths and faulting parameters such as strike, dip and rake) must be different. As we will discuss shortly, event A is probably a mid-depth, normal, dip-slip event, whereas event B is a shallow, normal, dip-slip event. Event C is a deep strike-slip event.

In order to study these seismograms in detail, we digitized and rotated the NS and EW components to obtain the tangential (SH waves) and vertical-radial (P-SV waves) components as displayed in Figure 5. At these periods the motion appears to be well-behaved in that the P-waves are not apparent on the tangential component. Particle motion studies of the type discussed by

AFTERSHOCKS OF IMPERIAL VALLEY 1979 EQ

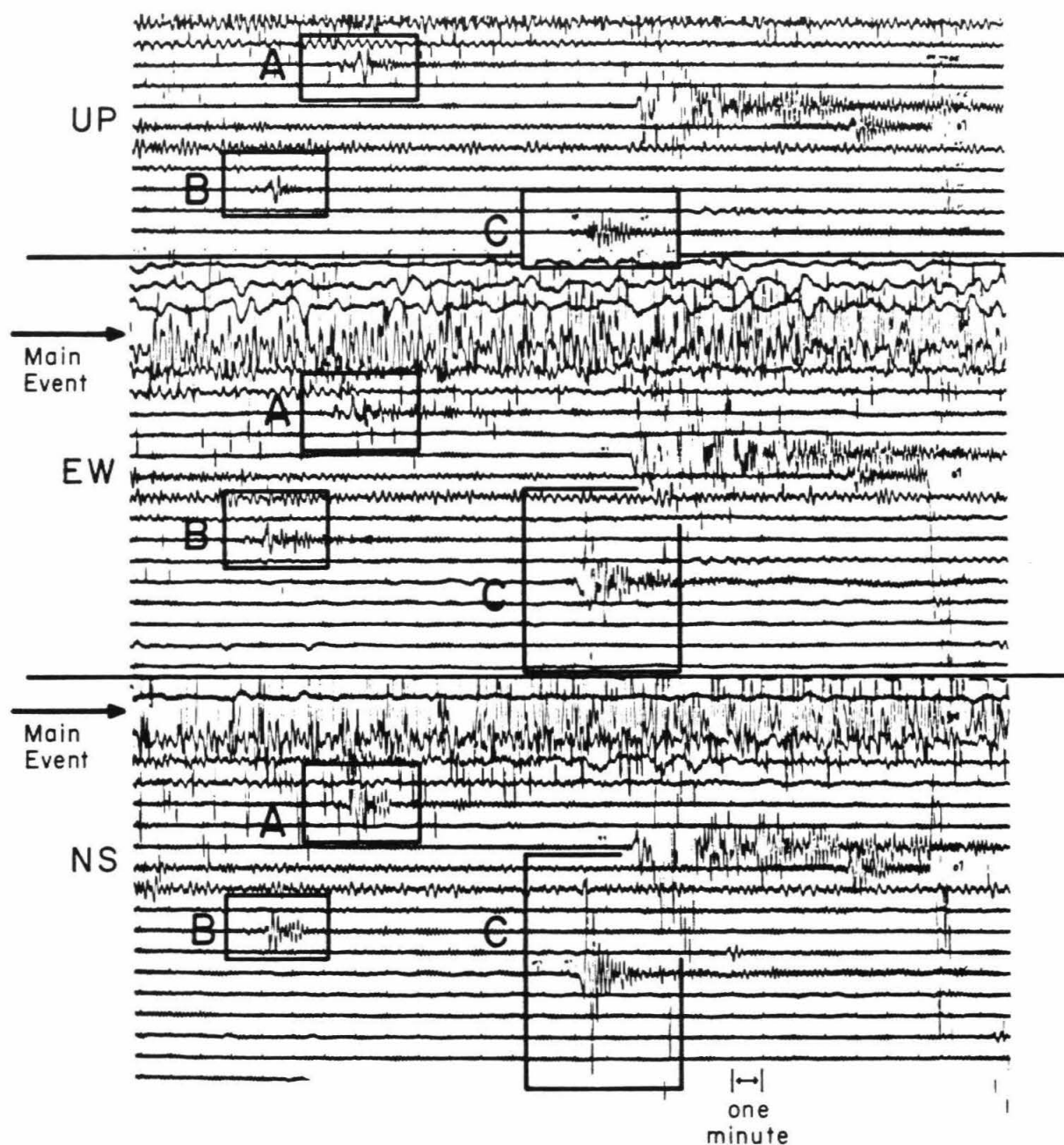


Figure 4: Three-component seismograms of the aftershock sequence recorded on the long-period Press-Ewing 30-90 instrument at Pasadena. Note the difference in waveforms and relative amplitudes of the three boxed aftershocks A, B, and C between components. The event locations are given in Table 1.

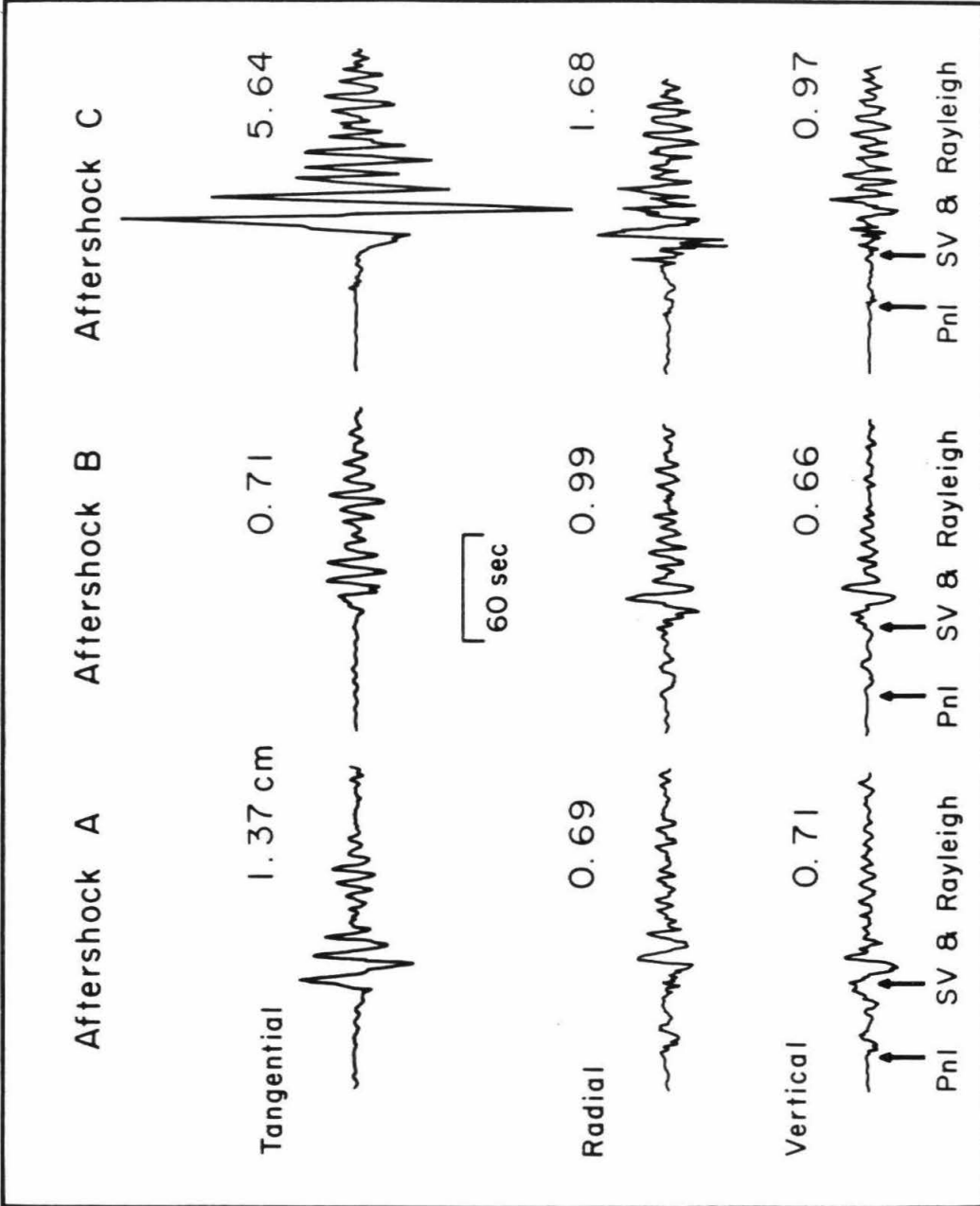


Figure 5: Rotated seismograms of the three aftershocks shown in Figure 4. Maximum amplitudes are given in mm.

Vidale (1986) conducted on these recordings indicate that the first 10 sec of record is consistent with P-waves and diffracted SV-waves followed by Rayleigh motion. Similar analysis of filtered rotated torsion records indicates that separation of the P-SV and SH motions occurs down to periods of about 1 second. Thus, it appears that two-dimensional models may prove effective in removing the path effects so that source retrieval is possible. For example, Vidale and Helmberger (1988) successfully used 2-D structure to model path effects at short (< 100 km) ranges.

In this study, we will derive a 2-D model appropriate for a cross section from Imperial Valley to Pasadena, using master events, known sources, and a forward modeling approach. The resulting Green's functions are then used to examine some of the more important events located in the section (Figure 3). We considered only the tangential motions in this pilot study because less computational effort is involved compared to modeling the P-SV motions recorded on the radial and vertical components.

2 Crustal Cross Section and Green's Functions

Searching for suitable Green's functions by trial-and-error testing can be a time-consuming endeavor, but the basic approach has proven effective in previous studies (Vidale *et al.*, 1985; Helmberger and Vidale, 1988; Vidale and Helmberger, 1988). Two types of codes were employed, namely, generalized ray theory (GRT) for dipping layers (Helmberger *et al.*, 1985) and a finite-difference (FD) technique (Vidale *et al.*, 1985; Helmberger and Vidale, 1988). The first method is analytical and can be used effectively to adjust deep,

smoothly varying structures to obtain proper timing and critical angle positions. The truncation of basins, however, requires the more powerful numerical approach. Some of the details of forward modeling strategies for this situation will be discussed later, but first, we present in Figure 6 our best-fitting model and corresponding Green's functions. The source is situated at mid-depth (7 km) in the Imperial Valley basin, with responses given at 50 km intervals. Note the soft basin structure. This structure is responsible for the rapid development of surface waves, which occur within the first 50 km of propagation. The waveform appears to change relatively slowly in traversing the remaining path. Note the ringing waveform for the dip-slip case versus the simple large amplitude pulse for the strike-slip orientation at the nearest range. This effect can be explained easily by the corresponding vertical radiation patterns (Vidale *et al.*, 1985).

Figure 7 shows the corresponding synthetics for the strike-slip case convolved with the instrument responses displayed in Figure 1. Amplitudes are given in mm as normalized to a moment of $4\pi\rho \times 10^{25}$ dyne-cm, where ρ is the density at the source location.

Changing the source positions relative to the basin has a dramatic effect as displayed in Figure 8. The relatively hard-rock path to Pasadena produces little waveform distortion. Shooting back into the basin produces a wave train similar to the motions observed at El Centro for Borrego Mountain events (Vidale *et al.*, 1985). The quick change in waveforms observed at Pasadena for small changes in source position near the basin boundary is the primary reason for abandoning a flat-layered structure.

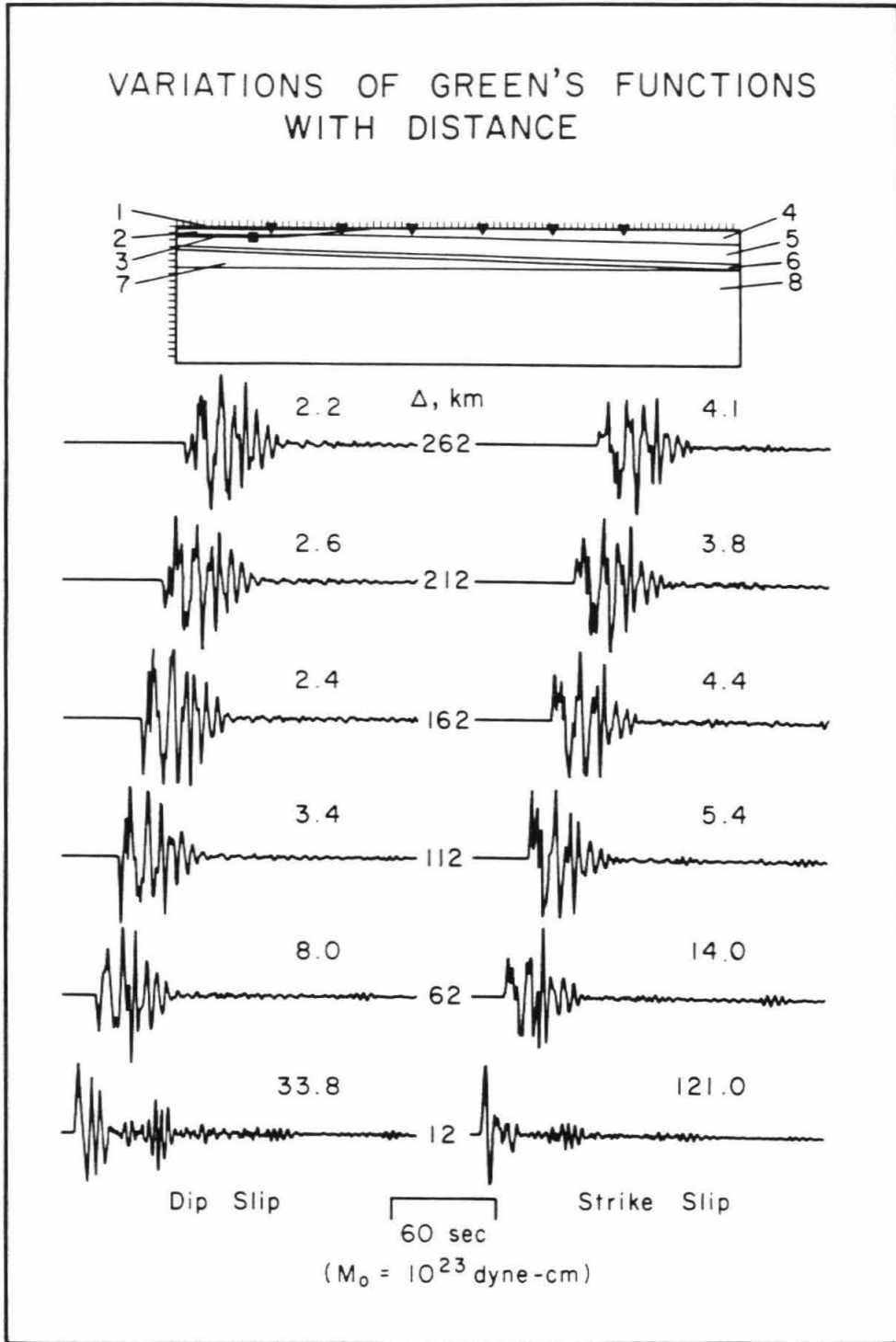


Figure 6: Preferred velocity model and the corresponding Green's functions generated with a source depth of 7 km at the location of the 1976 Brawley earthquake (Distance from Pasadena to the epicenter of the Brawley earthquake is 262 km). The stations are located at 50 km intervals, with the last station as the Pasadena station. Notice the rapid development of surface waves in the basin. Maximum amplitudes are given in 10^{-2} mm.

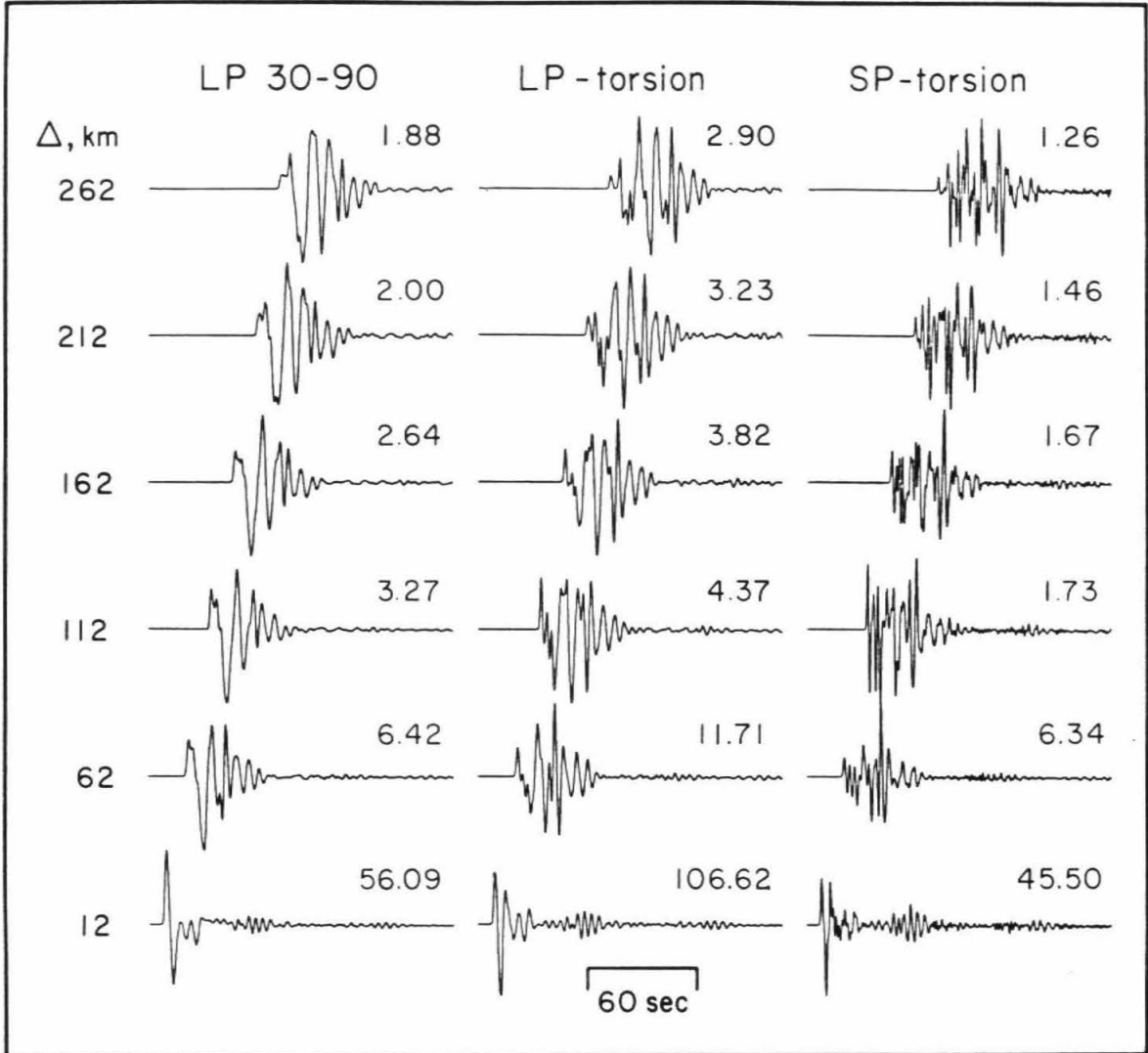


Figure 7: Comparison of the profile of Green's functions corresponding to a pure strike-slip source as recorded on the three instruments displayed earlier in Figure 1. Amplitudes are given in mm for a moment of $4\pi\rho \times 10^{25}$ dyne-cm.

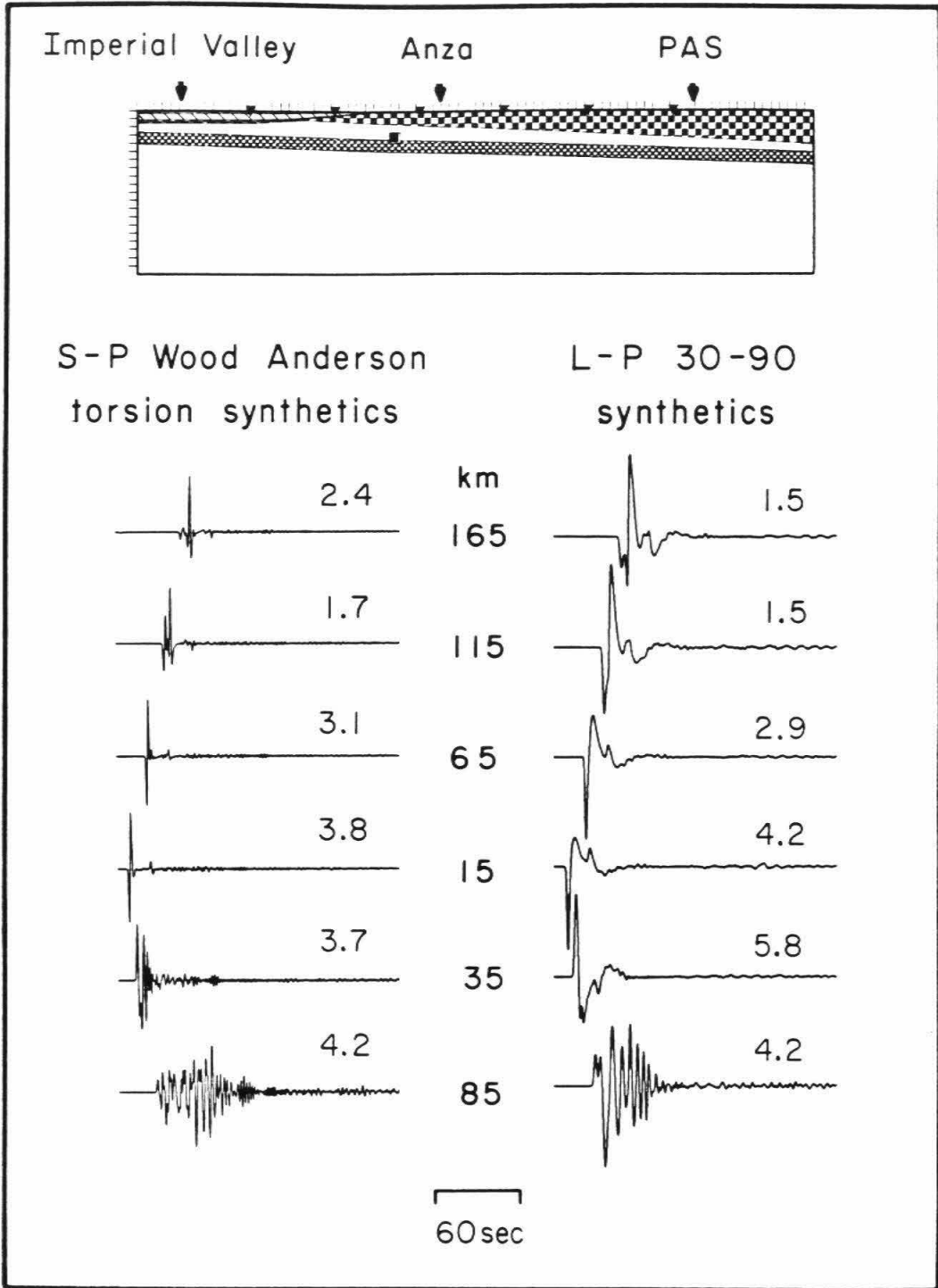


Figure 8: Profile of Green's functions with the source now outside the basin. Little waveform distortion is observed along the path towards Pasadena (upper four traces), while very complicated waveforms develop rapidly in the basin (lower two traces), indicating the important effect of the basin on wave propagation along this profile.

3 Long-Period Modeling

As in all forward modeling attempts, one starts with the best geophysical data available for constraining the initial model. Fortunately, a considerable number of studies have been conducted in this region. For the Imperial Valley velocity profile, we used the model proposed by Fuis *et al.* (1982) and McMechan and Mooney (1980). Just outside the basin we used the results from Hamilton (1970), who investigated the Borrego Mountain aftershocks with controlled calibration shots. Hamilton's results suggest a thick, crust-mantle transition zone which is extended along the entire profile. At Pasadena we adopted the model proposed by Hadley and Kanamori (1977, 1979) with a thick crust and relatively sharp Moho transition. These vertical profiles were assembled by allowing for a gently dipping connecting structure, thus producing an initial cross section from Imperial Valley to Pasadena.

Synthetics for this starting model were generated and compared with observed records for the various calibration events displayed in Figure 3. For example, in Figure 9 we give the comparison between the prediction for the Brawley event and its aftershock. The source parameters for this event were determined earlier by Heaton and Helmberger (1978), and are treated as known. This assumption allows us to perturb the various model parameters to improve agreement in waveform and absolute timing. This procedure goes relatively fast for long-period modeling but becomes increasingly tedious at higher frequencies.

The best-fitting model (Figure 6) to date has a slow mantle velocity of 4.28 km/sec (layer 8), a northwest-dipping Moho-crustal transition layer of

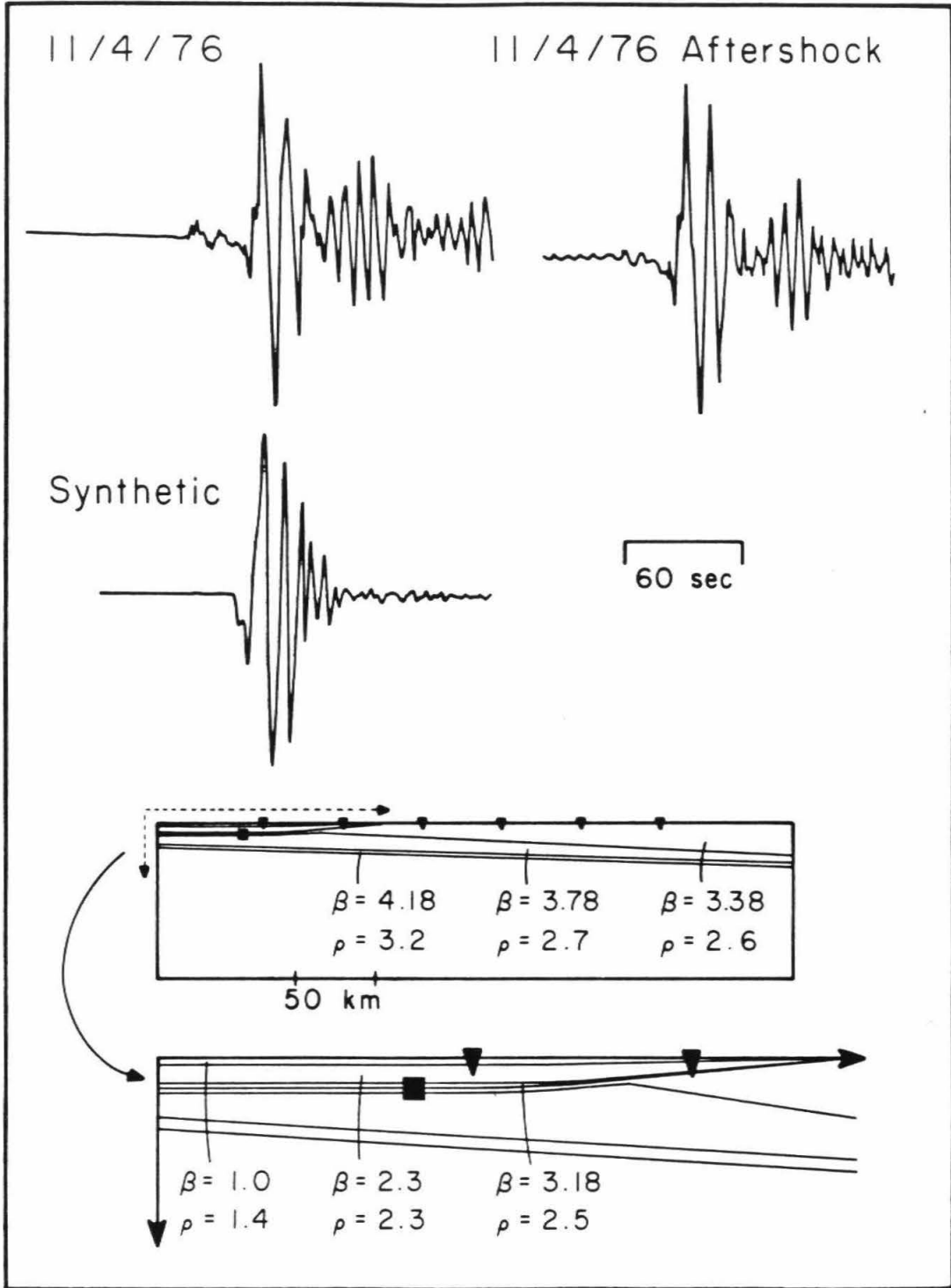


Figure 9: Tangential component of the Brawley earthquake and its aftershock as recorded on LP 30-90 of the Pasadena station and the corresponding synthetic prediction. The mechanism used to generate the synthetic is obtained from Heaton and Helmberger (1978).

4.18 km/sec (layer 7), a dipping crustal-Moho transition layer of 4.05 km/sec (layer 6), a dipping lower crust of 3.78 km/sec (layer 5) that thins out to the northwest, and an upper crust of 3.38 km/sec (layer 4) that also dips northwest. The idealized Imperial Valley basin surface has two layers of very slow shear velocities of 1.0 km/sec (layer 1) and 2.34 km/sec (layer 2), corresponding to what Fuis *et al.* (1982) described in their P-wave refraction studies. A thin layer of 3.18 km/sec (layer 3) that thins out at the edge of the basin lies underneath the slow sediments. This model is able to predict the arrival time and the waveform of the first 40 seconds. The secondary arrival occurring about 40 sec. after the initial motion is present on many records and will be discussed later.

The moment required to match the amplitudes is 3.0×10^{23} dyne-cm on the long-period modeling, compared to 3.2×10^{23} dyne-cm found by Heaton and Helmberger (1978), using local, strong-motion, intermediate-period records. This seems like a reasonable difference, since the lack of correction for intrinsic Q and scattered energy, imprecise knowledge of instrumental gain, small changes in strike, or three-dimensional structures etc. could account for such a difference.

Finally, with the model adjusted to predict synthetics matching the master event, we can easily perform depth sensitivity studies as displayed in Figure 10. The synthetics are generated with the source at a distance of 262 km from Pasadena, so the source is inside the basin at depths of 3.5 and 7 km and below the basin at depths of 10.5 and 14 km. For both strike-slip and dip-slip mechanisms, absolute amplitude decreases with depth for a given moment. In

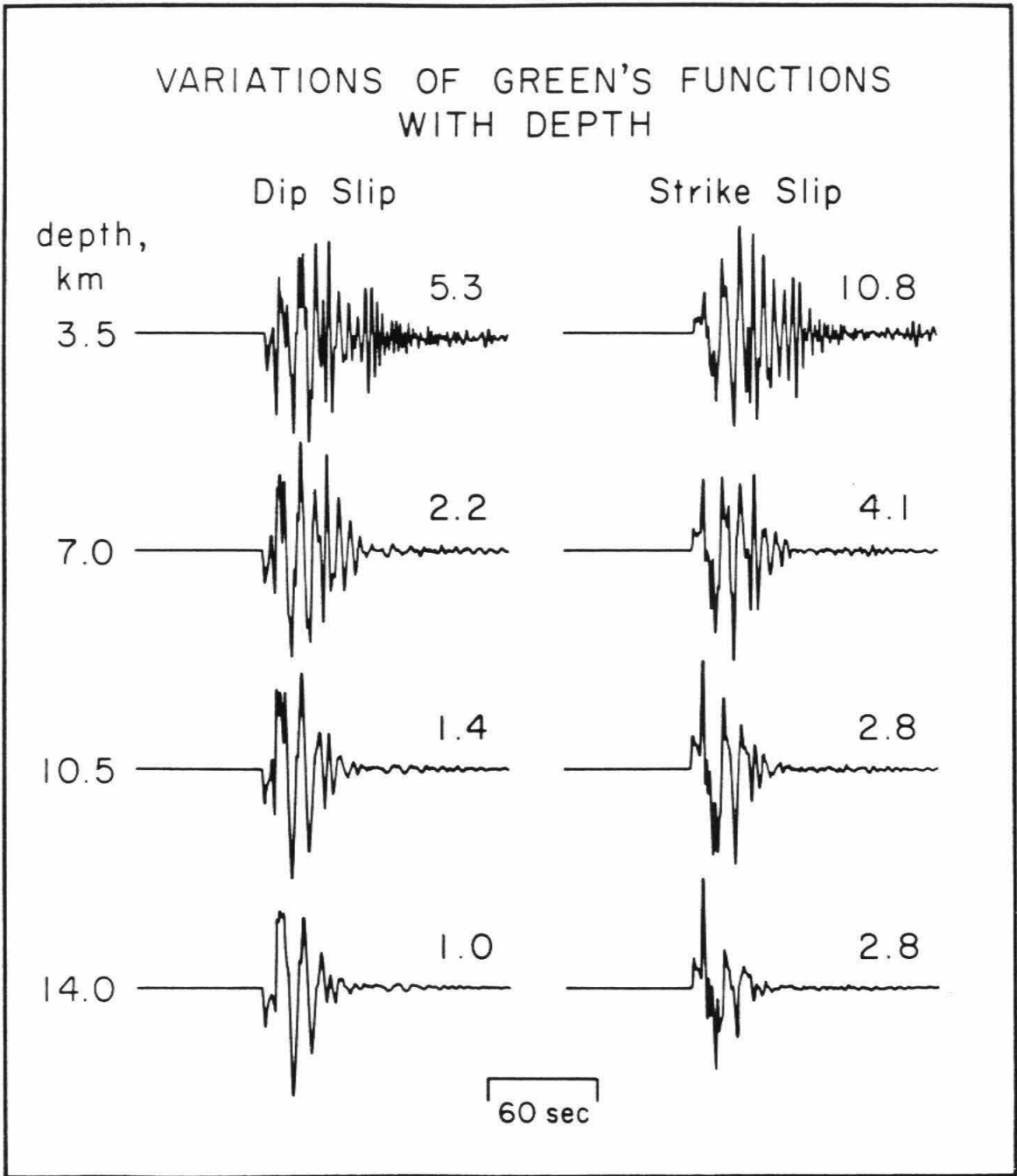


Figure 10: Sensitivity of Green's functions to depth. Sources are put in four different depths at the same epicentral location as the 1976 Brawley event: 3.5, 7.0, 10.5 and 14.0 km. In general, when the source is still in the basin, more surface waves are generated and when the source is below the slow sediments in the basin, the waveforms are simpler and energy drops off rapidly with time.

addition, a pure strike-slip mechanism results in almost twice the amplitude of a pure dip-slip mechanism at all four depths. In general, we also expect to see a shallow source excite more surface waves for both mechanisms, and a deeper source show less complexity. These results are similar to those found in flat, layered models. After reviewing mechanisms all the published mechanisms for events in this region (Fuis *et al.*, 1982; Heaton and Helmberger, 1978; Johnson and Hadley, 1976; Johnson and Hutton, 1982; Liu and Helmberger, 1985), a total of 21 possible orientations for each event was considered. The best-fitting combinations are displayed in Figure 11 with depths, magnitudes and moment estimates given in Tables 1 and 2. Note that event C, as discussed earlier, is modeled as a deep strike-slip event, while event B appears to be a shallow dip-slip event.

For small events we expect source durations to be short compared to the 30-90 instrumental response (see Figure 1), and therefore, we should be able to fit any observed long-period seismograms by a linear combination of the Green's functions displayed in Figure 10. A total of nine events with unknown source parameters, including the three aftershocks described earlier and the Brawley aftershock, were collected as a data set to which the Green's functions were applied. These events are listed in Table 1, where the locations and depths are given according to the Caltech catalog. Moments calculated by matching the synthetics to the data for these events are listed in Table 2.

The sensitivity of Green's functions to depth for sources at Anza appears different than that in Imperial Valley. In general, the waveform is very simple for both a strike-slip and a dip-slip mechanisms, and it changes only slightly

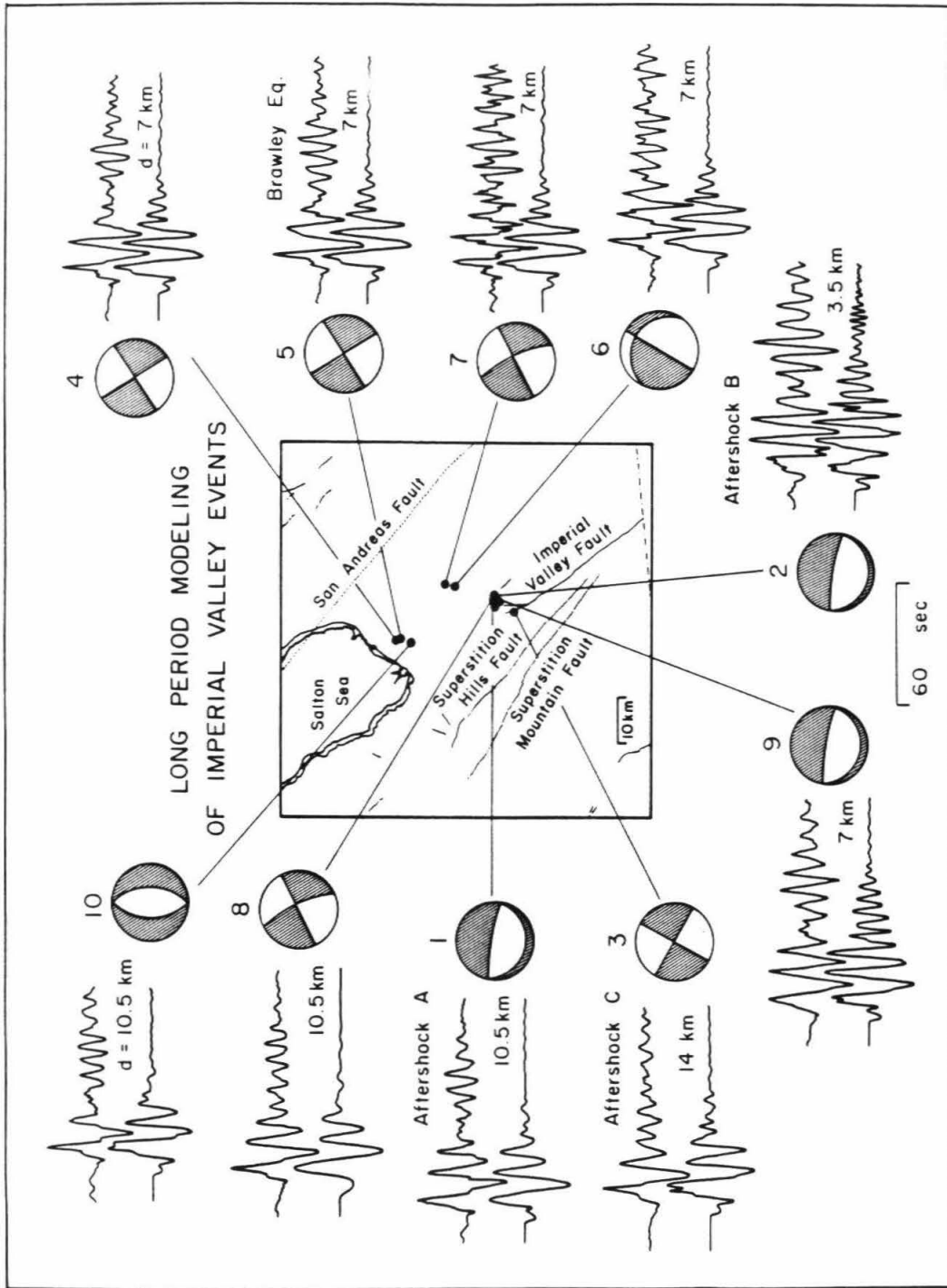


Figure 11: Long-period modeling of nine aftershocks and small events of unknown source characteristics in the Imperial Valley. Data shown are recorded on the LP 30-90 instrument. The modeled mechanisms are also shown. Results indicate that event 'C' is a deep strike-slip event, event 'B' a shallow dip-slip event and event 'A' a mid-depth dip-slip event.

Table 1. Summary of earthquakes used in the Imperial Valley long period study.
 Dips and rakes follow the convention by Vidale *et al.* (1985).
 Strikes are measured clockwise from North.

| Event # | Date | Time(GMT) | Latitude(N) | Longitude(E) | Depth(km) | Dip | Rake | Strike |
|---------|----------|-------------|-------------|--------------|-----------|-----|------|--------|
| 1(A) | 79-10-16 | 03:39:35.04 | 32° 56.92' | -115° 33.01' | 5.14 | 10° | 90° | 99° |
| 2(B) | 79-10-16 | 09:36:41.89 | 32° 56.98' | -115° 31.41' | 4.27 | 10° | 90° | 99° |
| 3(C) | 79-10-16 | 11:47:56.06 | 32° 54.81' | -115° 33.61' | 5.09 | 90° | 180° | 119° |
| 4 | 76-11-4 | 14:12:50.28 | 33° 07.41' | -115° 37.19' | 2.71 | 90° | 180° | 328° |
| 5* | 76-11-4 | 10:41:37.54 | 33° 07.89' | -115° 37.40' | 0.55 | 90° | 180° | 328° |
| 6 | 79-10-16 | 23:16:32.18 | 33° 01.33' | -115° 30.37' | 3.32 | 20° | 180° | 300° |
| 7 | 79-10-17 | 22:45:33.82 | 33° 02.40' | -115° 30.02' | 1.87 | 70° | 180° | 334° |
| 8 | 79-10-16 | 03:10:47.83 | 32° 57.05' | -115° 32.10' | 4.22 | 70° | 180° | 334° |
| 9 | 79-10-16 | 05:49:10.97 | 32° 56.48' | -115° 32.31' | 4.66 | 10° | 90° | 99° |
| 10 | 81-4-25 | 07:03:14.12 | 33° 06.24' | -115° 37.69' | 5.24 | 45° | -90° | 0° |

* Brawley Earthquake

Table 2. Imperial Valley moments obtained by fitting long-period *SH* and the corresponding M_L and depths compared to the catalogue value.

M_o are given in 10^{22} dyne-cm. Depths are given in km.

| Event | M_o | M_L | | Depth(km) | |
|-------|-------|-----------|---------|-----------|---------|
| | | <i>SH</i> | catalog | Modeled | catalog |
| 1 | 15.3 | 4.5 | 4.6 | 10.5 | 5.14 |
| 2 | 2.4 | 3.3 | 4.1 | 3.5 | 4.27 |
| 3 | 39.2 | 4.6 | 4.8 | 14.0 | 5.09 |
| 4 | 6.3 | 4.5 | 4.4 | 7.0 | 2.71 |
| 5 | 30.0 | 4.8 | 5.1 | 7.0 | 0.55 |
| 6 | 60.0 | 5.2 | 5.0 | 7.0 | 3.32 |
| 7 | 4.1 | 4.4 | 4.7 | 7.0 | 1.87 |
| 8 | 62.1 | 4.7 | 4.6 | 10.5 | 4.22 |
| 9 | 9.38 | 4.8 | 5.1 | 7.0 | 4.66 |
| 10 | 6.1 | 4.5 | 3.9 | 10.5 | 5.24 |

with depth (Figure 12). It appears that the deeper the event, the simpler the waveform created. This feature proves useful in fixing the depths of events as did the amount of surface wave excitation for events in the Imperial Valley.

In order to check the derived crustal model for its accuracy outside the Imperial Valley sedimentary basin, we applied the same process to three events at Anza, an aftershock of the Coyote Mountain 1969 event and two aftershocks of the 1968 Borrego Mountain event (see Figure 13). The mechanisms used to model the Anza events were again collected from various studies (Sanders and Kanamori, 1984; Given, 1983) and adjustments made to fit the data. The fits between synthetics and data are reasonably good, with results given in Table 3.

Most of the aftershocks in the Borrego region produced mechanisms similar to their main events, with results given in Table 4. The mechanisms for the main events are given by Thatcher and Hamilton, 1973; Ebel and Helmburger, 1982; Burdick and Mellman, 1976 and Sanders *et al.*, 1986. The waveforms are relatively simple, as shown in Figure 13, when compared to the Imperial Valley events in Figure 11, suggesting that the complexities of the waveforms are due to the existence of the basin.

4 Strong Motions from Imperial Valley Events

One of the primary objectives of this study was to provide Green's functions appropriate for strong motions in the frequency domain of 10 to 0.1 Hz. Unfortunately, we do not have broad-band data at this magnitude range, so we must rely on recordings from the 100X WA.

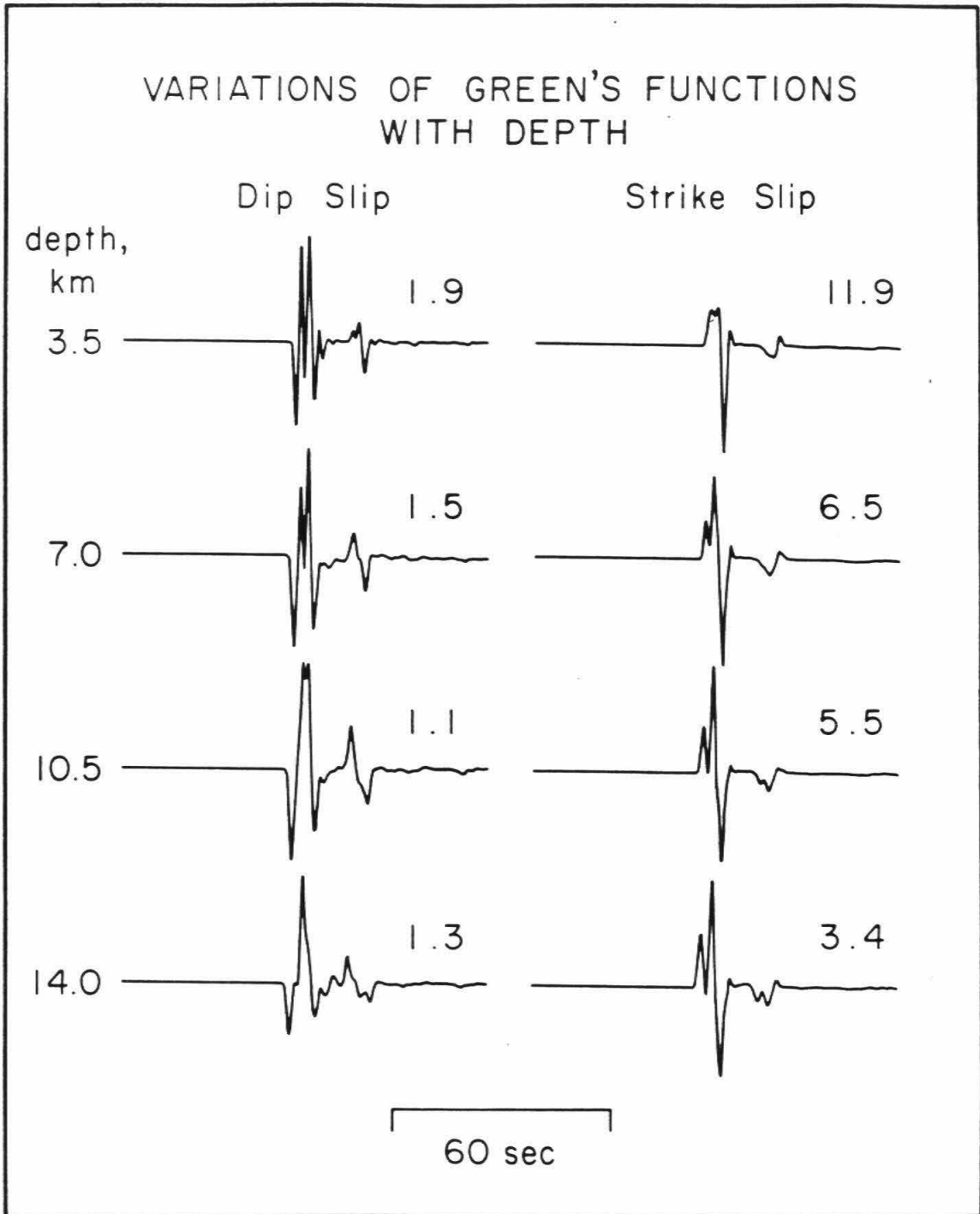


Figure 12: Sensitivity of Green's functions to depth with the source at Anza distance. The waveforms are simple compared to those displayed in Figure 10. There is not as much variation with depth as in the previous case.

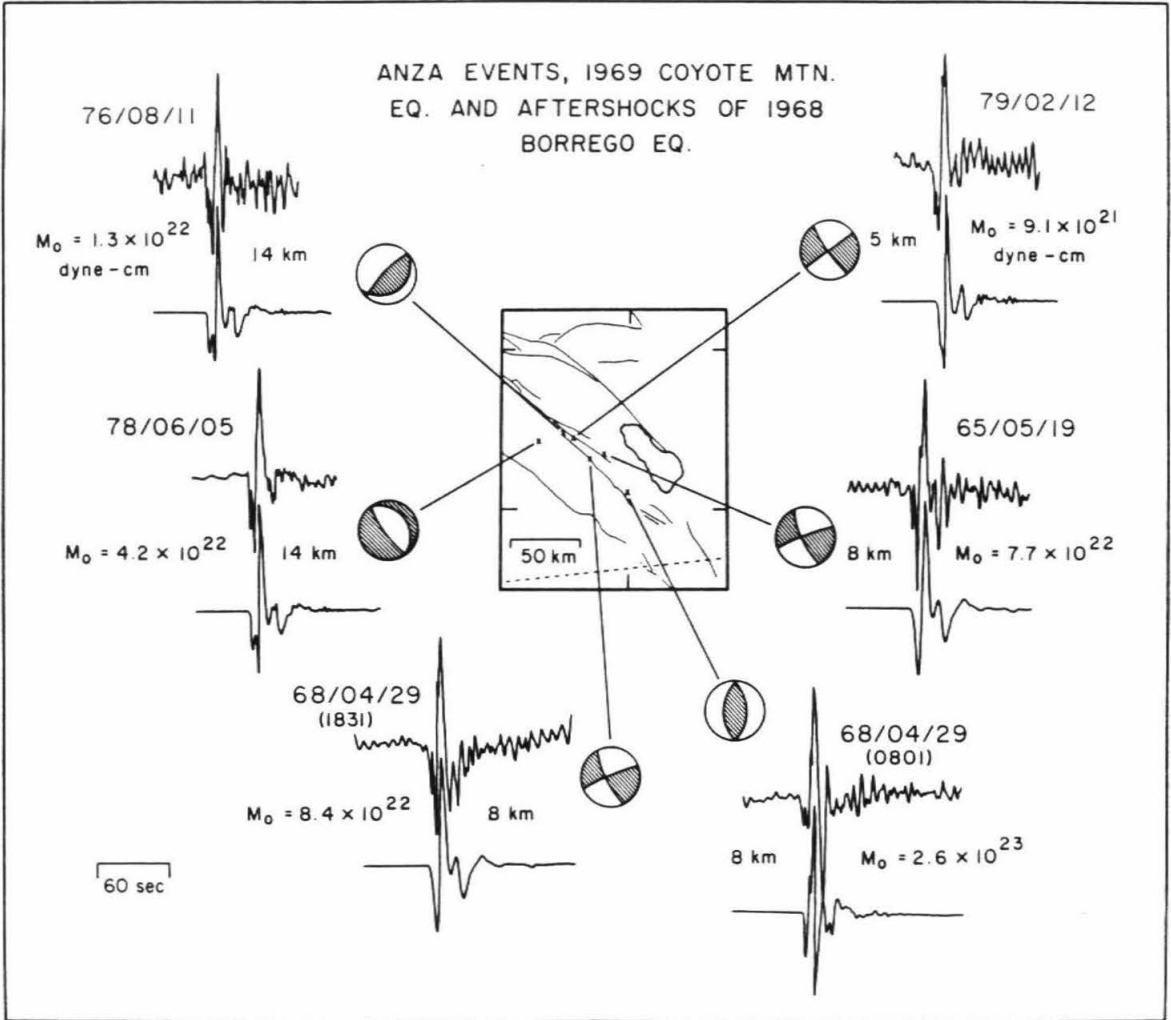


Figure 13: Long-period modeling of three Anza events, two aftershocks of the 1968 Borrego Mountain event and one of the 1969 Coyote Mountain aftershocks. The corresponding focal mechanisms are also shown.

Table 3. Summary of source mechanisms fit to three Anza events in the local magnitude range of 4 to 5.

| Event | | | | Depth | Dip | Rake | Strike |
|--------|-------------|-------------|--------------|-------|-----|------|--------|
| Date | Time | Latitude(N) | Longitude(E) | | | | |
| 760811 | 15:24:55.42 | 33° 28.9' | -116° 30.62' | 14.0 | 70° | -86° | 45° |
| 780605 | 16:03:03.72 | 33° 25.21' | -116° 41.61' | 14.0 | 70° | -90° | 152° |
| 790212 | 04:48:42.26 | 33° 27.21' | -116° 25.44' | 5.0 | 81° | 0° | 145° |

*Depth is given in km. Date is given in year-month-day.

Time is given in GMT. Strike is measured clockwise from North.

Table 4. Summary of source mechanisms fit to aftershocks of the 1968 Borrego Mountain and 1969 Coyote Mountain earthquakes.

| Event | | | | | Dip | Rake | Strike |
|-------------|-------|------|-------------|--------------|-----|------|--------|
| Date | Hrmin | Sec | Latitude(N) | Longitude(E) | | | |
| Apr 9,1968 | 0800 | 38.5 | 33° 06.4' | -116° 00.4' | 45° | 90° | 0° |
| Apr 9,1968 | 1831 | 38.5 | 33° 18.9' | -116° 18.3' | 80° | 251° | 163° |
| May 19,1969 | 1440 | 33.0 | 33° 20.9' | -116° 11.3' | 80° | 251° | 163° |

*Strike is measured clockwise from North.

At 10 Hz the problem becomes extremely complex, and the motions no longer separate into the P-SV and SH components. Also, we no longer expect events of this magnitude ($M_L > 5.5$) to be as simple as the Coyote Mountain events discussed earlier. Thus, it is difficult to assess the adequacy of our results, since we can only compare predicted motions at Pasadena based on independently determined sources from near-field data at Imperial Valley. Three component data may help resolve the source properties by providing more constraints, and this subject will be addressed in a later effort. At this stage, we examine only the 1979 Imperial Valley earthquake as an example. The secondary energy, arriving about 40 sec after the initial motion that accompanies many of the shallow events in the Valley, will be discussed later.

1979 Imperial Valley Earthquake

Several studies have inverted the strong motions of the 1979 Imperial Valley mainshock to find the slip distribution in space and time. There is a general consensus that the strike-slip rupture initiated at 10 km depth and propagated northwestward along the Imperial Fault at a rate of 75% of the shear velocity; then the rupture continued on at a shallower depth (Hartzell and Helmberger, 1982; Hartzell and Heaton, 1983; Olson and Apsel, 1982). Archuleta (1984) holds a slightly different conclusion on the rupture process: an initial pure strike-slip source at about 8 km depth rupturing northwestward, and subsequent rupture occurred at two main locations, both at about 10 km depth, with a minor dip-slip rupture at about 30 km from the epicenter along the strike of the fault. The Hartzell and Helmberger model (model HH1) and the Hartzell and Heaton model (model HH2) are very similar, while Olson

and Apsel's model (model OA) is a more continuous model, which can be simulated using nine segments of rupture. We attempt to model this 1979 mainshock by treating each rupture segment in each inversion model as an earthquake source. Using the same mechanism as determined in the above studies for each segment, we combine our synthetics with the mechanisms and then sum up the segments according to the corresponding delay time along the fault. Simulations of such strong motion recorded at Pasadena on the short-period torsion are shown in Figure 14 with the corresponding inversion models.

A comparison of the data filtered through a 4 sec up-and-down triangle with the similarly filtered synthetic predictions is displayed in Figure 15. The synthetic responses shown in Figure 14 require a time-derivative to compare with the corresponding WA record. The derivative tends to emphasize the high frequencies similar to those seen in the Olson-Apsel model. In general, all of these models display some merit, although it appears that the two models on the left of Figure 15 fit the waveform data somewhat better. The important point in this comparison is not which model fits better but that complex earthquakes (multiple-ruptures) can be distinguished from simple events. Thus, this type of regional data from historic events can be used to help delineate rupture patterns along important fault segments.

5 Discussion and Conclusion

Many of the events in the Imperial Valley data set have a secondary arrival (which we have neglected), that is about 40 sec late (Figure 11). There are several possibilities for the secondary arrivals: 1. Three-dimensional path

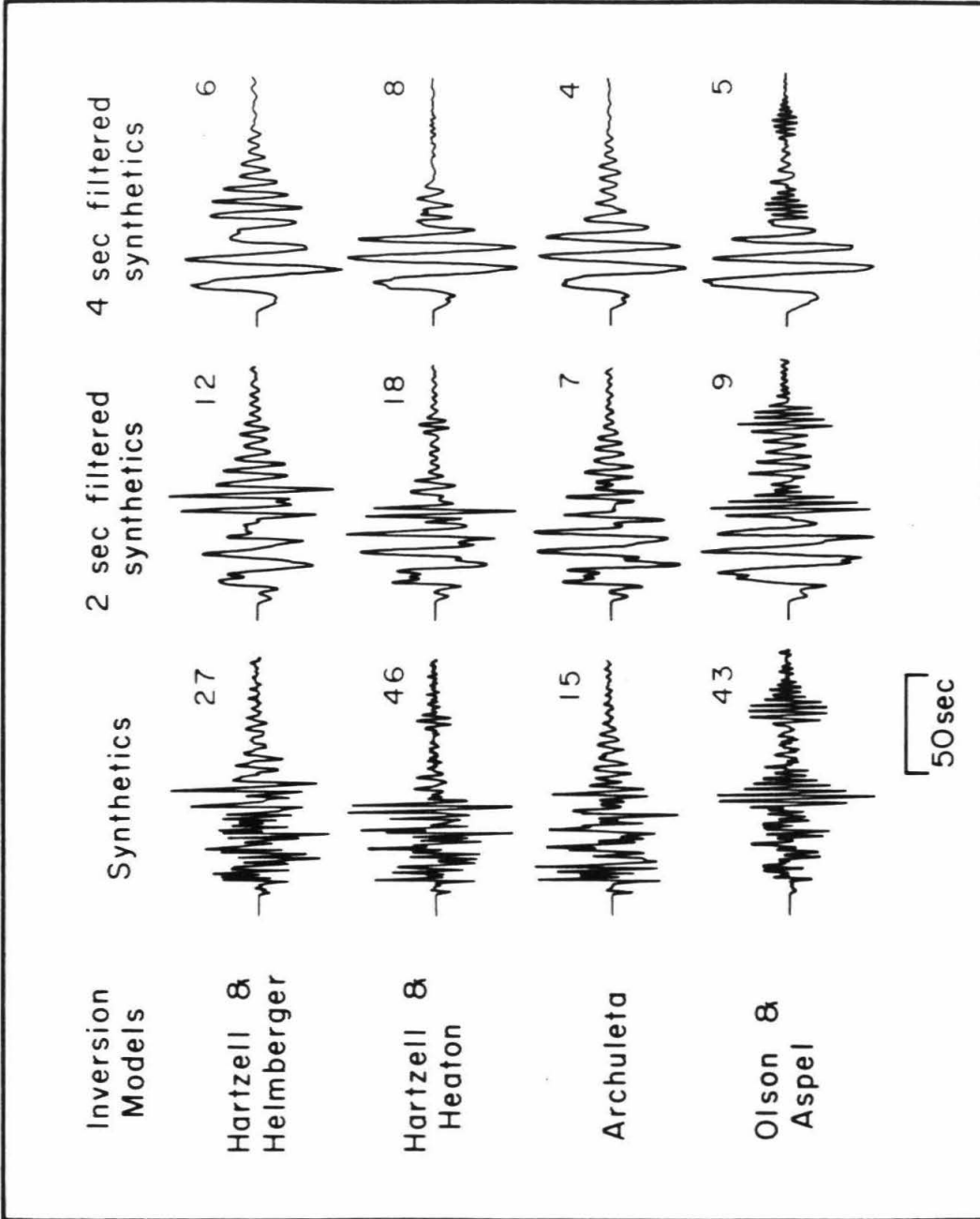


Figure 14: Simulations of strong motion of the 1979 Imperial Valley event using four inversion models (Hartzell and Helmberger, 1982; Hartzell and Heaton, 1983; Archuleta, 1984; and Olson and Aspel, 1982). Amplitudes are given in cm for a moment of 5.0×10^{25} dyne-cm.

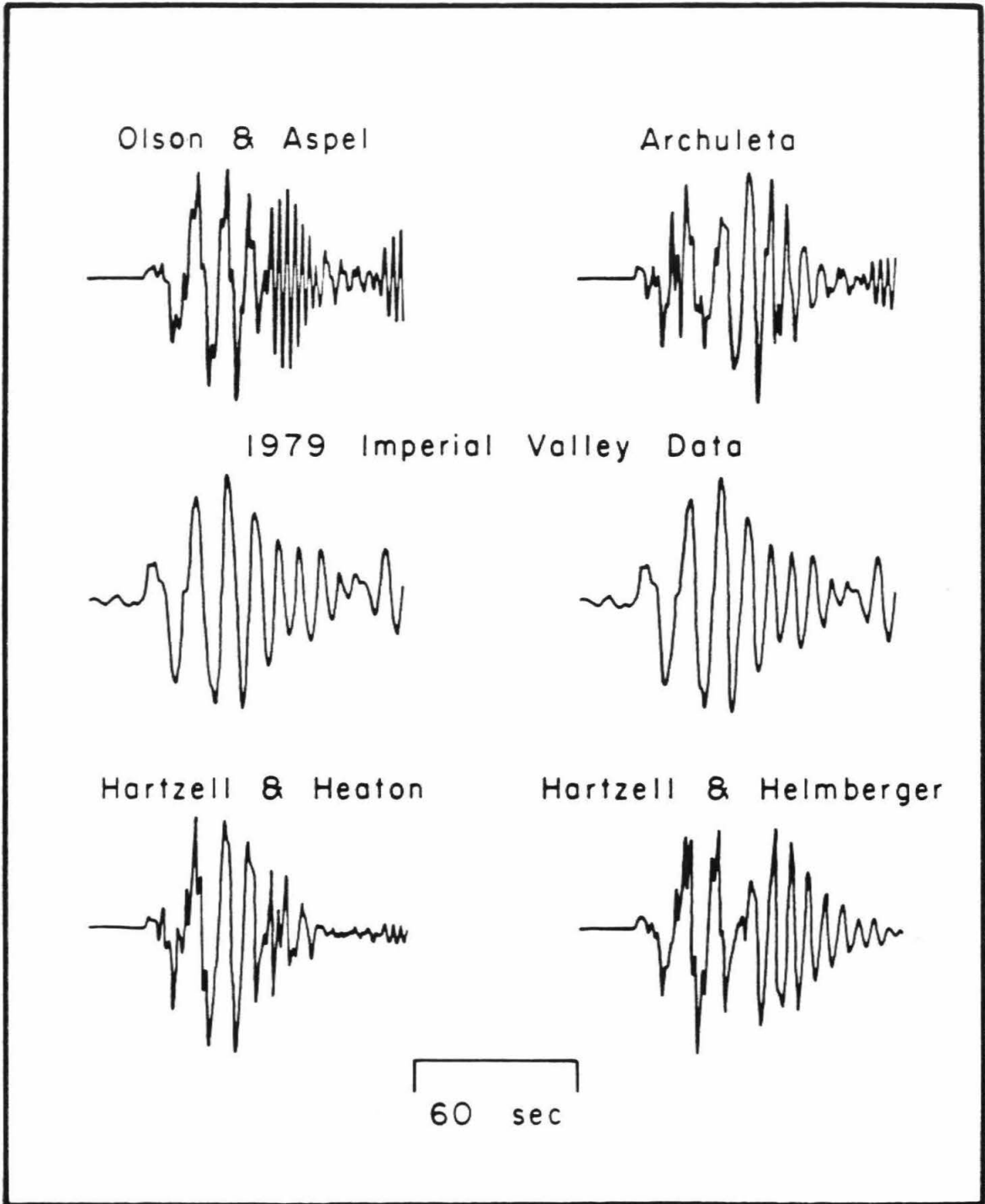


Figure 15: Comparison of a 4-sec filtered tangential motion against predicted synthetics for the 1979 Imperial Valley event.

effects, which include scattering due to the Imperial Valley basin structure; 2. Rupture effects, which include double events or complicated faulting mechanisms; 3. Receiver structural effects, which are local effects that are due to the receiver's being in or near a basin; 4. Path complications that include possible structural effects along the same path, which are not in the present model.

Three-dimensional path effects would result in waves arriving at the receiver along different azimuths. We determined by complex polarization studies (Vidale, 1986) on the three components, that the late arrival was traveling along approximately the same azimuth as the main arrival. So we believe that this late arrival comes mainly from the same azimuth as the main arrival, though there is a clockwise rotation after the first arrival at Pasadena. This effectively rules out possibility #1.

The three events we studied at Anza and the Borrego Mountain events show no secondary arrival at all. The arrivals have relatively simple waveforms. The hypothesis that the secondary arrivals on the Imperial Valley events are effects of the local receiver structure is then ruled out because of the absence of such arrivals on the records of events outside the basin.

We are now left with possibilities #2 and #4. It is fairly unreasonable to attribute double mechanisms to all events with secondary arrivals. However, shallow events have secondary arrivals, while deep events do not. The secondary arrivals are not seen in high-frequency records. These features suggest that this secondary arrival has traveled as a trapped wave in the surface sediments to the edge of the basin and then converts into a crustal Love wave for the rest of the path.

A number of numerical profiles with the source placed at various depths in a variety of basin models were generated to test the possibility of the above hypothesis. When the source is situated in the sediments and when the basin ends sharply, the secondary arrival becomes particularly strong, as displayed in Figure 16. Basin models with gently dipping edges do not show the secondary arrival and apparently scatter the surface waves at lower ray parameters, probably teleseismically as found in the study by Stead and Helmberger (1988).

The broad-band responses displayed in Figure 16 do not contain the instrument and suggest that the secondary arrival would not be depleted in high frequency as observed. Thus, the observed secondary arrival has lost its high frequencies by attenuation in the soft sediments, or perhaps the source excitation has very low stress drop. This subject is best pursued with broad-band three component array data and will be addressed in subsequent work.

In conclusion, we have demonstrated the effectiveness of using events with known source mechanisms to derive a regional crustal model and to make use of the model to retrieve source mechanisms for other events. This method is proven to be successful in matching SH waveforms and arrival times of events at different distances from the receiver. The method requires prior knowledge only about well-studied events and the availability of three-components seismograms with well-recorded events of unknown sources. These requirements can be met easily, since we have many stations with three-component seismograms that have recorded many regional events. As long as we have one master event to work with in the same area, source retrieval and strong

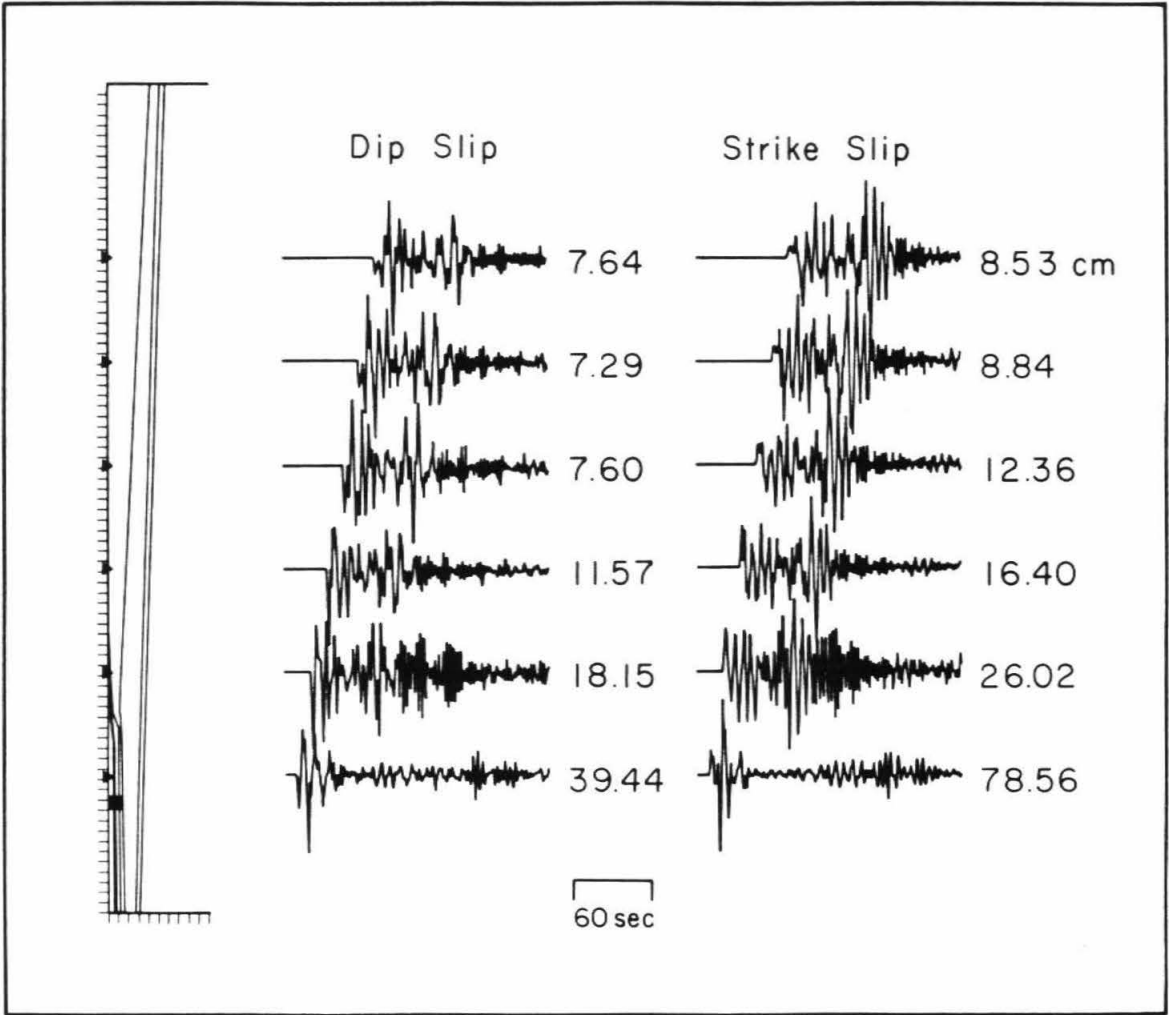


Figure 16: Numerical responses along a profile from IV to PAS for an idealized basin model. Note the sharp edge of the basin typical of faulted structures at the western edge of this particular basin. A strong secondary arrival is generated by such a sharp basin edge. Displacements are given for a moment of $4\pi\rho \times 10^{23}$ dyne-cm.

motion simulation or prediction can be done.

We have also demonstrated the sensitivity of various Green's functions to depth and mechanism. By applying the depth sensitivity of SH waveforms, we can now make an estimate of the depth of an event in the Imperial Valley recorded at regional distance by the rate of decay of reverberations in the record. This provides a powerful tool in detailed modeling of an event. With such a detailed model, we can now synthesize long-period, strong motions of an earthquake with any source mechanism, location and magnitude along the profile from Imperial Valley to Pasadena.

References to Part II

- Archuleta, R.J., 1984. A faulting model for the 1979 Imperial Valley earthquake, *J. Geophys. Res.*, **89**, 4559-4585.
- Burdick, L.J. and G.K. Mellman, 1976. Inversion of the body waves of the Borrego Mountain earthquake to the source mechanism, *Bull. Seismol. Soc. Am.*, **66**, 1485-1499.
- Ebel, J.E. and D.V. Helmberger, 1982. P-wave complexity and fault asperities: The Borrego Mountain, California, earthquake of 1968, *Bull. Seismol. Soc. Am.*, **72**, 413-437.
- Fuis, G.S., W.D. Mooney, J.H. Healy, G.A. McMechan and W.J. Lutter, 1982. Crustal structure of the Imperial Valley region in the Imperial Valley, California earthquake of Oct. 15, 1979, *U.S. Geol. Survey Prof. Paper*, **1254**, 25-49.
- Given, D.D., 1983. Seismicity and structure of the trifurcation in the San Jacinto fault zone, southern California, *Master's Thesis, California State University, Los Angeles*.
- Hadley, D. and H. Kanamori, 1977. Seismic structure of the Transverse Ranges, California, *Bull. Geol. Soc. Am.*, **88**, 1469-1478.
- Hadley, D. and H. Kanamori, 1979. Regional S-wave structure for southern California from the analysis of teleseismic Rayleigh waves, *Geophys. J. R. astr. Soc.*, **58**, 655-666.
- Hamilton, R.M., 1970. Time-term analysis of explosion data from the vicinity of the Borrego Mountain, California earthquake of 9 April, 1968, *Bull. Seismol. Soc. Am.*, **60**, 367-381.
- Hartzell, S.T., 1978. Earthquake aftershocks as Green's functions, *Geophys. Res. Lett.*, **5**, 1-4.
- Hartzell, S.T. and D.V. Helmberger, 1982. Strong-motion modeling of the Imperial Valley earthquake of 1979, *Bull. Seismol. Soc. Am.*, **72**, 571-596.
- Hartzell, S.T. and T.H. Heaton, 1983. Inversion of strong ground motion and teleseismic waveform data for the fault rupture history of the 1979 Imperial Valley, California, earthquake, *Bull. Seismol. Soc. Am.*, **73**, 1553-1583.
- Heaton, T.H. and D.V. Helmberger, 1978. Predictability of strong ground motion in the Imperial Valley: Modeling the M4.9, November 4, 1976 Brawley earthquake, *Bull. Seismol. Soc. Am.*, **68**, 31-48.
- Helmberger, D.V., G. Engen and S. Grand, 1985. Notes on wave propagation in laterally varying structure, *J. Geophys.*, **58**, 82-91.
- Helmberger, D.V. and J.E. Vidale, 1988. Modeling strong motions produced by earthquakes with two-dimensional numerical codes, *Bull. Seismol. Soc. Am.*, **78**, 109-121.
- Johnson, C.E. and D.M. Hadley, 1976. Tectonic implications of the Brawley earthquake swarm, Imperial Valley, California, January 1975, *Bull. Seismol. Soc. Am.*,

66, 1133-1144.

- Johnson, C.E. and L.K. Hutton, 1982. Aftershocks and pre-earthquake seismicity, California earthquake of Oct. 15, 1979, *U.S. Geol. Survey Prof. Paper*, **1254**, 59-76.
- Liu H.L. and D.V. Helmberger, 1985. The 23:19 aftershock of the 15 October 1979 Imperial Valley earthquake: More evidence for an asperity, *Bull. Seismol. Soc. Am.*, **75**, 689-708.
- McMechan, G.A. and W.D. Mooney, 1980. Asymptotic ray theory and synthetic seismograms for laterally varying structure: Theory and application to the Imperial Valley, California, *Bull. Seismol. Soc. Am.*, **70**, 2021-2036.
- Olson, A.H. and R.J. Apsel, 1982. Finite faults and inverse theory with applications to the 1979 Imperial Valley earthquake, *Bull. Seismol. Soc. Am.*, **72**, 1969-2001.
- Sanders, C.O. and H. Kanamori, 1984. A seismotectonic analysis of the Anza seismic gap, San Jacinto fault zone, southern California, *J. Geophys. Res.*, **89**, 5873-5890.
- Sanders, C.O., H. Magistrale and H. Kanamori, 1986. Rupture patterns and preshocks of large earthquakes in the southern San Jacinto fault zone, *Bull. Seismol. Soc. Am.*, **76**, 1187-1206.
- Stead, R.J. and D.V. Helmberger, 1988. Numerical-analytical interfacing in two dimensions with applications to modeling NTS seismograms, in *Special issue 'Scattering and Attenuation of Seismic Waves'*, *Pure and Appl. Geophys.* (in press).
- Thatcher, W. and R.M. Hamilton, 1973. Aftershocks and source characteristics of the 1969 Coyote Mountain earthquake, San Jacinto fault zone, California, *Bull. Seismol. Soc. Am.*, **63**, 647-661.
- Vidale, J., D.V. Helmberger, and R. W. Clayton, 1985. Finite-difference seismograms for SH waves, *Bull. Seismol. Soc. Am.*, **75**, 1765-1782.
- Vidale, J., 1986. Complex polarization analysis of particle motion, *Bull. Seismol. Soc. Am.*, **76**, 1393-1405.
- Vidale, J. and D.V. Helmberger, 1988. Elastic finite-difference modeling of the 1971 San Fernando, California earthquake, *Bull. Seismol. Soc. Am.*, **78**, 122-141.